

HIGH-Mn TWINNING-INDUCED PLASTICITY STEELS: MICROSTRUCTURE AND MECHANICAL PROPERTIES

P.S. Kusakin and R.O. Kaibyshev

Belgorod State University, Belgorod, Pobeda 85, 308015, Russia

Received: November 02, 2015

Abstract. A new class of austenitic steel for automotive applications exhibiting the TWIP (twinning-induced plasticity) effect, which provides an excellent combination of strength and ductility, is reviewed. Special attention is given to the microstructural design of TWIP steels, their alloying concept, thermomechanical processing, physical mechanisms responsible for superior ductility at room temperature ($\geq 100\%$) and high strength, which ensures a value of $\sigma_B \times \delta \geq 5 \times 10^4$ MPa $\times\%$, being highest among all steels. The correlation between microstructure and mechanical properties is discussed in detail. TWIP steel microstructural design is aimed to provide a stacking fault energy (SFE) between 20 and 40 mJ/m². In the steels with SFE values below 20 mJ/m², the ϵ (hcp) or α' (bcc) strain-induced martensite evolves during cold deformation. These steels exhibit the effect of transformation-induced plasticity (TRIP), which leads to $\sigma_B \times \delta = 3 \div 4 \times 10^4$ MPa $\times\%$. At SFE values $\geq 40 \div 50$ mJ/m², the mechanical twinning is suppressed, and the value of $\sigma_B \times \delta$ does not exceed 2×10^4 MPa $\times\%$. The role of twinning and dislocation slip in achieving ultra-high strength and ductility is considered. The specific mechanisms of solid-solution strengthening associated with the formation of a C-Mn dipole or octahedral clusters CMn_6 are discussed. The influence of thermomechanical treatment on the microstructure, crystallographic texture and mechanical properties of TWIP steel is also discussed. It was shown that extensive grain refinement provides a high increase in yield stress, and intense plastic straining can be applied to produce high-strength TWIP steels with ductility $\geq 20\%$.

1. INTRODUCTION

Progress in the automotive industry induces a demand for strong and ductile steels that must exhibit high strength with concurrently high plasticity to be feasible for the fabrication of inner car body parts by deep drawing [1]. Currently, steels with ferrite matrices and low contents of such interstitial elements as carbon and nitrogen (Interstitial free – IF-steels) are usually used for the outer panels of car bodies. These steels have elongation-to-failure up to 45% and ultimate tensile strength (UTS) up to 320 MPa (Fig. 1). Ferrite-martensite/bainite dual phase (DP), transformation-induced plasticity of retained austenite (TRIP-RA) and complex phase (CP-K) steels

have been attractive for the inner parts of automotive bodies to provide structural reinforcements and energy absorption during collisions. The UTS of these steels may attain ~ 1000 MPa, and their elongation-to-failure is up to 15% [1]. It should be noted that the unified strength and ductility index of novel automotive steels ($\sigma_B \times \delta$) lies in the range $1 \div 2 \times 10^4$ MPa $\times\%$. Thus, an increase in strength can be achieved by a reduction in ductility. Even the application of the most advanced methods of microstructural design and thermomechanical processing for the development of advanced low-alloyed steels cannot overcome the “banana”, delimited by $\sigma_B \times \delta = 1 \times 10^4$ MPa $\times\%$ at the lower bound and $\sigma_B \times \delta = 2 \times 10^4$

Corresponding author: P.S. Kusakin, e-mail: kusakin@bsu.edu.ru

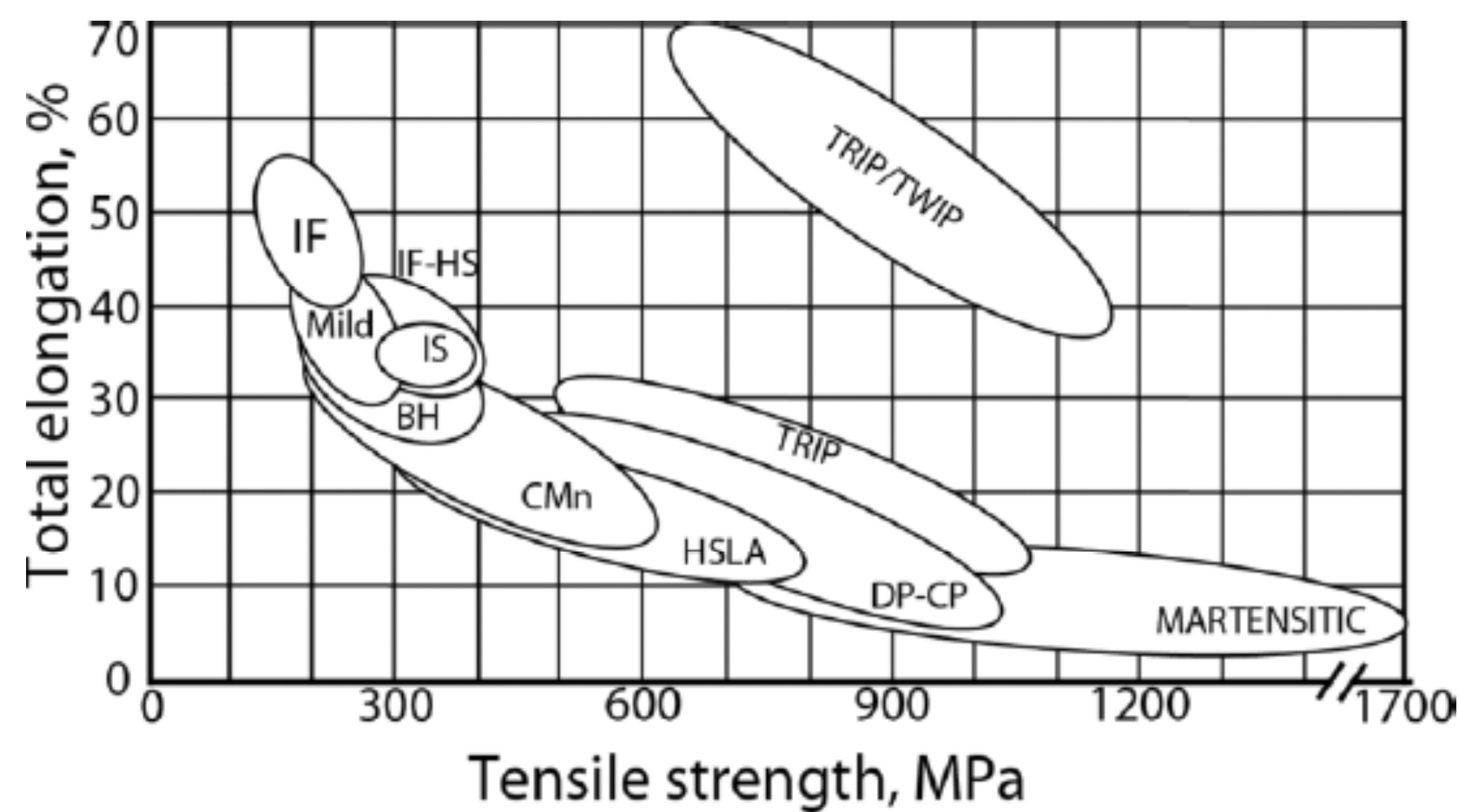


Fig. 1. Strength-ductility relationships for low carbon, high strength, advanced high strength and high Mn steels.

MPa×% at the upper bound [1,2]. Changes in the TMP and alloying additives may provide the appropriate combination of ductility and UTS but could not increase the $\sigma_B \times \delta$ term.

A new class of automotive steels was developed by POSCO, South Korea in the early 2000s. These steels have quite a different microstructural design. Martensitic transformation (TRIP) or deformation twinning (TWIP – twinning-induced plasticity) may take place in these steels in the fully austenitic matrix during deep drawing [2]. In TRIP steels, the Mn content is below 18 mass.% and the $\sigma_B \times \delta$ term ranges from 3×10^4 MPa×% to 4×10^4 MPa×%. TWIP steels have Mn contents between 18 and 32 mass.% and their $\sigma_B \times \delta$ values can reach $5 \div 6 \times 10^4$ MPa×%. Therefore, TWIP steels exhibit a superior combination of ductility and UTS that make them highly feasible for the automotive industry. Sheets produced by TMP before deep drawing may exhibit ductility of ~100% and $YS \geq 650$ MPa. Commercial implementation of these steels started from the use for structural elements of Luxury class vehicles with subsequent expansion to the production of medium-class models. At present, first-generation TWIP steels have already been commercialized for premium-class automobiles such as Volkswagen Touareg and Porsche Cayenne.

Advanced plasticity in comparison with the other automotive steels (Fig. 1) makes it possible to produce oddly shaped parts with fewer numbers of operations.

The present review discusses the fundamentals of the twinning-induced plasticity effect and deep drawing, as well as the relationships between TMP, microstructure and mechanical properties of high-manganese steels with the TWIP effect.

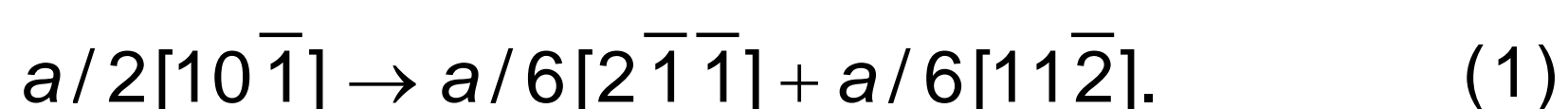
2. HADFIELD STEEL AND DEFORMATION STRENGTHENING MECHANISMS

The first austenitic high-Mn steel with a microstructural design similar to modern TWIP-steels was invented in 1888 by Sir Robert Hadfield [3]. This steel has a carbon content of 1.0-1.4 wt.% and a manganese content ranging from 11 to 15 mass.%; standard heat treatment of this steel includes homogenization at 1050-1100 °C followed by water quenching to avoid precipitations of grain boundary carbides. In the heat treated condition, this steel provides an excellent combination of strength, ductility and toughness: $YS = 360-380$ MPa, $UTS = 780-950$ MPa, elongation-to-failure of 34-53%, $KCV_{20C} = 170$ J/cm², $KCV_{-196C} = 7$ J/cm² [4]. The main feature of this steel is extensive deformation strengthening from 370 MPa to 950 MPa. At the same time, the hardness increases from 190 HBW in the quenched condition to 500 HBW after rupture. Superior deformation strengthening provides high wear resistance.

An unambiguous interpretation of the high ductility of Hadfield steel was given recently [5-10]. However, numerous aspects of its deformation behavior still remain unclear. This steel has a low stacking fault energy (SFE) of ~23 mJ/m², allowing the occurrence of deformation twinning at low strains. This fact distinguishes this steel from other fcc metals with low SFE values. The deformation-induced twin boundaries gradually reduce the effective glide distance of lattice dislocations, which results in the “dynamical Hall-Petch effect” [11]. In addition, the formation of dislocation boundaries can occur in Hadfield steel, which contribute to the structural hardening in a similar manner as high-angle boundaries [12,13]. However, the formation of dislo-

cation boundaries has a much lower contribution to overall deformation strengthening in comparison with twin boundaries [12].

High carbon content in the austenitic matrix reaching a concentration up to 7 at.% provides solid solution strengthening. However, the effect of strong saturation of austenite by carbon is rather small because carbon efficiency as a strengthening agent for an fcc lattice is significantly lower than for bcc [14]. Solid solution strengthening contributes to an increase in YS and through the stress for the onset of deformation twinning. At the same time, no effect of solid-solution strengthening on strain-hardening was found. The thermodynamically stable C-Mn atomic pairs were found to form in austenite on dislocation cores, what may cause either a static (SSA) or dynamic (DSA) strain aging and significantly contribute to hardening during deformation. At present, it was established that Hadfield steel exhibits the Portevin-Le Chatelier (PLC) effect [4,15,16] of type B with oscillation amplitude increasing from ~20 MPa at low strain rates to ~80 MPa at high strain rates. It is known [17-19] that stress amplitude is nearly equal to the solid-solution hardening value caused by DSA. This was confirmed for Hadfield steel by theoretical calculations [16]. The following mechanism has been proposed to explain the ultra-high strength increment originating from DSA [16]. In Hadfield steel, the interaction between Mn and C atoms leads to the ordering: carbon occupying the octahedral interstitial sites, and manganese atoms occupying the six nearest neighbor sites to thus form an octahedral cluster. The SFE value is low slip in Hadfield steel and is carried out by the movement of partial dislocations dissociated according to following reaction (1):



The movement of the first partial dislocation shifts the Mn atom just above the C atom located in the octahedral pore, creating a Mn-C couple with a very high binding energy [16]. This pair is a very strong local obstacle to the passage of the dislocation. For the glide of the second partial dislocation to pass through this obstacle to restore the original fcc structure and destroy the CMn_6 octahedral cluster, a significant stress increment is required [16]. This yields an appearance of a very high oscillation value up to 80 MPa on the σ - ϵ curve. Disordering leads to a reduction of the stress required for the movement of each subsequent dislocation in the same slip plane, which promotes planar glide in Hadfield steel. Hadfield steel is a cast material state. Recent successful attempts were made to develop

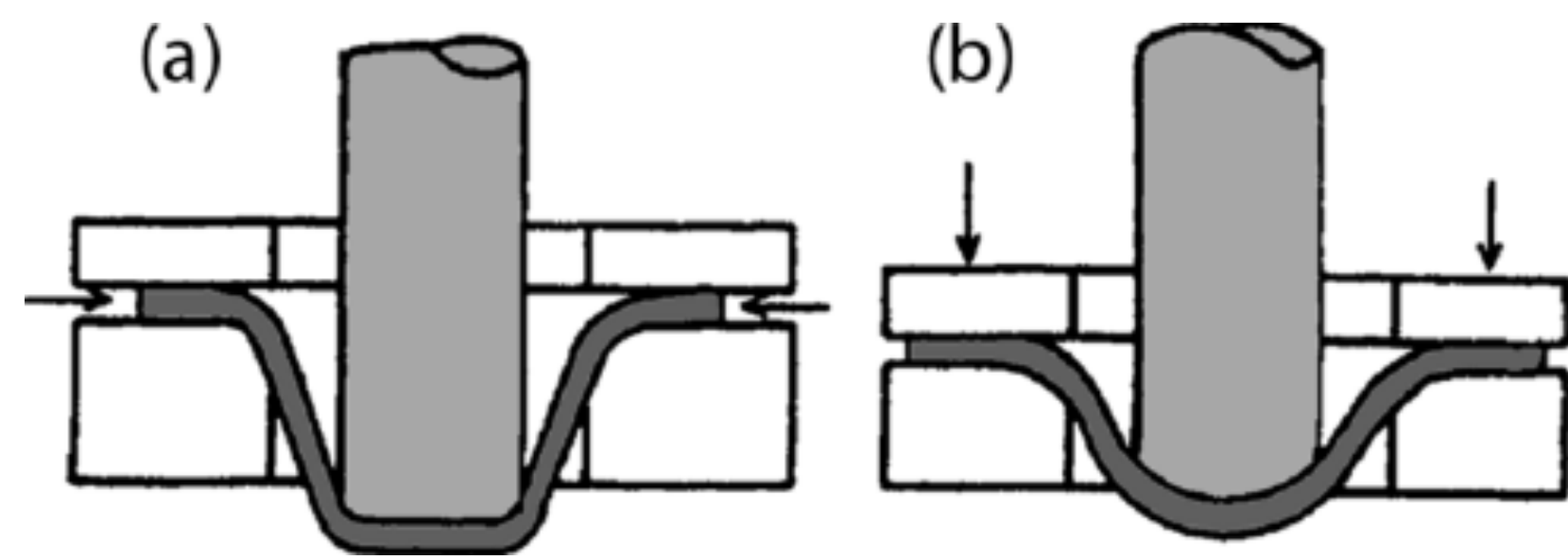


Fig. 2. (a) Deep drawing; (b) stretch forming.

wrought steel with a microstructural design like Hadfield steel with feasibility for the fabrication of thin sheets by hot and cold rolling.

3. MECHANICAL BEHAVIOR AND DRAWABILITY

In contrast with cast Hadfield steel, the main requirement to wrought sheet automotive TWIP steels is the ability for deep drawing at room temperature [20]. Deep drawing is the first step in the processing route of car body components. Formability is dependent on the mechanical behavior and the anisotropy of ductility attributed to the crystallographic texture. It is now generally accepted that, for many applications, the cold formability of sheet steel may be resolved into two separate but related components, namely as drawability and stretchability. The drawability of a steel is its ability to be drawn in to make a component without local necking or splitting, whereas the stretchability of a steel is its ability to be stretched to form a component, again without local necking or splitting. Stretching involves major and minor strains in the plane of the sheet that are both positive, whereas drawing involves major and minor strains, one of which is positive and one of which is negative. Many applications, however, involve both drawing and stretching. Therefore, both abilities for drawing and stretching are important for attaining high formability. A simple test to qualify the deep drawability consists of forming flat-bottomed cylindrical cups from circular blanks, as illustrated in Fig. 2a. The maximum ratio between the circular blank diameter and the punch diameter that may be drawn in a single stage to form a cylindrical cup without necking or splitting is a measure of the drawability of the steel. This ratio is called the limiting drawing ratio (LDR) and values of ~2.5 are attained for advanced automotive steels.

A simple measure of the stretchability may be obtained by using a hemispherical punch to form a circular dome, as indicated in Fig. 2b. The flange of the circular blank is prevented from being pulled in by the use of a draw bead or by using sufficient blank holder pressure. The maximum ratio of dome

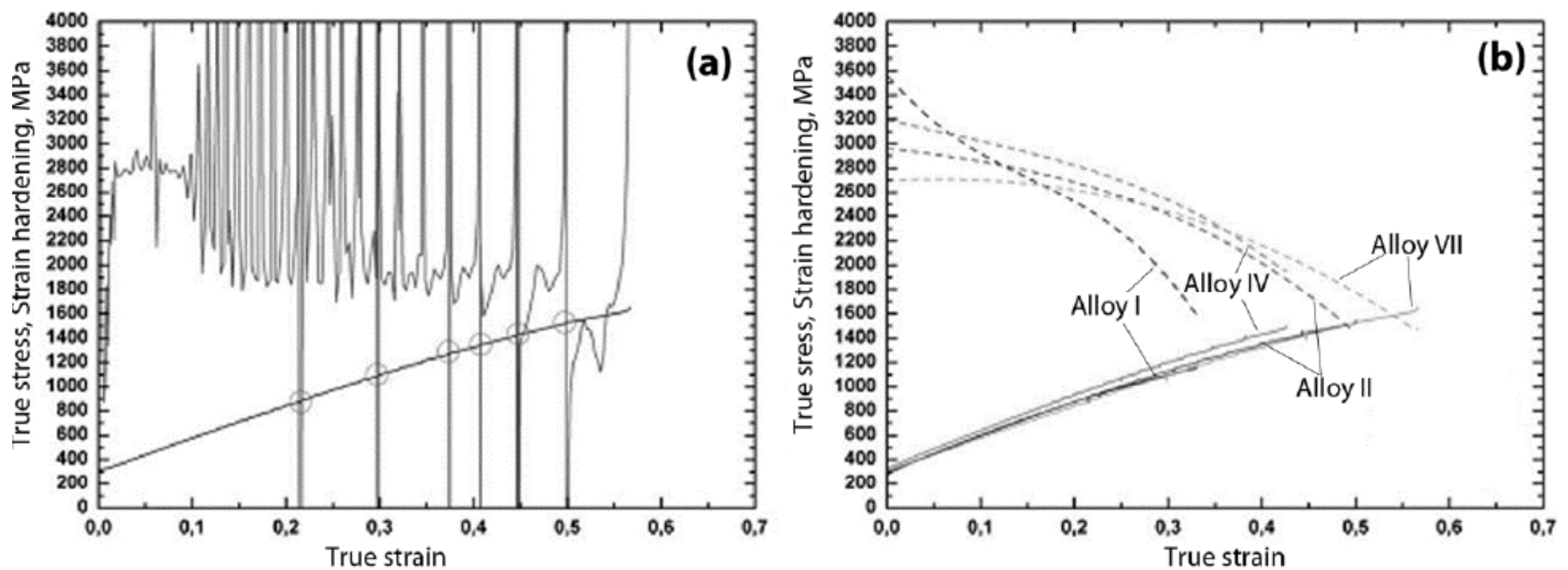


Fig. 3. (a) Plot of flow curve and (unsmoothed) hardening curve of alloy VII. Considère criterion is matched at least six times (red circles) in the strain range from 0.2 to 0.5. (b) Plot of flow curve and smoothed hardening curve of the evaluated materials. Considère criterion is not matched for alloys I and IV.

height to dome diameter at the moment of necking or splitting is a measure of the stretchability of the steel. A similar test, called a hydraulic bulge test, may be used, employing oil under pressure to form the dome. In this case, the result would not be influenced by friction. In these tests in which the shape of the dome is circular, the strain at the top of the dome is almost the same in two directions at right angles. The strain, therefore, is said to be balanced biaxial strain.

The general requirement in terms of the mechanical behavior of automotive steels is the stability of plastic flow that is provided by suppression of necking owing to a high strain hardening coefficient [21,22]. For most materials, the necking occurs only when UTS is attained [23].

Almost all deformation processes occur in a localized manner thereafter in the necked region until the onset of ductile fracture. Considère [24] treated this phenomenon mathematically by focusing on the point of plastic instability at which the load vs. strain curve shows a maximum value. The maximum load condition coupled with a requirement of conservation of volume leads to the following condition (2):

$$\sigma = \frac{d\sigma}{d\varepsilon}. \quad (2)$$

In Eq. (2), σ is the true stress and ε is the true strain. After $\sigma > d\sigma/d\varepsilon$, the material becomes plastically unstable, i.e., prone to strain localization in the neck [25].

The Considère criterion assumes a homogenous distribution of strain and a homogenous elongation up to the onset of necking. As the TWIP and TRIP steels show inhomogeneous deformation up to fracture, this concept seems rather inappropriate. The

plot of hardening and flow curves (Fig. 3) by Hoffmann et al. shows that the Considère criterion for necking is met at the early stages of deformation without failure of the sample [26]. Chemical compositions of the steels examined for achieving the Considère criterion (Fig. 3) are listed in Table 1. If a $\sigma - \varepsilon$ curve is fitted by a fourth order polynomial to eliminate the serrations and a hardening curve is reconstructed from this cleaned $\sigma - \varepsilon$ curve, the Considère criterion is not fulfilled up to failure. Therefore, the Considère criterion for necking after small strains is apparently attained.

On the other hand, it can be seen that a stress overload to initiate the propagation of a new deformation band leads to immediate fracture. This is either due to exhausted hardening capabilities within the areas of localized deformation, or the joining or intersection of two areas of localized deformation that cannot be absorbed by the material or due to preexisting damage (Fig. 3).

The second factor affecting the drawability of automotive steels is the anisotropy of strain hardening associated with the crystallographic texture [27]. This texture-induced anisotropy may take two forms. The first form is termed planar anisotropy; the flow properties in the sheet plane vary with direction. In the second form, an appropriate texture introduces a differential strengthening between the 'in-plane' and 'through-thickness' directions; such an effect is referred to as normal anisotropy. The criterion for drawability is given by the ratio of the true strains in the width and thickness directions (the r value):

$$r = \frac{\varepsilon_w}{\varepsilon_t}. \quad (3)$$

Table 1. Chemical composition of the high-Mn steels examined.

Alloy	C	Si	Mn	P	S	Cr	Mo	Ni	Type of steel	Calculated SFE, mJ/m ²
I	0.315	0.066	22.79	0.0073	0.0012	0.0016	0.014	0.037	TRIP	17
II	0.573	0.174	23.21	0.009	0.0002	0.31	0.019	0.0381	TWIP	29
IV	0.594	0.103	18.4	0.0084	0.0005	0.016	0.02	0.037	TWIP	19
VII	0.714	0.059	23.5	0.0071	0.0071	0.016	0.01	0.039	TWIP	36

In the presence of planar anisotropy, the value of r varies with direction in the sheet plane and an average r value is used:

$$\bar{r} = \frac{r_0 + 2r_{45} + r_{90}}{4}, \quad (4)$$

where 0, 45, and 90 are the angles between deformation direction in sheet plane and the rolling direction. The \bar{r} value is a convenient measure of normal anisotropy and therefore of drawability. High values of \bar{r} correlate with good drawability. IF steels demonstrate the highest value of $r \sim 2.5$ and exhibit the highest drawability, making IF steels attractive for car body parts of almost any net shape. At the same time, the r values of TWIP steels are slightly more than 1. Accordingly, the drawability of these steels is provided by almost isotropic deformation hardening.

4. MECHANICAL PROPERTIES AND DRAWABILITY OF TWIP STEELS

The typical dependence of the strain hardening exponent, n , in the Ludwig-Hollomon Eq. (5) on the true strain described by following equation:

$$\sigma = K\varepsilon^n, \quad (5)$$

where σ is the true stress, ε is the true strain, K and n are the strength coefficient and strain hardening exponent, respectively, is shown in Fig. 4. The deformation stages are difficult to distinguish using σ - ε curves but can be clearly seen from n vs ε and $d\sigma/d\varepsilon$ vs ε plots (Figs. 3 and 4). Values of the strain hardening exponent and strain hardening rate increase and decrease, respectively, up to $\varepsilon \sim 0.25$ because the increments of dislocation density and twin portion slow down with strain. This is the first stage. At the second stage and upon further strain, the strain-hardening may remain nearly unchanged or slightly decrease. Insignificant increases in the density of dislocations and the twin portion take place [28,29]. At the third stage, the onset of extensive necking corresponds with the occurrence of a drop strain hardening.

In a significant number of studies [30-34] noted that, despite the high elongation-to-failure of TWIP steel, the rupture of specimens in tension occurs without visible necking. The steels show low reduction in areas typical for brittle materials; fracture occurs by shearing ("slant fracture"). X-ray microtomography of TWIP steel tensioned to failure showed the presence of large chains of voids along the previous rolling direction [34]. Cavity volume at-

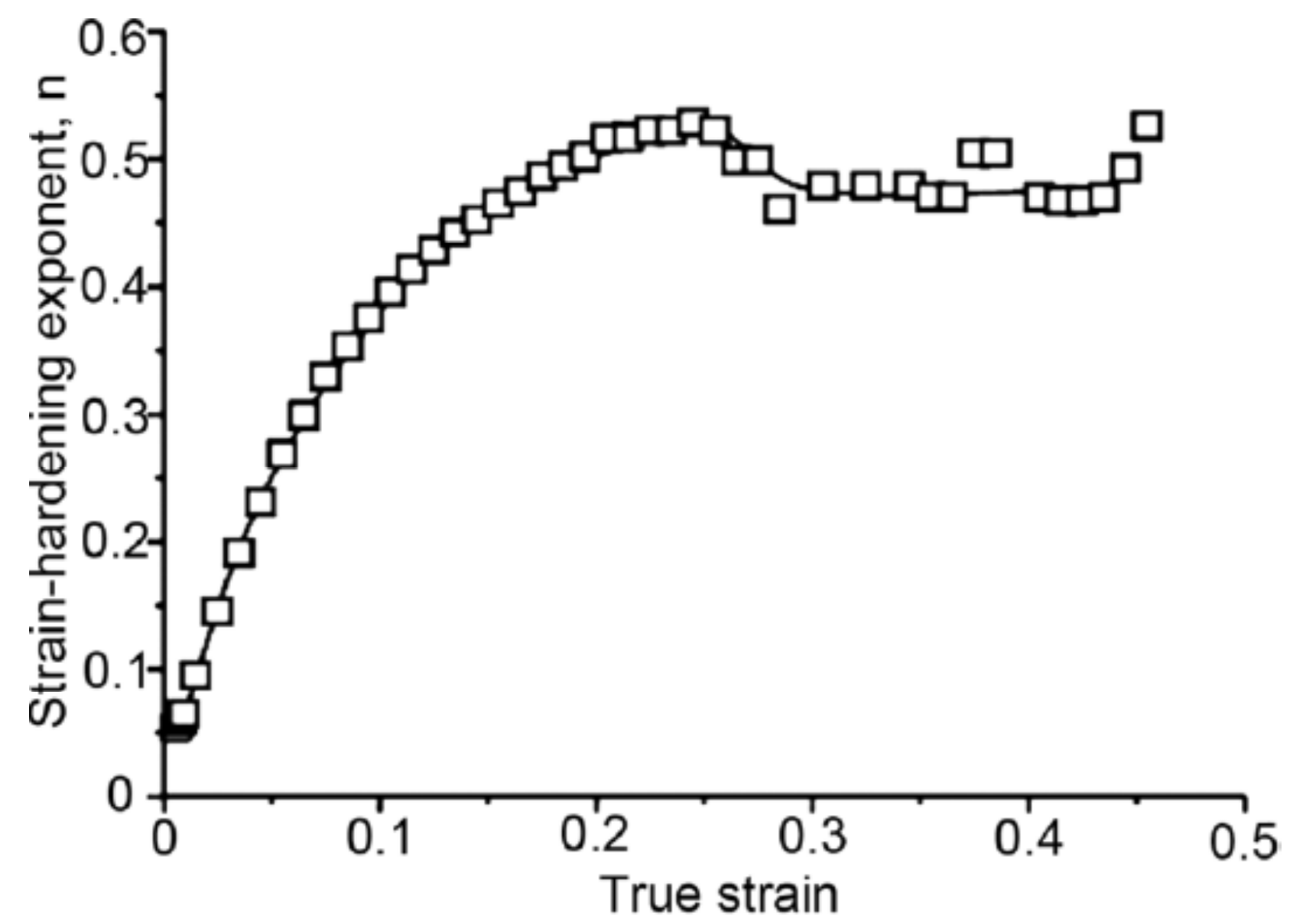


Fig. 4. Dependence of strain-hardening exponent on strain for the Fe-18Mn-0.6C-1.5Al steel.

tains a relatively high value of 0.06%, which initiates crack propagation. Therefore, fracture initiation of TWIP steel occurs in manner typical for the high-temperature fracture of superplastic materials through the coalescence of voids [35]. Crack propagation occurs in a ductile manner; fine dimples are observed at fracture surfaces.

There are no works dealing with the consideration of failure criterion in TWIP steels. The character and mechanism of fracture in pure aluminum, Al-Mg alloys and TWIP-steels are similar [30-34,36,37]. Therefore, the failure criterion developed for Al and Al-Mg alloys [36,37] can be applied to establish one for fracture initiation in TWIP-steels. It was proposed [36,37] that there is a critical dislocation spacing of ~ 8 nm beyond which the material loses the ability to undergo plastic deformation, plastic flow becomes unstable and failure occurs.

The orientation dependence of the normal anisotropy of Fe-18Mn-0.6C-1.5Al steel with strain [38] is shown in Fig. 5. The normal anisotropy of TWIP steels is relatively low, but their planar anisotropy can reach very high values. Accordingly, the main goal of TMP of TWIP steels is not an increase in the r -value but a reduction of the planar anisotropy. TWIP steels have extraordinary high strain hardening rates (Fig. 3b), so the unique performance and ductility could be achieved even in the presence of normal isotropy. At the same time, the planar anisotropy can cause the formation of festoons during the deep drawing process. Works on the drawability of TWIP steels [30,39-41] confirmed the conclusions made based on the mechanical behavior.

TWIP steels demonstrate high LDR. It should be noted that the deep drawing ability of TWIP steels is approximately 2-2.5 times higher than that of commercial high-strength steels such as DP, CP-

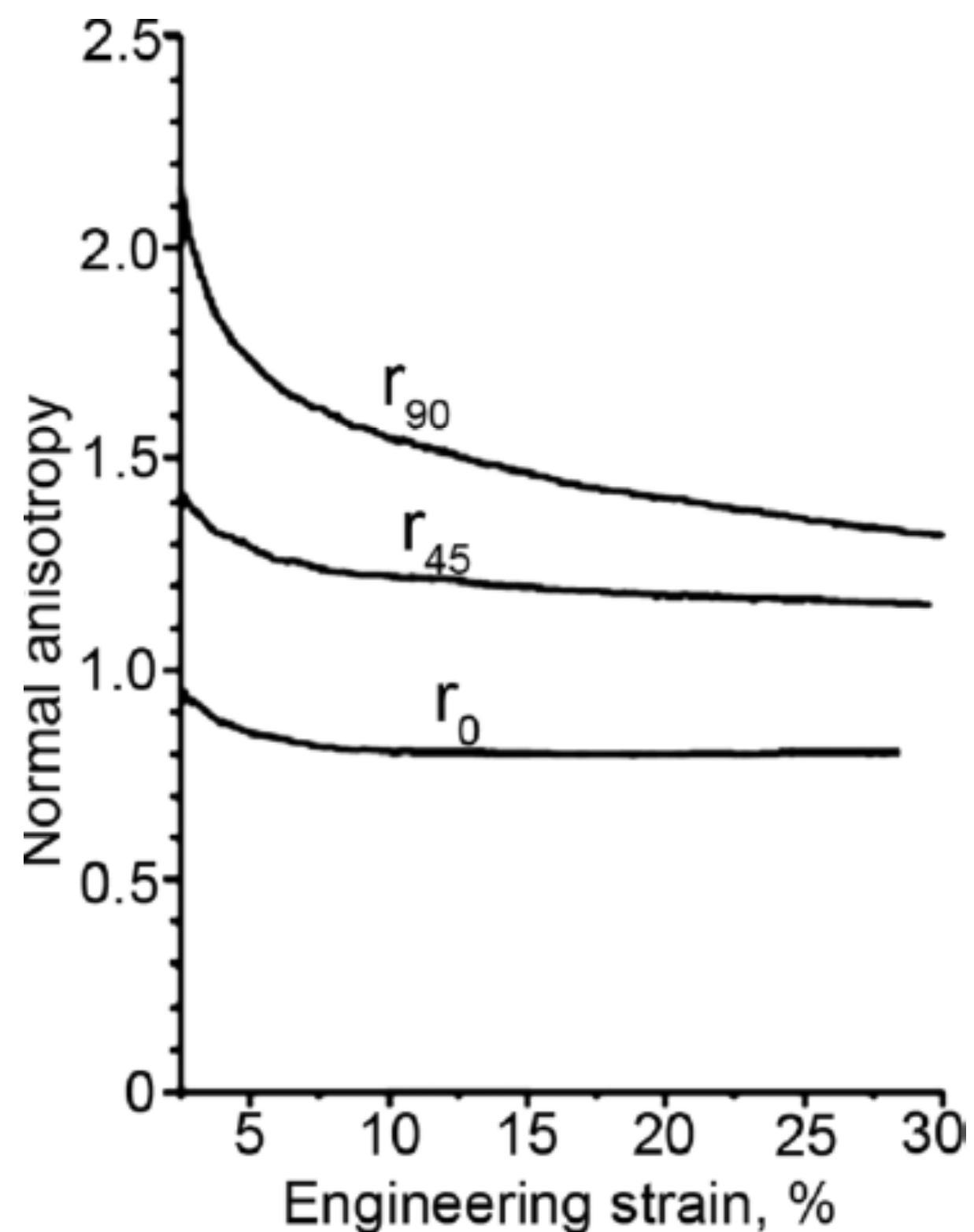


Fig. 5. Strain dependence of the normal anisotropy for tensile samples taken at 0°, 45°, and 90° to the rolling direction for the Fe-18Mn-0.6C-1.5Al steel.

K, and TRIP-RA but slightly lower than that of IF steels. Because TWIP steels are not intended for use as exterior car parts like IF steel, these data confirm the feasibility of the commercial implementation TWIP for the fabrication of structural inner elements of car bodies to replace the aforementioned high-strength automotive steels. The main shortcoming of TWIP steels compared to DP and TRIP-RA or CP-K steels is a low YS value. However, YS can be increased twice and more by preliminary cold rolling with a relatively low reduction, $\leq 20\%$. The effect of cold rolling on tensile behavior is shown in Fig. 6 [29]. Increasing the reduction of cold rolling highly increases the YS value. However, ductility drops and the strain hardening exponent, n , decreases from 0.4 to 0.18. In addition, significant anisotropy in the tension behavior appears. As a result, extensive cold rolling decreases the drawability (Fig. 7). However, cold rolled TWIP steels exhibit higher YS values and better drawability than DP steels, determined by the Erichsen test [42] (Fig. 7). Therefore, TMP is an effective route to the production of high-strength TWIP with sufficient formability.

TWIP steels are susceptible to a special type of rupture - delayed fracture (DF). DF appears readily in the deep drawn cup as deep edge cracks after a certain time, varied from 1 months to 200 days after the cup has been drawn. The edge of a fully drawn cup is subjected to residual tensile hoop stresses. The reasons for this phenomenon are still not clarified, but Kim et al. [43] have suggested hydrogen embrittlement under the residual stresses as the cause of delayed fracture. Data for the deep draw-

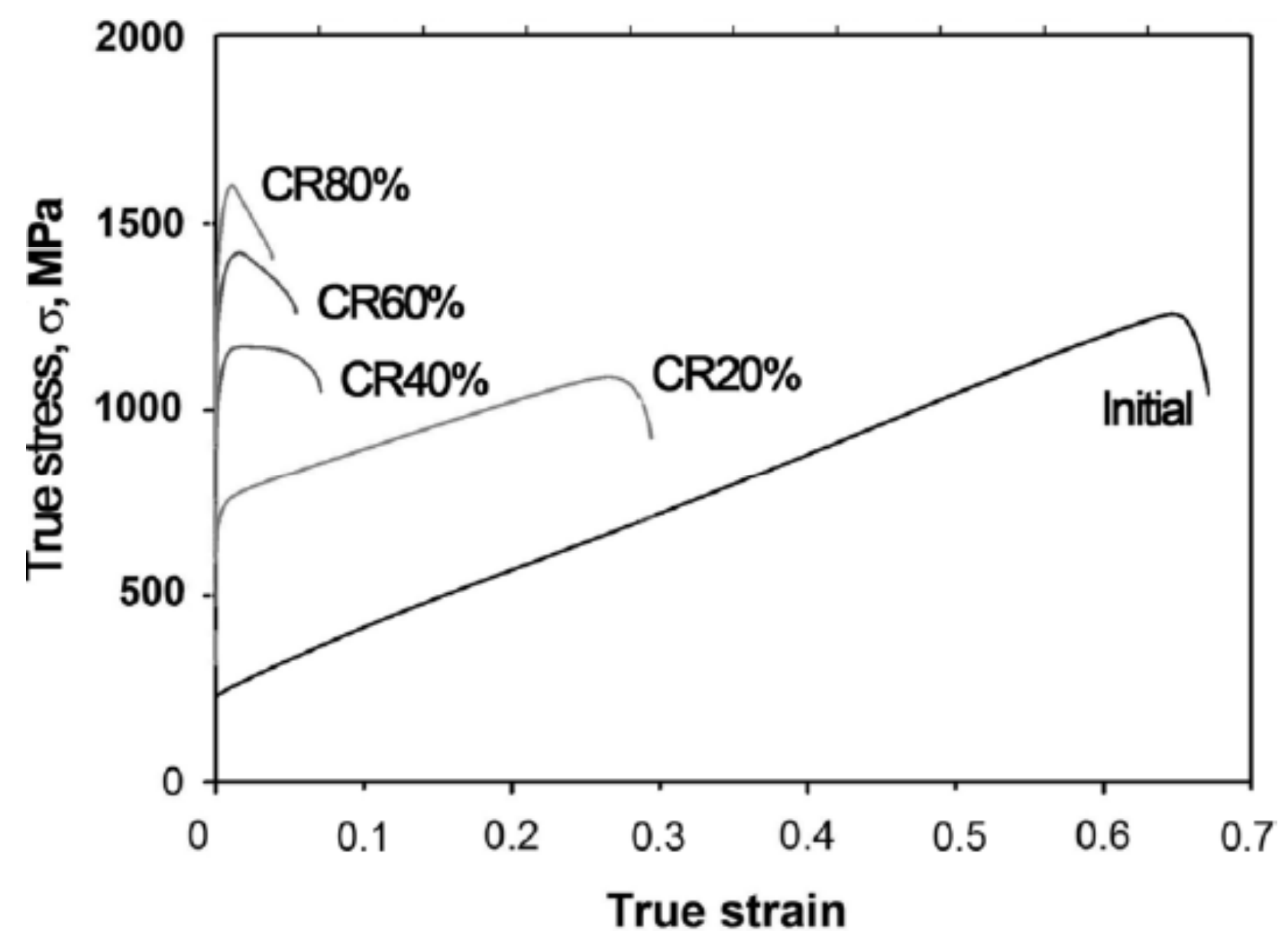


Fig. 6. True stress versus true strain curves for Fe-23Mn-0.3C-1.5Al TWIP steel as a function of cold rolling reduction.

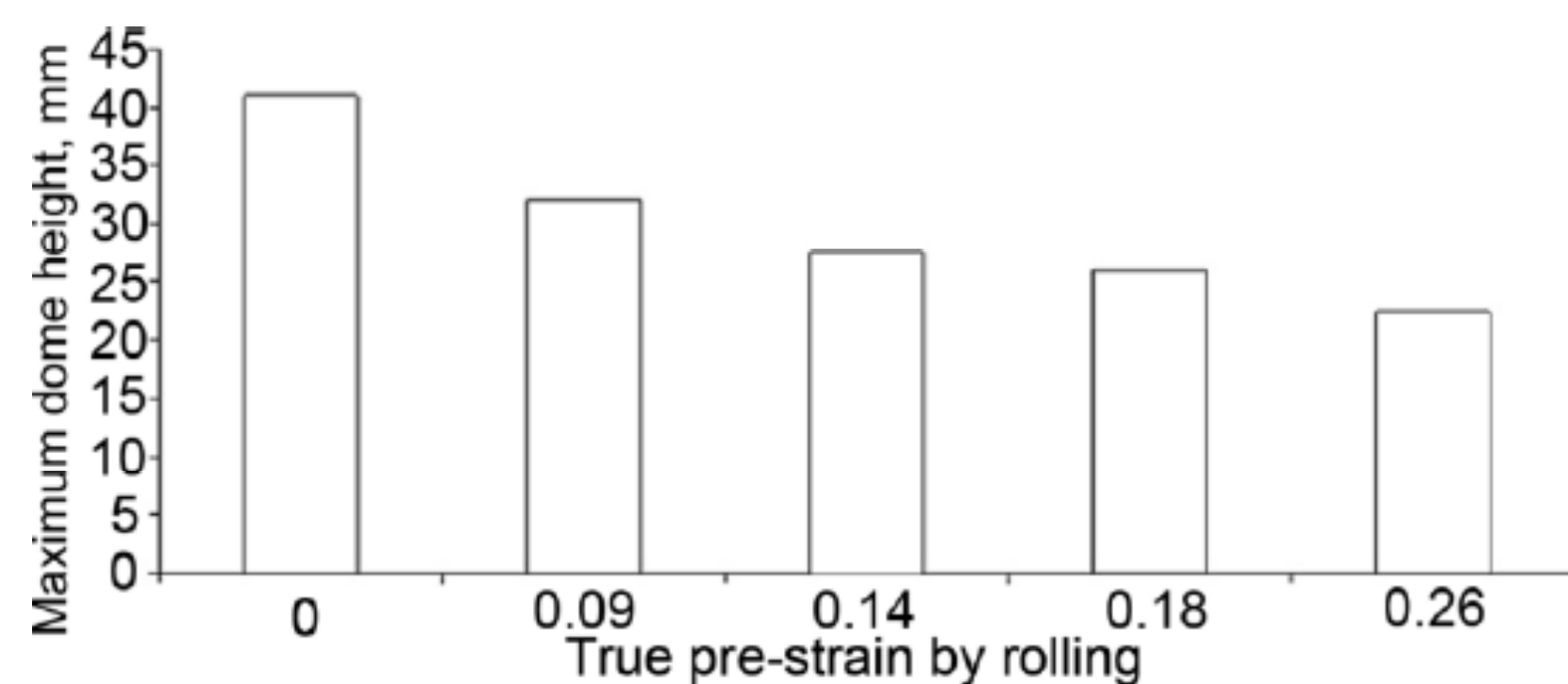


Fig. 7. Effect of prestraining of Fe-22Mn-0.6C on the maximum dome height in a hemispherical expansion test.

ing of Fe-(15-18)% Mn-0.6% C steels with and without Al additions support this conclusion [43]. It was shown that Al additives to TWIP steels prevent DF (Fig. 8).

This effect of Al on DF can arise from the fact that Al additions increase the SFE, thereby suppressing residual stress, which may induce embrittlement due to the presence of small amounts of solute hydrogen. This suggestion was also supported by Jung et al [44], where the hydrogen embrittlement of TRIP and TWIP steel after cathodic hydrogen charging was compared. They report that Fe-15% Mn-0.45% C-1% Al and Fe-18% Mn-0.6% C TWIP steels, with and without Al-additions, contained less hydrogen and were much more resistant to embrittlement than TRIP steel after U-bend and cup drawing tests.

5. WORK-HARDENING OF TWIP STEELS

Modern TWIP steel can be divided into three types according to their chemical compositions: Fe-Mn-C system (Fe-(18-22)Mn-0.6C), Fe-Mn-C-Al (Fe-(18-22)Mn-0.6C-1.5Al) and Fe-Mn-Si-Al (Fe-(30-33)Mn-(1-6)Si-(1-6)Al). All TWIP steels have low YS values

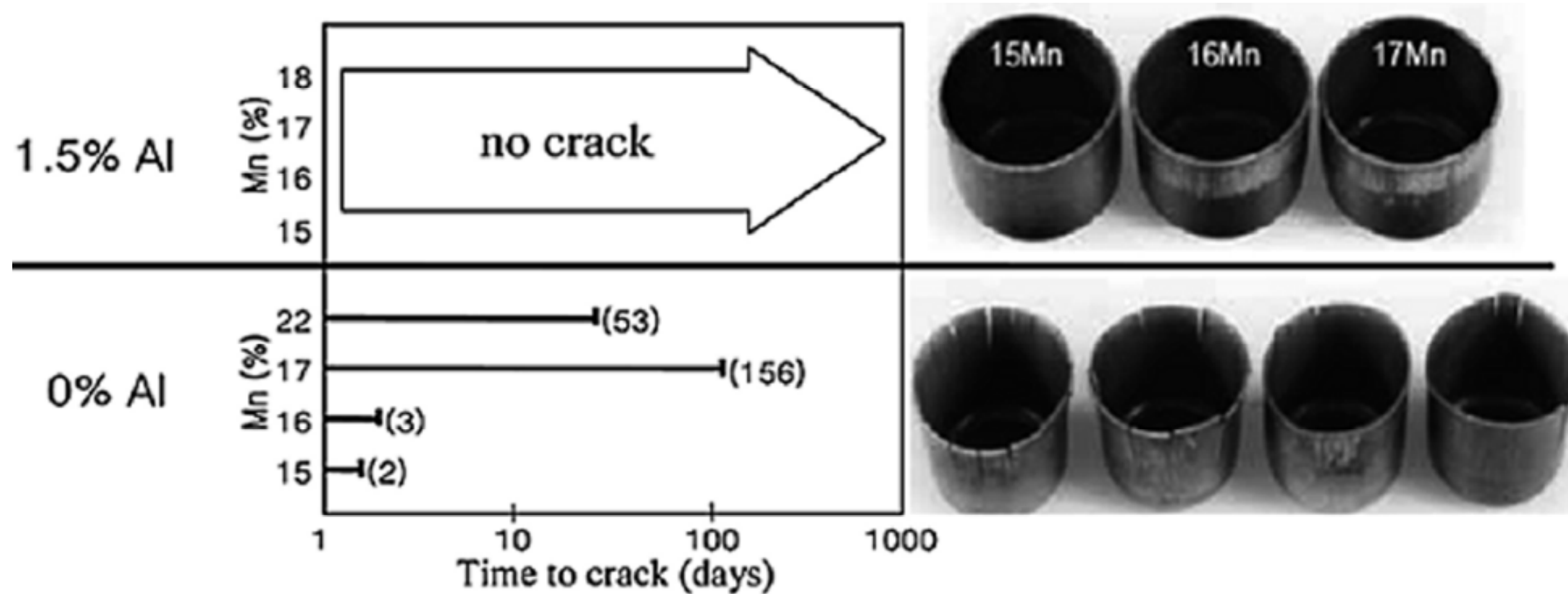


Fig. 8. Evidence of the delayed fracture suppression in deep drawn Fe-(15-18)%Mn-0.6%C TWIP steels by Al additions.

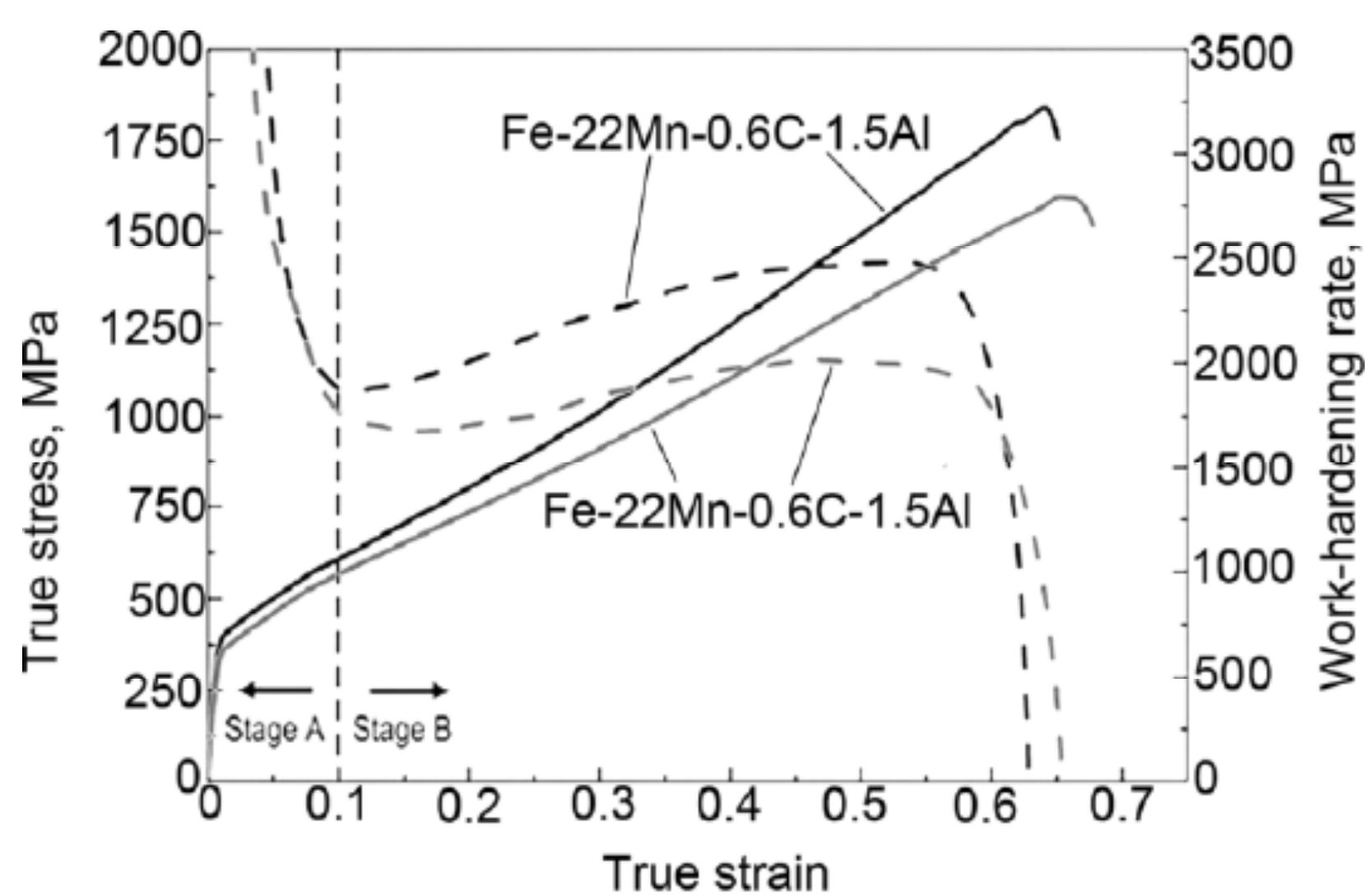


Fig. 9. The true stress–strain and work-hardening rate curves. The black and blue lines represent FeMnC and FeMnCAI TWIP steels, respectively, and the solid and dashed lines represent true stress and work-hardening rate, respectively.

and high values of UTS and ductility. YS varies from 250 to 300 MPa, UTS varies from 780 to 1350 MPa, and elongation varies from 50 to 110%. The Fe-Mn-C steels have the highest YS value among all TWIP steels. However, these steels exhibit DF. Fe-Mn-C-Al steels are characterized by a good combination of mechanical properties. The metallurgical process of these steels does not require the use of special techniques for melting and crystallization. Fe-Mn-Si-Al steels need complicated melting technology because the simultaneous addition of Si and Al leads to the formation of macro segregations, which cannot be removed by homogenization annealing, and induces hot cracks in ingots.

Stress-strain curves and the dependence of the strain-hardening rate for Fe-22Mn-0.6C and Fe-22Mn-0.6C-1.5Al steels at room temperature are shown in Fig. 9 [45]. It can be seen that Al additions reduce the strain hardening coefficient, $d\sigma/d\varepsilon$, and the UTS values. At the same time, the uniform elongation and total elongation increase. In Fe-Mn-C-Al steel, unlike Fe-Mn-C steel, plastic instability

appears at flow stress values slightly below the Considère criterion. Therefore, plastic instability attributed to PLC is not important for the deep drawability of these steels.

The three aforementioned stages of plastic flow could be distinguished in Fe-Mn-C(-Al) steels. At the first stage, the initial high hardening rate, $d\sigma/d\varepsilon$, decreases sharply with strain. At the second stage, the $d\sigma/d\varepsilon$ value remains nearly unchanged or may even increase. At the third stage, a sudden drop of work hardening induces plastic instability leading to failure [45]. Al additions affect the mechanical behavior through the suppression of secondary deformation twinning: in a Fe-22Mn-0.6C steel at a fixed strain $\varepsilon \sim 0.2$, the twins are thinner (17 ± 5 nm) than in a Fe-22Mn-0.6C-1.5Al steel (120 ± 66 nm). After failure, the fraction of grains containing secondary deformation twins with a thickness of 20 nm or less are ~ 35 and $\sim 5\%$ in the Fe-22Mn-0.6C and Fe-22Mn-0.6C-1.5Al steels, respectively.

Four stages of strain hardening were distinguished in Fe-(22-28)Mn-3Si-3Al steels (Fig. 10): stage 2 is divided into a, b, and c intervals for the steel with 22% Mn [46]. In these steels, the strain hardening coefficient decreases monotonically after the first stage, in contrast to Fe-Mn-C and Fe-Mn-C-Al steels [46-49]. This feature of tension behavior is associated with the formation of ε -martensite in 22% Mn steel, resulting in a slight decrease in the strain-hardening in stage 1 as in the steels with no Si additions or in the 25% Mn and 28% Mn with Si additions. Therefore, atypical strain hardening behavior is attributed to concurrent twinning and the formation of strain-induced martensite. This allows stage 2a to be specifically distinguished, where an intense deformation twinning starts to occur. Further formation of ε -martensite plates results in their thickening and a corresponding decrease of the strain hardening rate (stage 2b). The formation

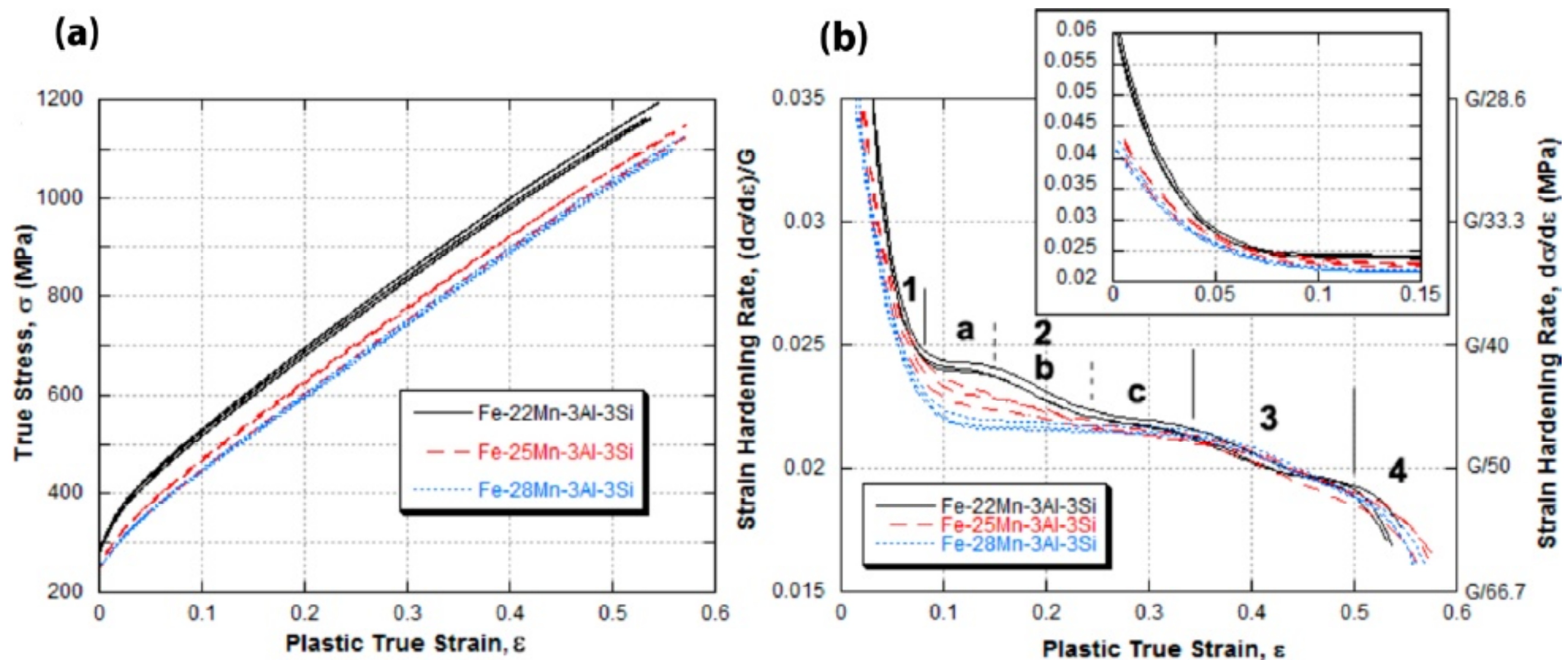


Fig. 10. (a) True stress vs. plastic true strain and (b) strain-hardening rate vs. plastic true strain for the Fe-22/25/28Mn-3Al-3Si steels at RT. The insert shows the strain hardening rates at low strains.

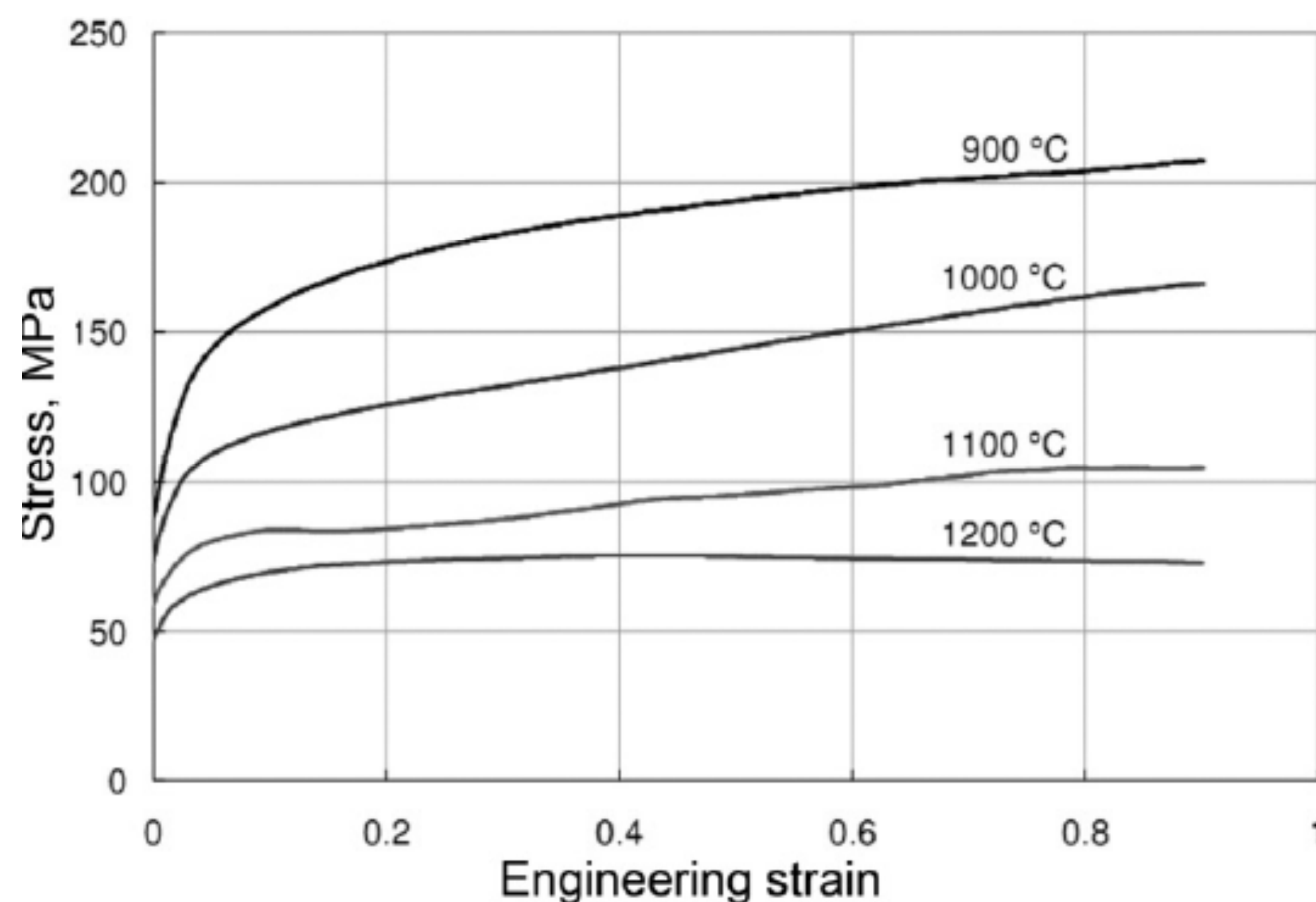


Fig. 11. Flow curves of Fe-23Mn-0.6C steel under compression at temperatures between 900-1200 °C.

of the first ϵ -martensite plates decreases the mean free path of the dislocations, while further thickening does not reduce the mean free path significantly. The bend of the strain hardening curve in stage 2c is associated with a maximum rate of the ϵ -martensite formation. The work hardening coefficient of the 25% Mn steel is slightly higher than of the 28% Mn steel in a true strain range of 0.1 to 0.25 because of the ϵ -martensite formation in some grains. In 28% Mn steel, the normalized strain hardening coefficient of ~ 0.022 remains unchanged until the beginning of the third stage of strain hardening, which is associated with a decrease in the mean free path of the dislocations resulting from the formation of dislocation substructures and deformation twinning [49]. Upon further strain, the steels lose their ability to accumulate dislocations in the microstructure within ~ 20 nm structural elements delimited by twin boundaries, which results in a gradual decrease in the work hardening coefficient.

In contrast with deformation at ambient temperature, the hot deformation of TWIP steels does not result in significant strain hardening. For example, a gradual decrease of YS stress from 160 to 70 MPa takes place when increasing the temperature from 900 to 1200 °C under hot compression of Fe-23Mn-0.6C steel with a strain rate of 1 s^{-1} . In addition, the strain hardening coefficient reaches zero when increasing the temperature up to 1200 °C (Fig. 11) [40]. Accordingly, under hot working, the ductility of TWIP steels is lower than at room temperature, which is unusual for metallic materials. This fact manifests the key role of extensive strain hardening, $d\sigma/d\epsilon$, in the superior ductility of TWIP steels.

Moreover, a significant concurrent decrease of flow stress and tensile elongation is observed at temperatures up to 600 °C for Fe-23Mn-0.2C-2Al steel (Fig. 12a) [39]. This is also absolutely unusual for other materials. At 600 °C, no mechanical twinning occurs. Therefore, the Fe-23Mn-0.2C-2Al steel

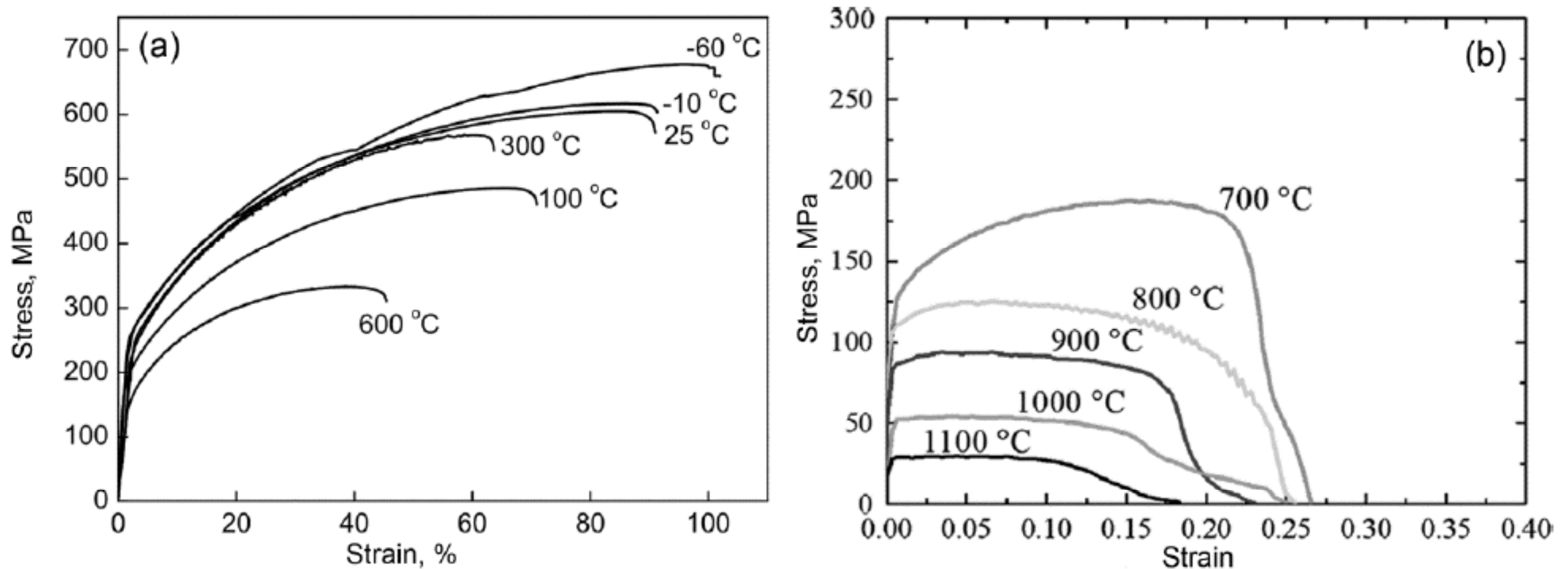


Fig. 12. (a) Stress-strain curves for Fe-23Mn-0.2C-2Al steel during tensile at temperature between -60 –600 °C and (b) Stress-strain curves for Fe-21Mn-1.3Al-1.5Si-0.5C steel during tensile at temperature between 700 - 1100 °C.

exhibits mechanical properties typical for austenitic steels [42] with “normal” strain hardening attributed solely to the increasing dislocation density with strain. This is distinctly different from the behavior at room temperature, where the mechanical twinning highly promotes the accumulation of lattice dislocations. Moreover, at 1100 °C, the Fe-21Mn-1.3Al-1.5Si-0.5C steel exhibits limited elongation-to-failure of about $15\pm 5\%$ despite low flow stress (40 ± 10 MPa) (Fig. 12b) [50,51]. The poor high temperature ductility of TWIP steels results from the lacking of both deformation twinning and dislocations accumulation and yields restricted workability of these steels at elevated temperatures.

6. TWINNING-INDUCED PLASTICITY

Deformation mechanisms of TWIP steels were examined in numerous works [52-56]. It was found that both twinning and dislocation slip in TWIP steels depend on the SFE value. The fundamental principle of the microstructural design of TWIP steels is as follows: alloying elements have to provide SFE values ranging from 20 to 40 mJ/m² [38]. Accordingly, the SFE value must be accurately predicted by means of advanced mathematical modeling methods and then confirmed experimentally. A stacking fault is formed by dissociation of a perfect dislocation into two Shockley partials. SFE is determined by the distance between the partial dislocations: a low SFE corresponds with a high distance between the partial dislocations [57,58]. Two experimental and two theoretical methods for the determination of SFE in TWIP steels are used. First, SFE is estimated by the measurement of partial dislocation separation width using a transmission electron microscope (TEM) [59,60]. The second experimental

method is profile analysis of X-ray diffraction line shape [61,62]. The ab-initio calculation method provides the most accurate match with the experimental data [15,58]. In addition, SFE may be less accurately predicted using a thermodynamic model [57]. Hirth [63] proposed an equation for the SFE calculation for fcc metals based on the thermodynamic approach:

$$SFE = 2\rho\Delta G^{\gamma-\varepsilon} + 2\sigma^{\gamma/\varepsilon}, \quad (6)$$

where $\Delta G^{\gamma-\varepsilon}$ is the free molar enthalpy of the transformation $\gamma\rightarrow\varepsilon$, ρ is the molar surface density of atoms in the {111} planes and $\sigma^{\gamma/\varepsilon}$ is the energy per surface unit of a {111} interface between γ and ε . Recently, Saeed-Akbari et al. [64] reviewed the expression (6), taking into account the influence of grain size:

$$SFE = 2\rho\Delta G^{\gamma-\varepsilon} + 2\sigma^{\gamma/\varepsilon} + 2\rho\Delta G_{ex}, \quad (7)$$

where ΔG_{ex} is the excess part of the SFE associated with the grain size.

The SFE of TWIP steel is a strongly temperature dependent parameter. Remy et al. [65] considered the temperature effect on the intrinsic SFE of a high-manganese austenitic steel (Fe-20Mn-4Cr-0.5C). He showed that the value of SFE increases due to a decrease in the size of the dislocation nodes with increasing temperature >300K. It was also stated that at $T \leq 300$ K, such temperature dependence is reversible but is irreversible in the temperature interval 300 - 390K due to pinning of dislocations by carbon atoms. The thermodynamic calculation of SFE, through the entropy variations between the fcc and hcp phases, and TEM observations consistently confirmed the trend of increasing values of SFE with temperature. The calculation of

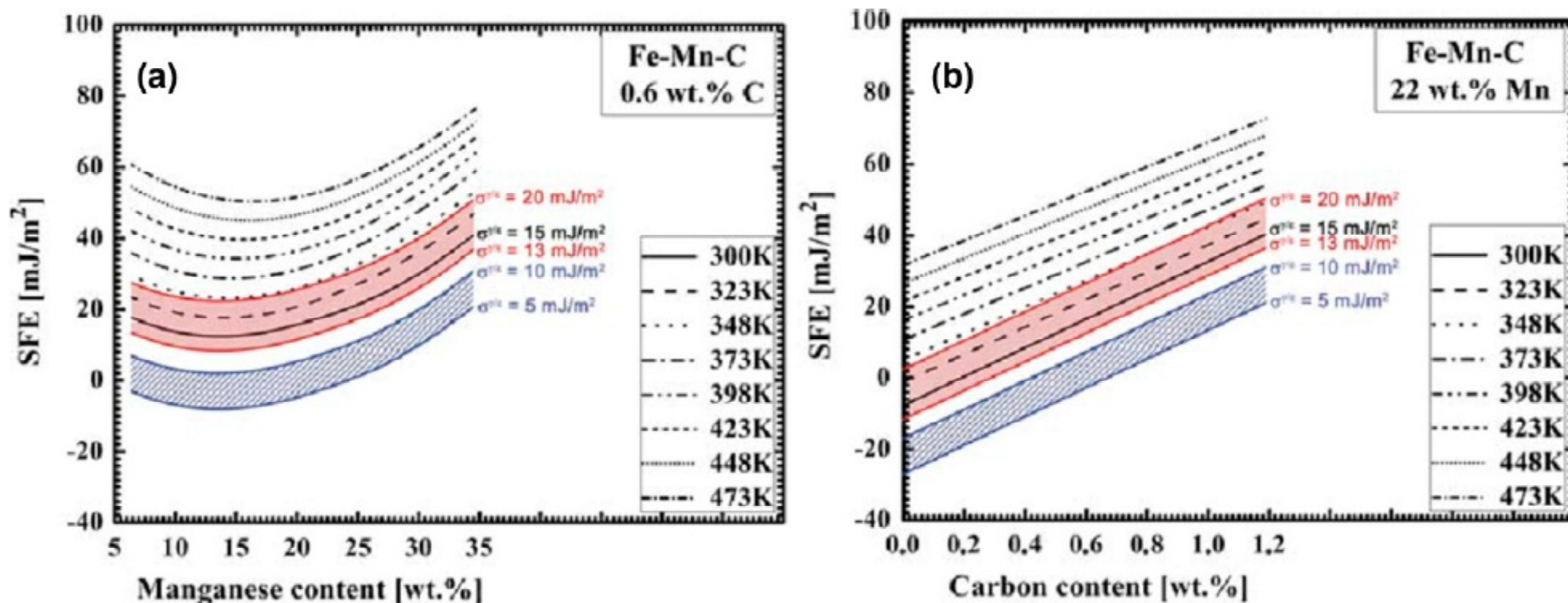


Fig. 13. (a) Isocarbon (0.6 wt.% pct) and (b) isomanganese (22 wt.% pct) SFE diagrams by increasing temperature. Movements of isocarbon and isomanganese lines at 300K are seen in both figures by changing interfacial energy.

SFE via the subregular solution model [64] gives a similarly increasing trend. Fig. 13, showing the isocarbon and isomanganese diagrams of 0.6 wt.% C and 22 wt.% Mn, respectively, demonstrates a polynomial trend of SFE with increasing Mn content and a linear dependence of SFE on C content. Moreover, the effect of temperature on the isocarbon lines is seen to be more crucial for lower manganese contents.

Dumay et al. [66] used a thermodynamic model to determine the influence of alloying elements on the SFE of Fe-Mn-C steels (Fig. 14a). They found that Cu and Al additions to Fe-22Mn-0.6C steel increase the SFE, while Si has a complex effect. Some authors report that Si additions increase SFE [61,66-68], while Lee et al. [69] found that Si reduces SFE by 4 mJ/m² per 1 or 1.5 wt.% in Fe-18% Mn-0.6% C TWIP steel. Cr reduces SFE [70]. Saeed-Akbari et al. proposed a model of SFE calculation for a Fe-Mn-C system [64] and later [71] expanded it for Fe-Mn-Al-C. They showed that Al additions provide a SFE value above 20 mJ/m² for TWIP steels with reduced contents of Mn and C. The influences of Mn, Al and C are shown in Fig. 14b. Sections of the plot in Fig. 14b at Al=0% and Al=1.5% are shown in Fig. 14c and 14d, respectively. It is shown that the same value of SFE can be obtained in TWIP steels with a balanced Mn/C ratio with different Al contents.

Because TWIP steels contain a large amount of Mn, which increases the solubility of nitrogen in the melt [14], these steels may contain up to 0.02 wt.%N. The effect of N on SFE of Fe-0.01% C-(20.24-22.57)% Mn-(2-3)% Si-(0.69-2.46)% Al and Fe-18Cr-10Mn-(N or N + C) steels up to over-equi-

librium concentrations of 0.52% was reported in previous works [72,73]. An almost linear SFE dependence on the (N+C) amount for Fe-18Cr-10Mn-(N or N + C) steel was recorded (Fig. 15).

The main purpose of the SFE studies for TWIP steel is to determine the alloying interval of the aforementioned SFE values in which austenite is susceptible to extensive mechanical twinning. Authors [74] showed that at SFE ≤ 16 mJ/m², the formation of hcp ϵ -martensite occurs, while SFE values beyond 25 mJ/m² retain a fully austenitic structure after intense plastic straining and the twinning occurrence after small strain. Allain et al. [54] found that mechanical twinning becomes the dominant deformation mechanism in the interval of SFE 12-35 mJ/m². At higher SFE values, no mechanical twinning occurs. Strain-induced ϵ -martensite appears at lower SFE, while in the SFE interval 12-18 mJ/m², the mechanical twinning and this martensitic transformation occurs in a sequential manner: deformation twinning promotes the formation of ϵ -martensite. The thickness of the ϵ -martensite plates and the deformation twins are nearly equal and can vary from 20 to 40 nm [29,40,49].

The SFE value of austenitic steels influences twinning not only because it is associated with the energy of twin boundaries [75,76] but mainly because the large separation distance between partial dislocations facilitates the formation of a twin embryo when the critical shear stress is reached [58]. The nucleation of twins in TWIP steel does not seem to be a homogeneous process. Instead, the nucleation stage in deformation twinning is closely related to prior dislocation activity, as the process always occurs after some amount of prior disloca-

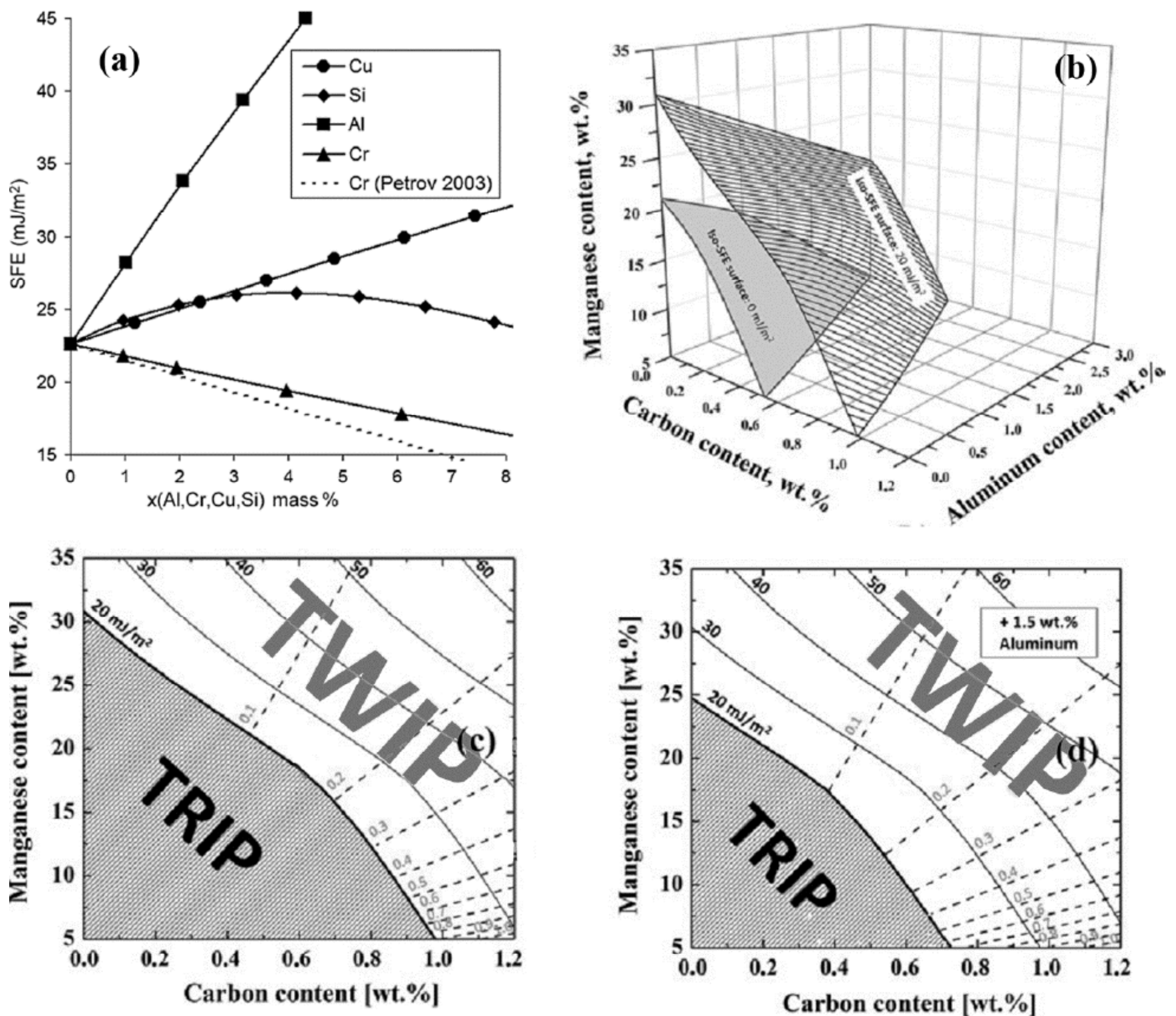


Fig. 14. (a) Predicted influence of alloying elements (Al, Cr, Cu, Si) on the SFE of Fe-22Mn-0.6C steel. (b) Effect of chemical composition on the SFE value of Fe-Mn-Al-C steels. (c),(d) Sections of (b) at Al=0% and Al=1.5%, respectively. Replotted from [66] and [71].

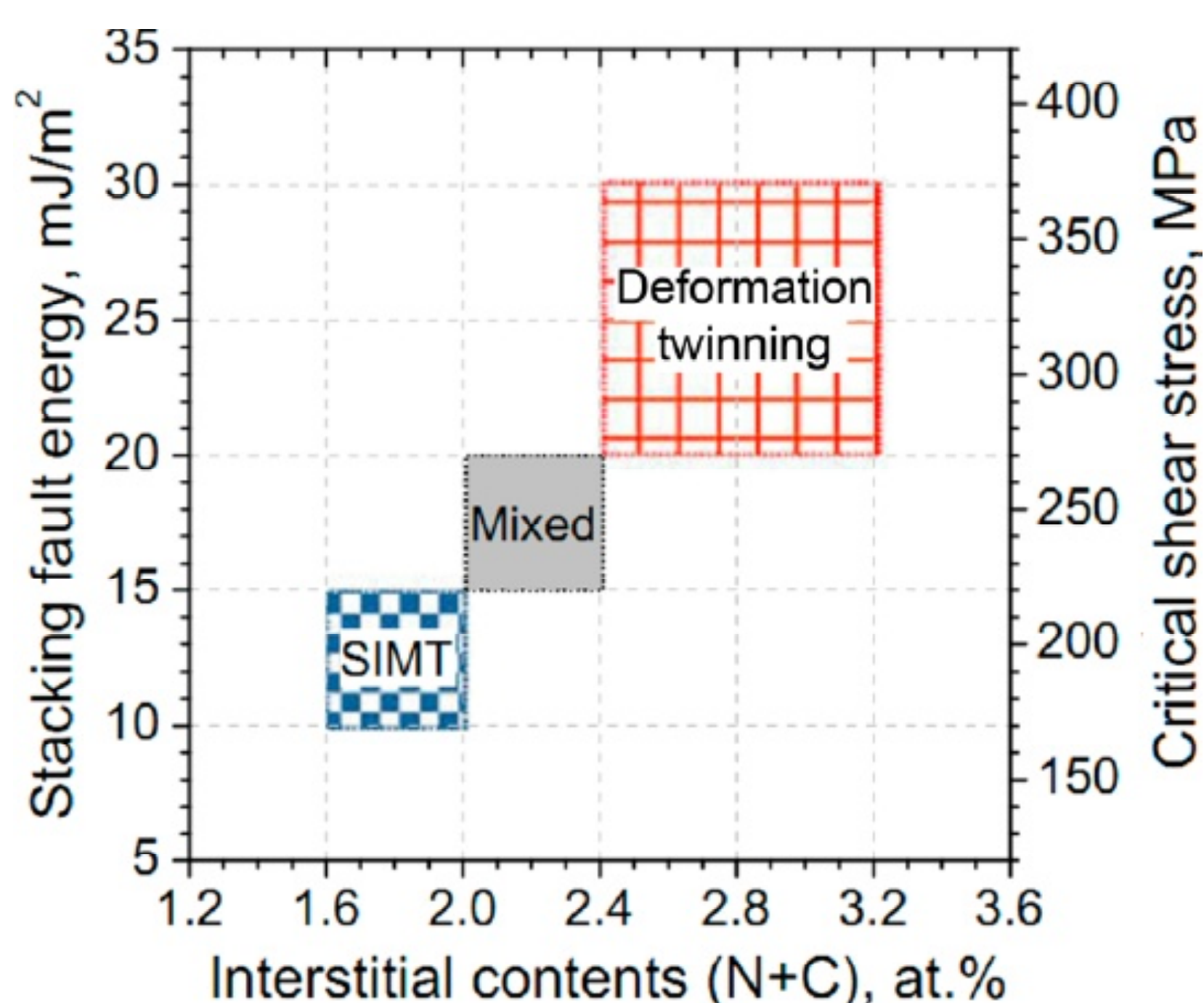


Fig. 15. Deformation microstructure-SFE-critical shear stress map of Fe-18Cr-10Mn-(N or N + C) alloys.

tion generation and dislocation-dislocation interactions on different slip systems. Twins are initiated in special dislocation configurations created by these interactions, generally resulting in multi-layer stacking faults that can act as twin nuclei. To date, several models of deformation twin nucleation, which can initiate twinning in TWIP steels, were developed. All of these mechanisms are based on the dissociation of a perfect dislocation into two partial dislocations followed by the subsequent movement of the head dislocation and anchorage of the second partial dislocation. The extension of stacking fault will produce a twin.

1) Venables [77] proposed a pole mechanism according to which a prismatic dislocation dissociates into a Frank sessile and a Shockley partial, creating a stacking fault (8):

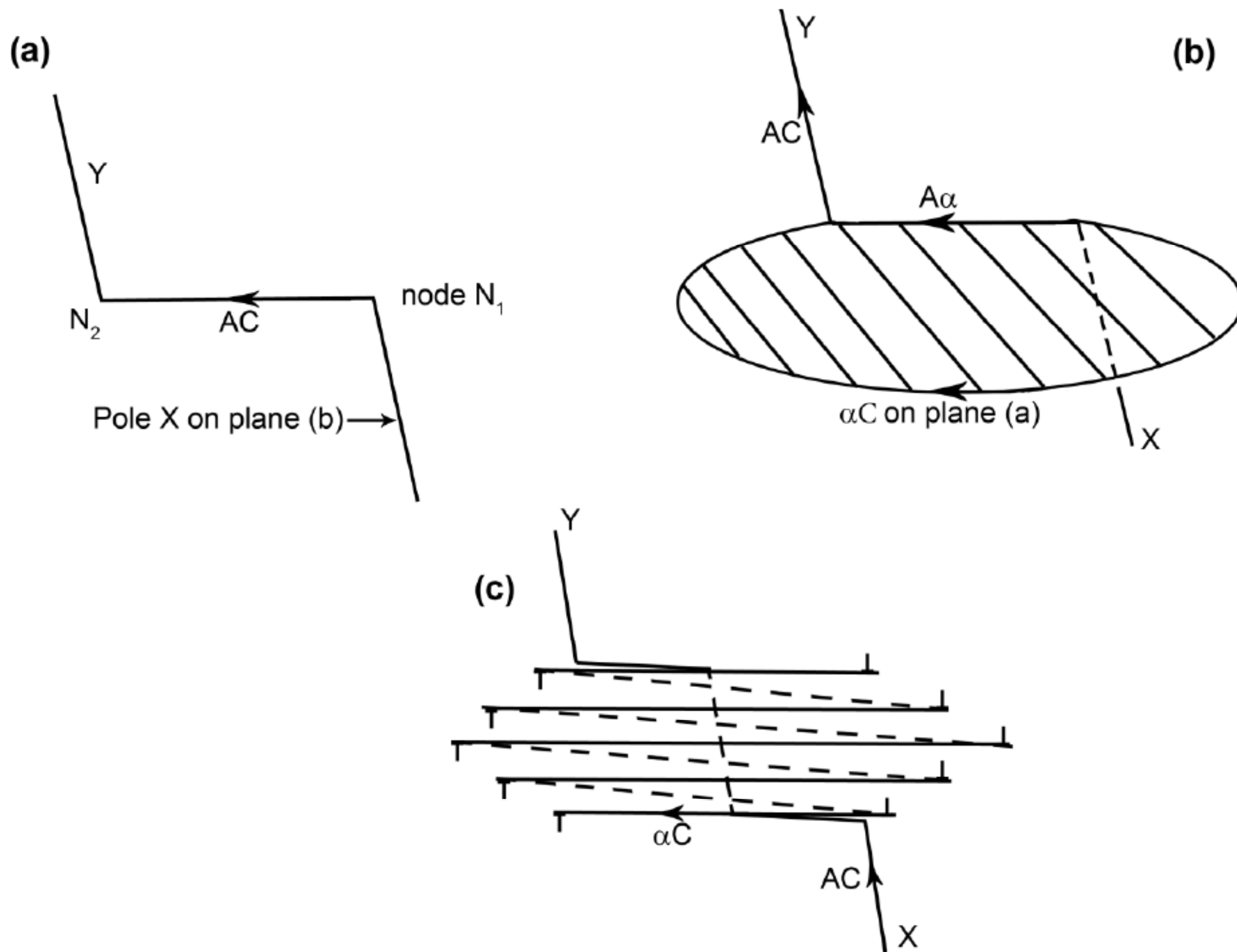


Fig. 16. Twin formation according to Venables (replotted from [68]). (a) the dislocation AC which is jogged along CB. (b) Dissociation of the jog to form a twinning dislocation αC . (c) formation of twin after operation of the source. The twinning dislocation is a continuous (left-handed) helical fault.



After one revolution about the pole, they recombine to form the original perfect dislocation, leaving behind a stacking fault layer. The perfect dislocation is free to glide prismatically to the neighboring close-packed plane, where the dissociation can again occur and the process can repeat itself. Repeated operation of the source on consecutive close-packed planes produces a twin. Fig. 16 illustrates the described mechanism. Here, $AC = 1/2[110]$, $A\alpha = 1/3[11\bar{1}]$ and $\alpha C = 1/6[112]$.

3) Cohen and Weertman [78] proposed a twin nucleation model whereby a twin is formed due to the dislocation pile-ups at Cottrell–Lomer locks by the dissociation of a perfect dislocation. The Shockley partial is formed in the conjugate slip plane and glides away from the sessile Frank partial, forming an intrinsic stacking fault. Many Cottrell–Lomer locks are created on parallel planes in a slip band, which become the source of multiple stacking faults. In order for a twin to form, these stacking faults must be on directly adjacent atomic planes. Twins produced in this manner would be imperfect, exhibiting a series of matrix and twin lamellae because not every twin plane in a large volume would have a

stacking fault. This reaction is not energy-effective because the dislocation energy remains constant, but Cohen and Veertman argue this by claiming that the appropriate stress factor is generated at the head of dislocation pile-ups.

4) Fujita and Mori suggested that a stair-rod cross-slip mechanism occurs [79]. In their theory, strong barriers for dislocation motion are created by perfect dislocations gliding on the conjugate slip plane and interacting with groups of dislocation dipoles on the primary slip plane. Accordingly, a sessile Frank dislocation on a (111) plane and a glissile Shockley partial dislocation on the primary slip plane are produced. The cross slip with the stair-rod dislocation are expressed by the following equations:

$$\frac{a}{2} [\bar{1}01] \rightarrow \frac{a}{6} [\bar{2}11] + \frac{a}{2} [\bar{1}\bar{1}2] \rightarrow \quad (9)$$

$$\rightarrow \frac{a}{6} [\bar{1}21] + \frac{a}{6} [\bar{1}\bar{1}0] + \frac{a}{2} [\bar{1}\bar{1}2] \rightarrow \quad (10)$$

$$\rightarrow \frac{a}{6} [\bar{1}21] + \frac{a}{3} [\bar{1}\bar{1}1] \quad (11)$$

$$\frac{a}{6} [\bar{2}11] + \frac{a}{6} [\bar{1}2\bar{1}] \rightarrow \frac{a}{6} [\bar{1}\bar{1}0] \quad (12)$$

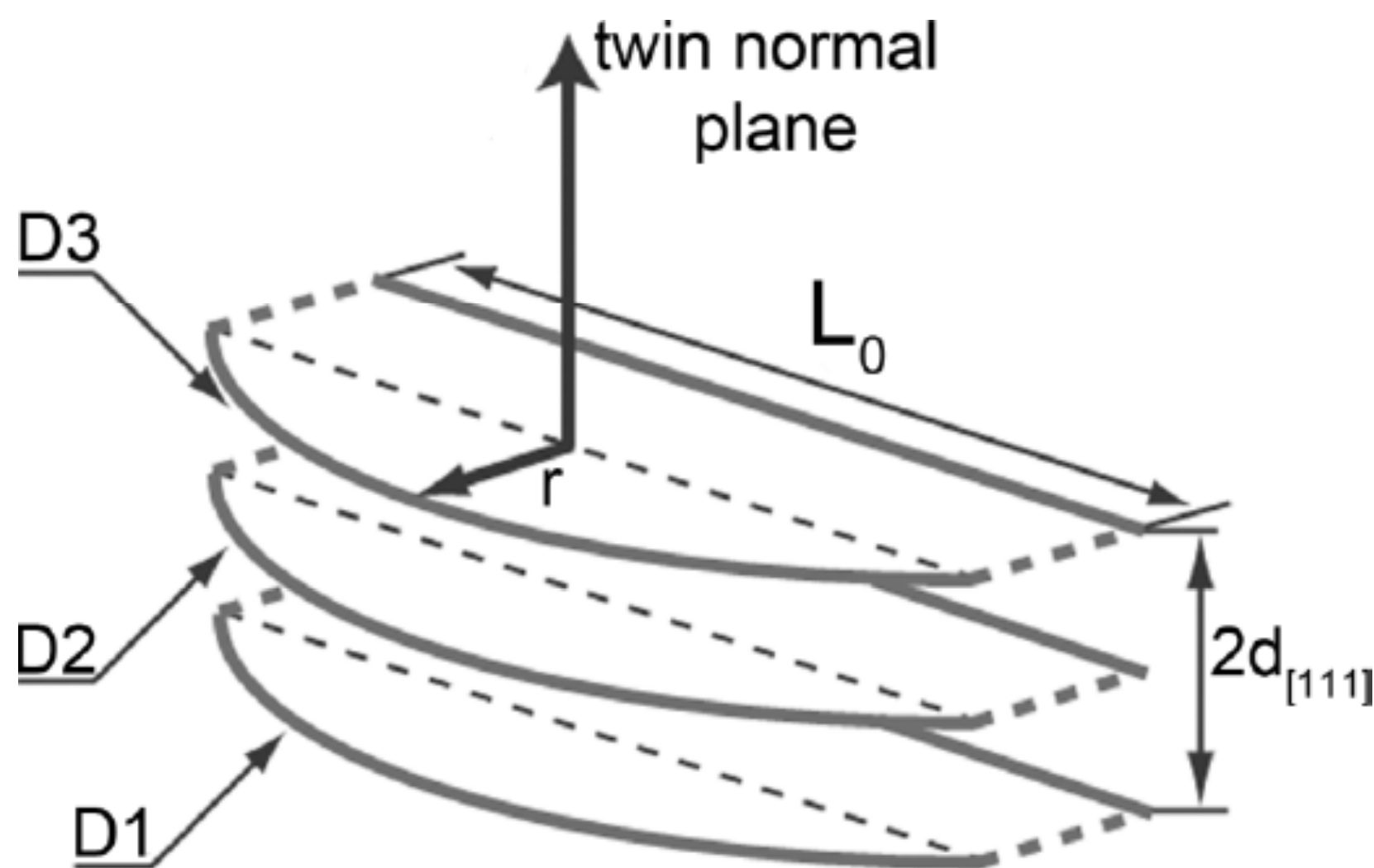


Fig. 17. The twin nucleus proposed by Mahajan and Chin. $d_{\langle 111 \rangle}$ is the interplanar spacing in the $\langle 111 \rangle$ direction, L_0 is the length of the sessile partial dislocations forming the twin nucleus and r is the distance the mobile partial dislocations have bowed out. D1, D2, and D3 are the mobile Shockley partial dislocations which bow out to form the twin.

When an extended primary dislocation expressed by Eq. (9) moves to an obstacle such as a dislocation bundle or multipole, the leading Shockley of $1/6[\bar{2}11]$ can split into the partial of $1/6[\bar{1}21]$ and the stair-rod of $1/6[\bar{1}10]$ according to Eq. (10). The partial of $1/6[\bar{1}21]$ corresponds to the twinning partial. Therefore, the twinning partials can be sufficiently generated for the twin growth from many of the active primary dislocations nearby. In this way, the overlapping wide faults become thick to microtwins.

5) Mahajan and Chin [80] proposed a twin formation model in which a three-layer twin may nucleate when two co-planar $1/2[110]$ dislocations of different Burgers vectors interact with each other by Eq. (13):

$$\frac{a}{2}[\bar{1}01]_{(111)} + \frac{a}{2}[\bar{1}10]_{(111)} \rightarrow 3 \times \frac{a}{6}[\bar{2}11]_{(111)}. \quad (13)$$

Therefore, a macroscopic twin may evolve when three-layer twins distributed at different levels within a localized region grow into each other. A schematic of the twin nucleus is shown in Fig. 17. Twin formation according to this model was proved by direct TEM observations [81] by Bracke et al.

6) Recent investigations by Idrissi et al. and Steinmetz et al. [82-84] revealed a more complex mechanism of twin formation operating in TWIP steels. It was shown [82] that the pole mechanism with deviation [78] or the MTN model [79] can be responsible for the twin formation in Fe-20% Mn-1.2% C TWIP steel, while the twin growth is probably controlled by secondary polar sources created by the interaction of perfect dislocations with the Shockley twinning partials. The other mechanisms

proposed in the literature could not be confirmed thanks to the accurate identification of the different dislocations found within or very close to the mechanically induced twin precursors. Steinmetz et al. [84] developed an improved model using the twin nuclei proposed by Mahajan and Chin [80]. It was shown [84] that both a critical amount of dislocation activity and a critical stress must be reached to form twins. Elevated temperatures clearly delay the onset of twinning by simultaneously decreasing the flow stress, increasing the rate of dislocation annihilation through climb and increasing the SFE, which in turn increases the critical stress needed to initiate deformation twinning. Additionally, it has been noted that SFE determines the activation stress for twin nucleation (14):

$$\tau_c = \frac{\gamma_{SF}}{3b_s} + \frac{3Gb_s}{L_0}, \quad (14)$$

where γ_{SF} is SFE, b_s is the Burgers vector of the Shockley partial, G is the shear modulus and L_0 is the length of the sessile partial dislocations forming the twin nucleus. A very good agreement with experimental compression data for Fe-22Mn-0.6C TWIP steel was found between 293 and 873K using a single set of physically motivated parameters [84].

Mechanical twinning in TWIP steels results in the subdivision of austenite grains to crystallites delineated by twin boundaries as in Hadfield steel (Fig. 18). Dislocation mean free path is thereby reduced, resulting in structural strengthening. The dynamical Hall-Petch effect takes place in TWIP steels [48,55,85] as in Hadfield steel. However, in contrast with Hadfield steel, the TWIP wrought steels exhibit a work hardening rate two-folds higher. This exceptional work-hardening until fracture cannot be explained only by the dynamical Hall-Petch effect. Theoretical calculations show that deformation twinning is not a major contributor to the strengthening of TWIP steels under deformation [29]. The main role the extraordinary strain-hardening of TWIP steels plays is in the substantial dislocation density increase to extremely high values above 10^{15} m^{-2} [29] due to dislocation glide within crystallites surrounded by twin boundaries with a size ranging from 20 to 40 nm. This allows increasing dislocation density to values approximately 10 times higher than those in Al-Mg alloys [86,87], in which no mechanical twinning occurs due to high SFE values. Accordingly, plasticity and the deep drawing ability of TWIP steel are superior and highly exceed similar characteristics of non-age-hardenable Al-Mg alloys [88]. Thus, the high ductility of TWIP steels is

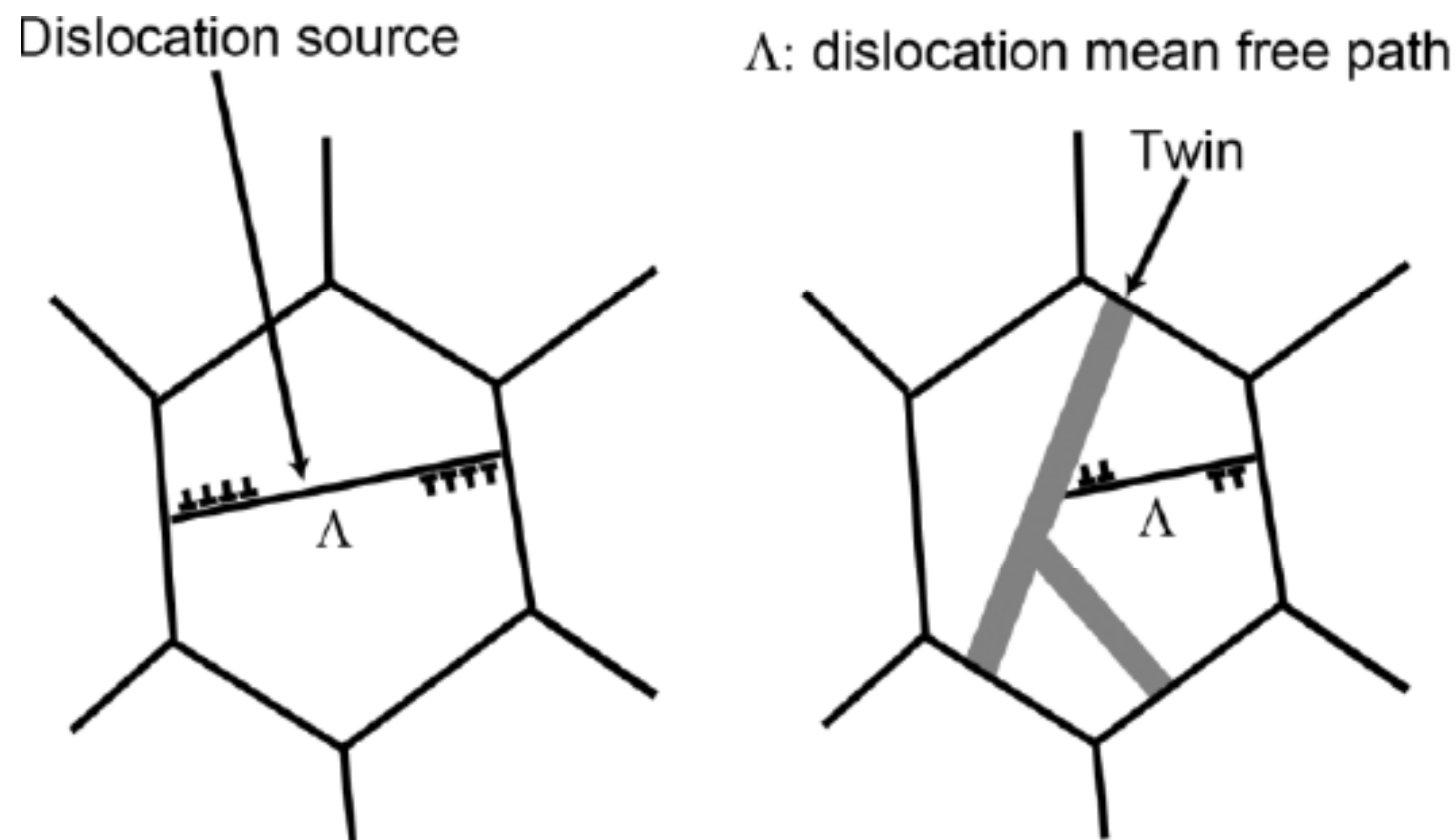


Fig. 18. Schematic presentation of the dynamical Hall-Petch effect.

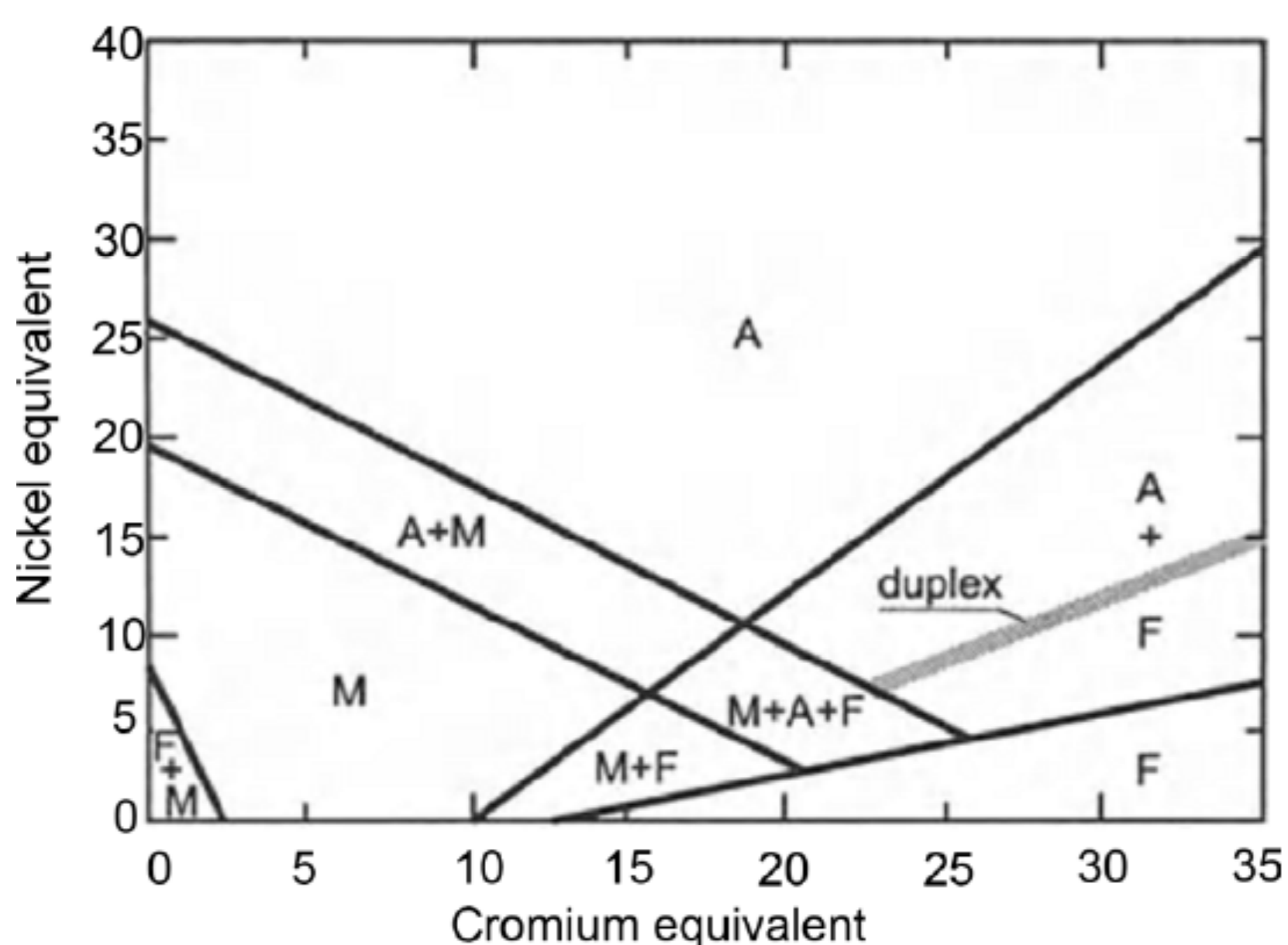


Fig. 19. Schaeffler diagram, revised after Speidel and Uggowitzer (1993). A – austenite, M – martensite, F – ferrite.

attributed to the fact that the critical dislocation density for the failure of the samples occurring suddenly before the work hardening capacity of the material is exhausted [36] is ten-folds higher than for other materials (in which no subdivision of the initial coarse grains to nanoscale areas with boundaries that are non-transparent for gliding dislocation takes place). This subdivision in TWIP steels allows significantly lower critical mean slip distances for the onset of failure. We may assume that the difference in work hardening behavior between Hadfield steel and wrought TWIP steels is mainly attributed to difference in carbon content. In TWIP steels, the average distance of the interstitial atoms near the glide plane is two times lower than in Hadfield steel, and this distance has no remarkable effect on the critical mean slip distance.

Generally, at a given temperature, the SFE value is controlled by chemical composition. The influence of chemical composition on stacking fault energy, microstructure and mechanical behavior of high-Mn TWIP steels is described below in detail.

7. INFLUENCE OF CHEMICAL COMPOSITION ON MICROSTRUCTURE AND MECHANICAL BEHAVIOR OF TWIP STEELS

Chemical composition strongly affects SFE, microstructure and mechanical properties of high-Mn TWIP steels in a similar manner as it does the other austenitic steels [14]. As it was demonstrated, the TWIP steels retain a fully austenitic structure up to high strains, and no strain-induced martensitic transformation occurs at room temperature. Accordingly, the first requirement of the chemical composition of TWIP steels is to retain a fully austenitic microstructure after normalization at 1050 °C. This can be accurately predicted using the Schaeffler diagram [14] (Fig. 19). The influence of chemical composition on the phase composition is determined by the contents of α - and γ -stabilizers denoted as Cr_e (chromium equivalent) and Ni_e (nickel equivalent), respectively. Cr_e and Ni_e for interstitial and substitutional elements present in TWIP steels are as follows:

$$Cr_e = 5.5 \times Al + 2 \times Si, \quad (15)$$

$$Ni_e = 30 \times C + 25 \times N + 0.5 \times Mn. \quad (16)$$

Currently, an optimal chemical composition of TWIP steels varies in the following range: (0.3÷0.7)% C- (18÷33)% Mn-(0.8÷2)% Al-(1÷2)% Si and Fe balance [37,38]. The Fe-0.6% C-18% Mn TWIP steel contains minimal amounts of alloying elements providing the TWIP-effect. All other TWIP steels contain a higher amount of alloying elements, except C, which can be reduced to 0.3% [38]. Therefore, TWIP-steels, according to the Schaeffler diagram,

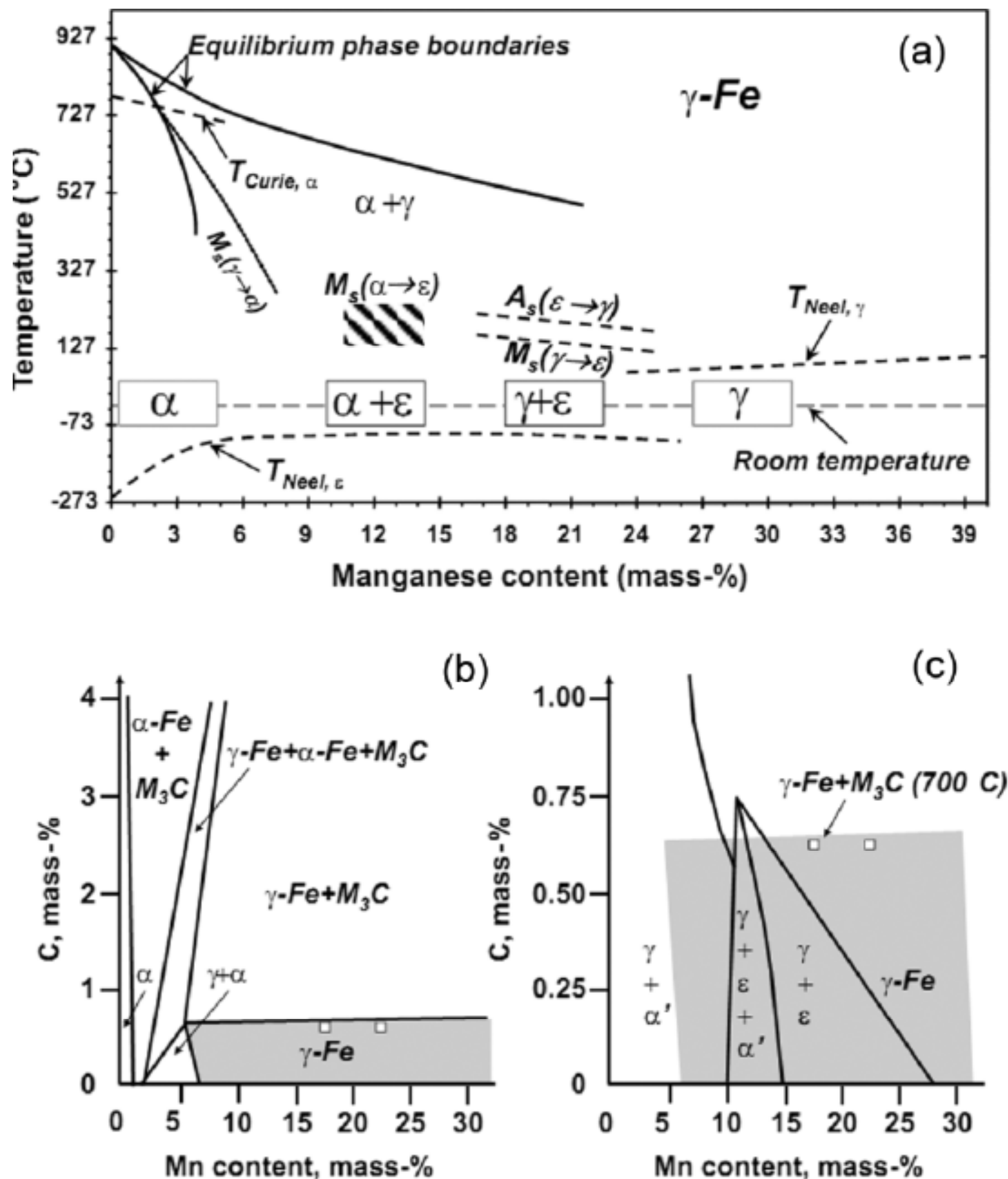


Fig. 20. (a) Metastable Fe-Mn phase diagram, (b) Fe-rich corner of Fe-Mn-C equilibrium diagram at 700 °C showing the austenite stability range in grey, (c) superposition of the 700 °C austenite stability range and the microstructure observed after quenching to room temperature from 950 °C.

are fully austenitic at room temperature. However, this austenite is metastable. According to the thermodynamic calculations, the $\gamma \rightarrow \alpha$ (A_{C3}) transformation temperature for the TWIP steels varies from 550 °C to 580 °C. Most TWIP steels have a fraction of austenite stable at room temperature ranging from 30% to 50%. Accordingly, it is necessary to determine the content of alloying elements that will ensure the suppression of strain-induced martensite transformation at room temperature.

For this purpose, the metastable Fe-Mn constitution diagram was calculated [89] (Fig. 20a). At room temperature and with Mn content ranging from 5 to 25%, the multiphase structure consists of a major portion of α' -martensite predominance, which tends to be substituted by ϵ -martensite with Mn

enrichment and a minor portion of austenite. Both types of martensite may have stress-assisted or strain-induced origins. At 27%wt.Mn, martensitic transformation is completely suppressed. This suppression takes place at lower Mn contents with increasing carbon [90]. At 0.6% C and 18% Mn, no strain-induced martensite transformation occurs, and a fully austenitic carbide-free microstructure exists. Increasing the carbon content beyond 0.6 mass.% may cause the precipitation of cementite at boundaries and within grain interiors, as in Hadfield steel [3-7] (Figs. 20b and 20c).

Microstructural characterization after tensile tests of TWIP steels with chemical and phase compositions listed in Table 2 showed that increasing the Mn content suppresses the $\gamma \rightarrow \alpha'$ transforma-

Table 2. Chemical analyses and the constituent phases before and after tensile testing at 10^{-4} s^{-1} at room temperature.

Steel	Chemical composition, mass. %					Phases before tensile test	Phases after tensile test
	Mn	Si	Al	C	Fe		
Fe-15Mn-4Si-2Al	16.2	4.0	1.8	0.02	Bal.	$\gamma + \alpha + \varepsilon$	$\gamma + \alpha' + \varepsilon + \alpha$
Fe-15Mn-3Si-3Al	17.9	3.2	2.9	0.02	Bal.	$\gamma + \alpha$	$\gamma + \alpha' + \alpha$
Fe-15Mn-2Si-4Al	15.9	1.9	3.5	0.01	Bal.	$\gamma + \alpha$	$\gamma + \alpha' + \alpha$
Fe-20Mn-4Si-2Al	18.2	4.3	1.8	0.06	Bal.	$\gamma + \alpha$	$\gamma + \alpha' + \varepsilon$
Fe-20Mn-3Si-3Al	20.1	2.8	2.9	0.04	Bal.	$\gamma + \varepsilon$	$\gamma + \alpha' + \varepsilon$
Fe-20Mn-2Si-4Al	18.1	1.8	3.5	0.03	Bal.	$\gamma + \alpha$	$\gamma + \alpha + \alpha'$
Fe-25Mn-4Si-2Al	25.5	3.9	1.8	0.03	Bal.	$\gamma + \varepsilon$	$\gamma + \varepsilon$
Fe-25Mn-3Si-3Al	26.6	3.0	2.8	0.03	Bal.	γ	γ
Fe-25Mn-2Si-4Al	25.6	2.0	3.8	0.03	Bal.	γ	γ
Fe-30Mn-4Si-2Al	28.7	4.0	2.0	0.02	Bal.	$\gamma + \varepsilon$	$\gamma + \varepsilon$
Fe-30Mn-3Si-3Al	29.2	3.0	2.8	0.02	Bal.	$\gamma + \varepsilon$	γ
Fe-30Mn-2Si-4Al	30.6	2.0	3.9	0.01	Bal.	γ	γ

tion [91,92]. Increasing the Si content and decreasing the Al content promotes the formation of α -martensite. Multiphase steels with $\gamma + \varepsilon$, $\gamma + \alpha'$ or $\gamma + \varepsilon + \alpha'$ phase compositions exhibit $\gamma \rightarrow \alpha'$ or $\gamma \rightarrow \varepsilon$ martensite transformations under tension. X-ray diffraction analysis revealed that neither α' - or ε -martensite form after the tension of the steels with 25 and 30% Mn and a large amount of deformation twins appear. However, some ε -martensite plates were detected within separate γ grains of Fe-25% Mn-3%Si-3% Al steel.

The strength of TWIP steels can only be increased by solid solution hardening, as the presence of carbides is undesirable. The dependence of the YS and UTS values on the contents of alloying elements in TWIP steels and the grain size can be described by the standard equations for austenitic steels [14]:

$$\text{YS} = 63.5 + 356.5 \times \text{C} + 496 \times \text{N} + 20.1 \times \text{Si} + 12.7 \times \text{Al} + 7.1 \times d^{-1/2}, \quad (17)$$

$$\text{UTS} = 449.5 + 852.5 \times \text{N} + 542.5 \times \text{C} + 37.2 \times \text{Si} + 18.6 \times \text{Al} + 7.1 \times t^{-1/2}, \quad (18)$$

where d and t are grain size and twin thickness, respectively. It is observed that carbon and nitrogen play the role of the most effective agents for solid solution hardening; YS and UTS are linearly dependent on the contents of these interstitial elements. Substitutional Mn elements have almost no influence on the strength of TWIP steels. However, this does not apply for DSA-strengthening. Bouaziz et al. [93] calculated the Mn and C contents influence on YS as:

$$\text{YS} = 228 + 187 \text{C} - \text{Mn}, \quad (19)$$

which differs from Eq. (17) by an increased value of $\sigma_0 = 228 \text{ MPa}$ and a decreased increment of YS associated with C content; in addition, no effect of grain size on YS was taken into account. A negative effect of increased Mn content on YS was confirmed by [93] for Fe-(0-1.2)% C-(12-30)% Mn steels.

Experimental studies dealing with the effect of Al additions on the strength characteristics of TWIP steels also revealed the invalidity of the equations (17-18) [94,95]. Al addition reduces strength because Al not only contributes to the solid solution hardening but also increases the SFE (Fig. 14b). Thereby, Al additions hinders mechanical twinning in the Fe-22% Mn-0.6% C steel; the onset of twinning is shifted to higher strains. Fig. 21 shows the difference in the microstructure of steels with different Al contents at nearly the same strains. The onset of twinning was observed in Al free steel at low strains, whereas in the steels with 3% Al and 6% Al, the onset of mechanical twinning was found at strains beyond 20%. The authors explain this phenomenon by the fact that the critical stress for twinning increases with SFE. Al additives hinder the aforementioned short-range order attributed to the formation of Mn-C dipoles that in turn reduces the critical stress required for the onset of twinning.

The influences of Mn, Al and Si on the tensile mechanical properties of TWIP steels are shown in Figs. 9 and 22. Increasing the Mn content reduces the UTS values from $930 \pm 160 \text{ MPa}$ to $630 \pm 100 \text{ MPa}$ and increases elongation-to-failure from $44 \pm 5\%$ to $82 \pm 13\%$ (Fig. 22b). At $\text{Mn} \geq 25 \text{ wt.}\%$, no effect of

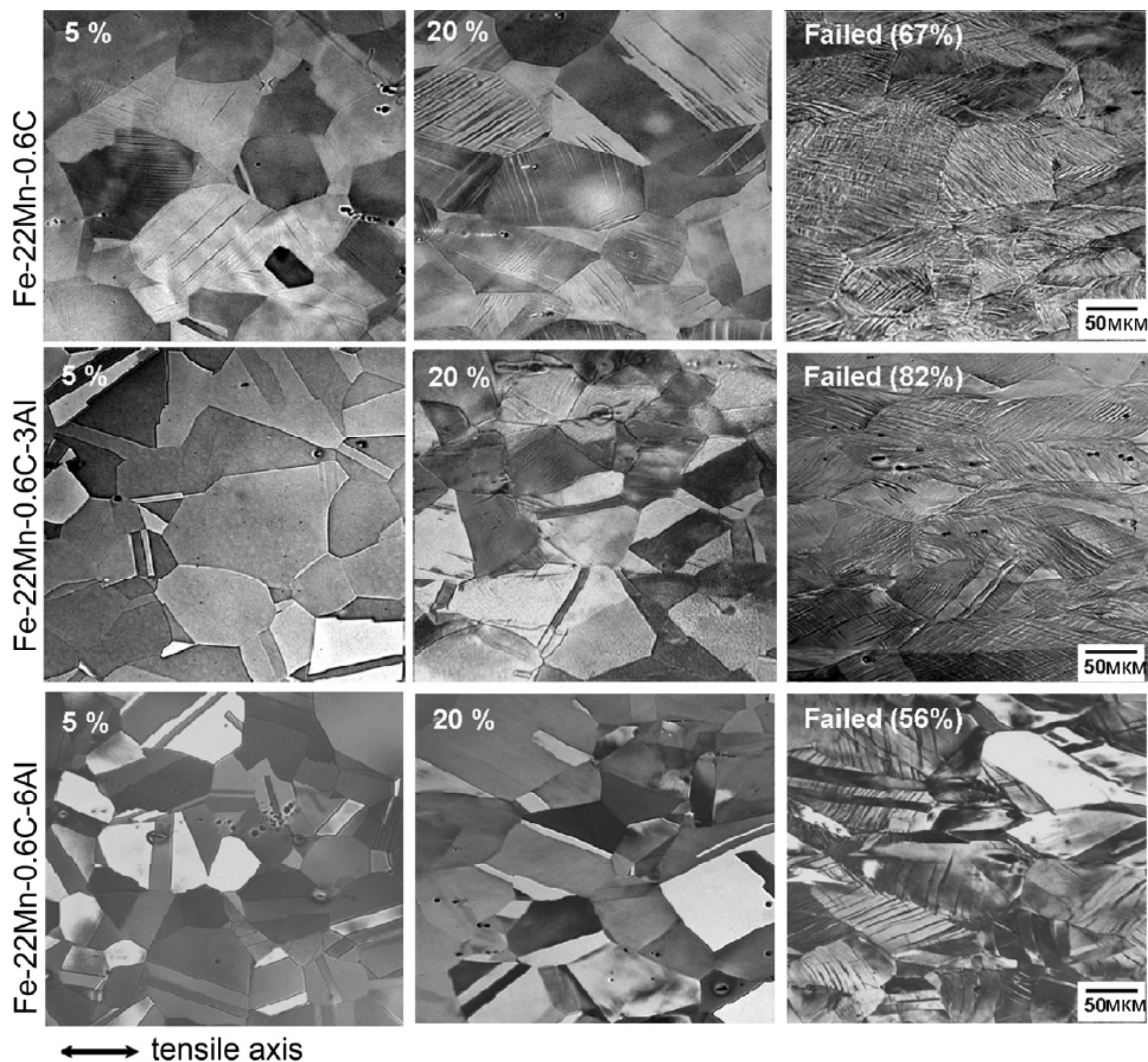


Fig. 21. Optical micrographs of the Fe-22%Mn-0.6%C-(0-6)%Al steels after different tensile strains.

Mn on ductility was found. UTS decreases with decreasing Si content. Increasing the Al content to 3 wt.% leads to decreased UTS, while further increase of Al to 6wt.% increases UTS. Steels with 3% Si and 3% Al show the highest elongation-to-failure. This conclusion is also supported by the work [95] in which the Fe-22% Mn-0.6% C TWIP steels with Al contents ranging from 0% to 6% were examined (Table 3).

The PLC effect is known to result in a reduction in ductility and the formation of deformation bands that leave undesirable traces on the surface of the sheet product [96]. Therefore, it is reasonable to develop an optimal chemical composition of TWIP steel providing no or diminished plastic instability. An Al free Fe-22% Mn-0.6% C steel exhibits plastic

flow instabilities at high strains, while no evidence for PLC was found for the same steel containing 3 and 6% Al. The higher YS value of the 6% Al steel can be explained by finer grain size: ($36 \pm 23 \mu\text{m}$ compared to $44 \pm 28 \mu\text{m}$ for 0% Al and 3% Al). Therefore, Al can be considered as effective agent suppressing plastic instability associated with DSA in TWIP steels.

There is a strong relationship between manifestation of DSA in TWIP steels and other alloying additions. DSA is observed in high Mn twinning-induced plasticity steels containing interstitial C solutes in a restricted range of temperatures around room temperature. At room temperature and at quasi-static strain rates, the tensile curve of a Fe-18Mn-0.6C-(0-1.5)Al steels exhibits typical serra-

Table 3. Mechanical properties of the Fe-22%Mn-0.6%C-(0-6)%Al steels after tensile tests at room temperature.

Steel	YS, MPa	UTS, MPa	Uniform elongation, %	Total elongation, %
Fe-22Mn-0.6C	290	875	62	65
Fe-22Mn-0.6C-3Al	277	672	75	80
Fe-22Mn-0.6C-6Al	317	692	46	54

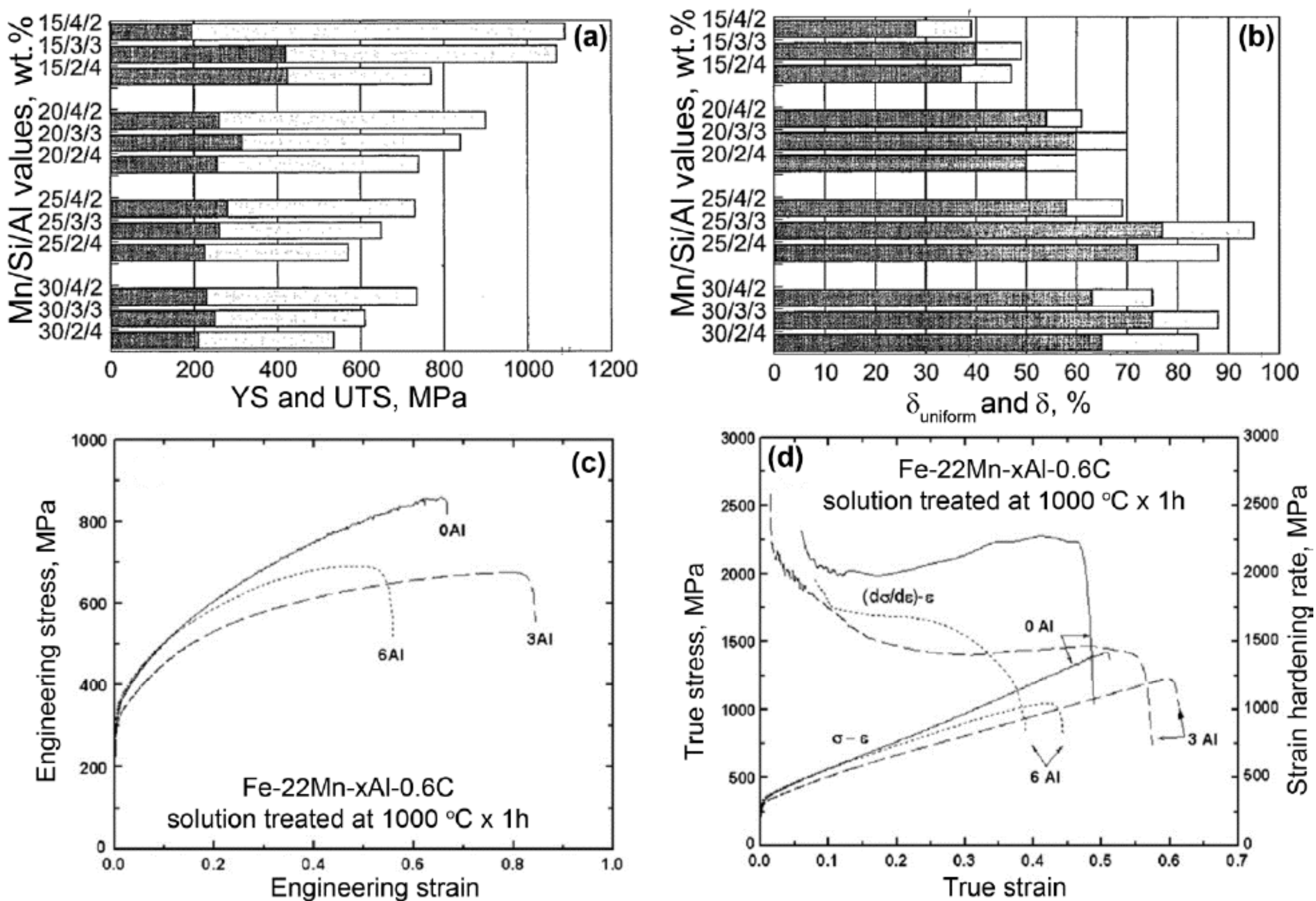


Fig. 22. Mechanical properties of TWIP steels with different Mn, Al and Si content: (a) YS (grey) and UTS (white); (b) uniform elongation (grey) and total elongation (white). (c) engineering stress-strain curves and (d) true stress-true strain curves and effect of strain on strain-hardening rate for Fe-22Mn-0.6C-(0-6)Al steels.

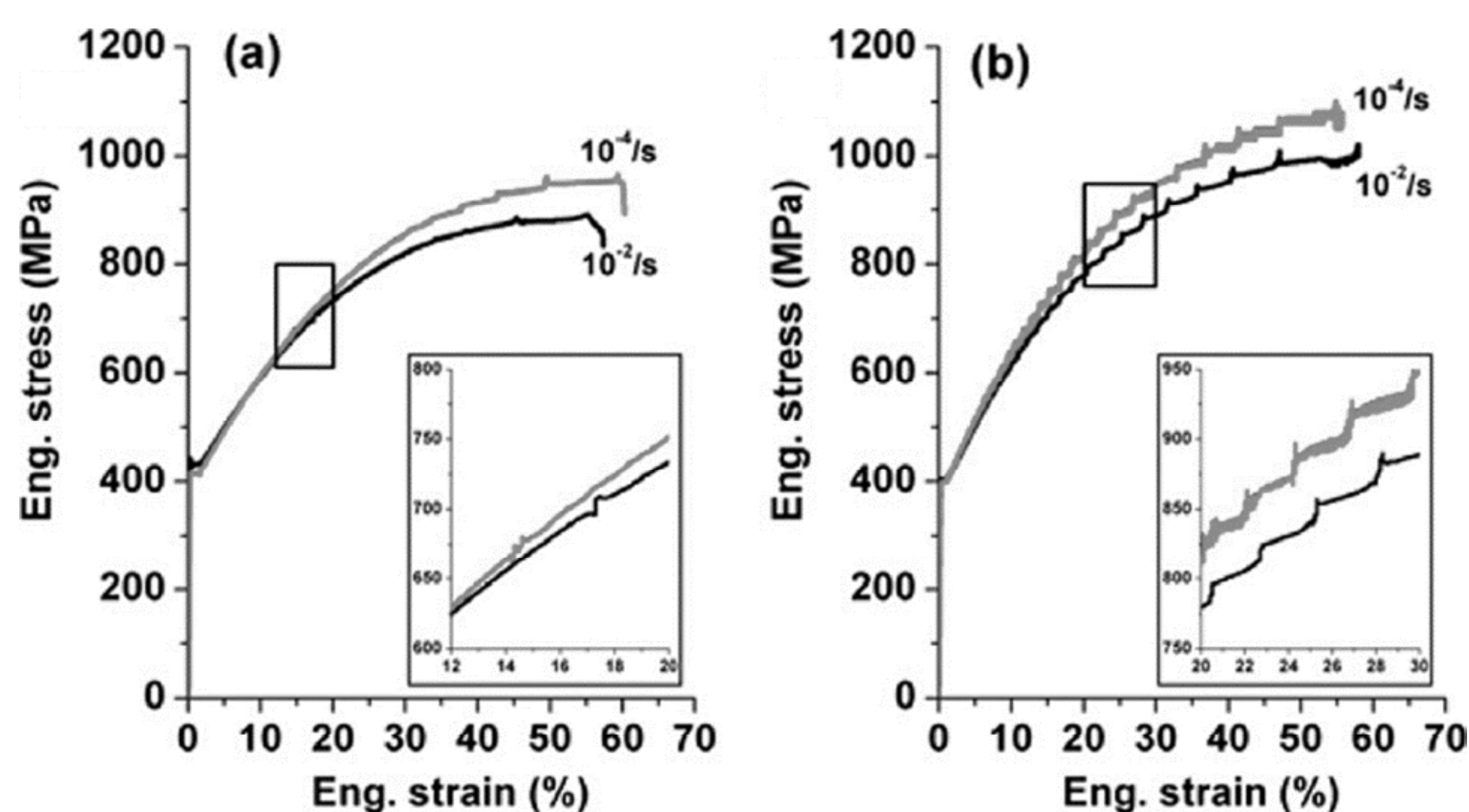


Fig. 23. Engineering stress-strain curves for the (a) Fe-18Mn-0.6C-1.5Al steel and (b) Fe-Mn-C steel recorded for strain rates of 10^{-4} s $^{-1}$ and 10^{-2} s $^{-1}$. Step-like type A serrations are only observed for the FeMnC TWIP steel.

tions (Fig. 23). The occurrence of this “jerky flow” in austenitic high Mn steels is well known [97-101] and has been described in terms of the PLC effect. Most of the experimental studies report a so-called A type PLC, which is characterized by the occurrence of narrow and mobile deformation bands that explain the successive plateaus in between regular stress jumps on the tensile curves. The occurrence

of static B or random C type PLC bands has been rarely reported in the literature, except at high temperatures [41]. Therefore, decreasing the C content from ≥ 1 wt.% in Hadfield to 0.3-0.6 wt.% in automotive TWIP steels modified the manifestation of PLC through transition from B type oscillation to A type.

According to Rose and Glover [102], the presence of interstitial C is essential to induce DSA in

austenitic steels due to the reorientation of C-vacancy complexes by internal elastic stress fields originating from lattice dislocations. Chen [99] reported that DSA occurs when an aging process, related to solute atoms, is fast enough to occur during deformation, i.e., when the dislocation velocity is similar to the solute mobility. Dastur et al. [4] suggested that C–Mn pairs or point defect clusters reorienting themselves in the stress field at the core of the dislocations are able to pin gliding dislocation strongly. The C–Mn octahedral clusters can more effectively pin gliding dislocations rather than C–Mn pairs. Therefore, short range ordering (SRO) causes dislocation pinning. In these clusters, carbon occupies the octahedral interstitial sites, and manganese atoms occupy the six nearest neighbor sites with an occupancy higher than the expected value based on the atomic concentration of manganese. Saeed-Akbari et al. [71] discuss the PLC phenomenon in TWIP steels in detail. They assume the most stable SRO zone is CMn_6 octahedral clusters and that the strain-hardening behavior could be described by introducing a semi-empirical dimensionless parameter called TOI (theoretical ordering index) defined as:

$$TOI = \frac{N_C}{N_{Mn}}, \quad (20)$$

where N_C and N_{Mn} are the number of atoms or the contents of C and Mn in at.%, respectively. TOI provides a ratio between portions of carbon and manganese atoms in different Fe-Mn-C steels. It was shown that for TOI values ranging from 0.1 to 0.3, an increase in TOI leads to increased density of CMn_6 octahedral clusters. At $TOI \geq 0.3$, the density of CMn_6 octahedral clusters is likely to decrease with increasing TOI due to the reduction of the number of manganese atoms available for the formation of the clusters. Finally, both the shortage of carbon in the TOI range below 0.1 and the shortage of manganese in the TOI range above 0.3 could decrease the strengthening attributed to DSA and, therefore, the plastic instability associated with the interaction of dislocations with SRO areas. For TWIP steels, this approach is most attractive for $TOI \leq 0.1$ provided by $\%wt.C/\%wt.Mn=0.022$. For instance, Al free TWIP steels exhibited no PLC effect or insignificant plastic instability must have the following chemical compositions: Fe-0.4C-18Mn, Fe-0.5C-22Mn, Fe-0.6C-28Mn.

As mentioned above, the strain localization and serrated flow are highly undesirable for industrial deep drawing applications because deformation

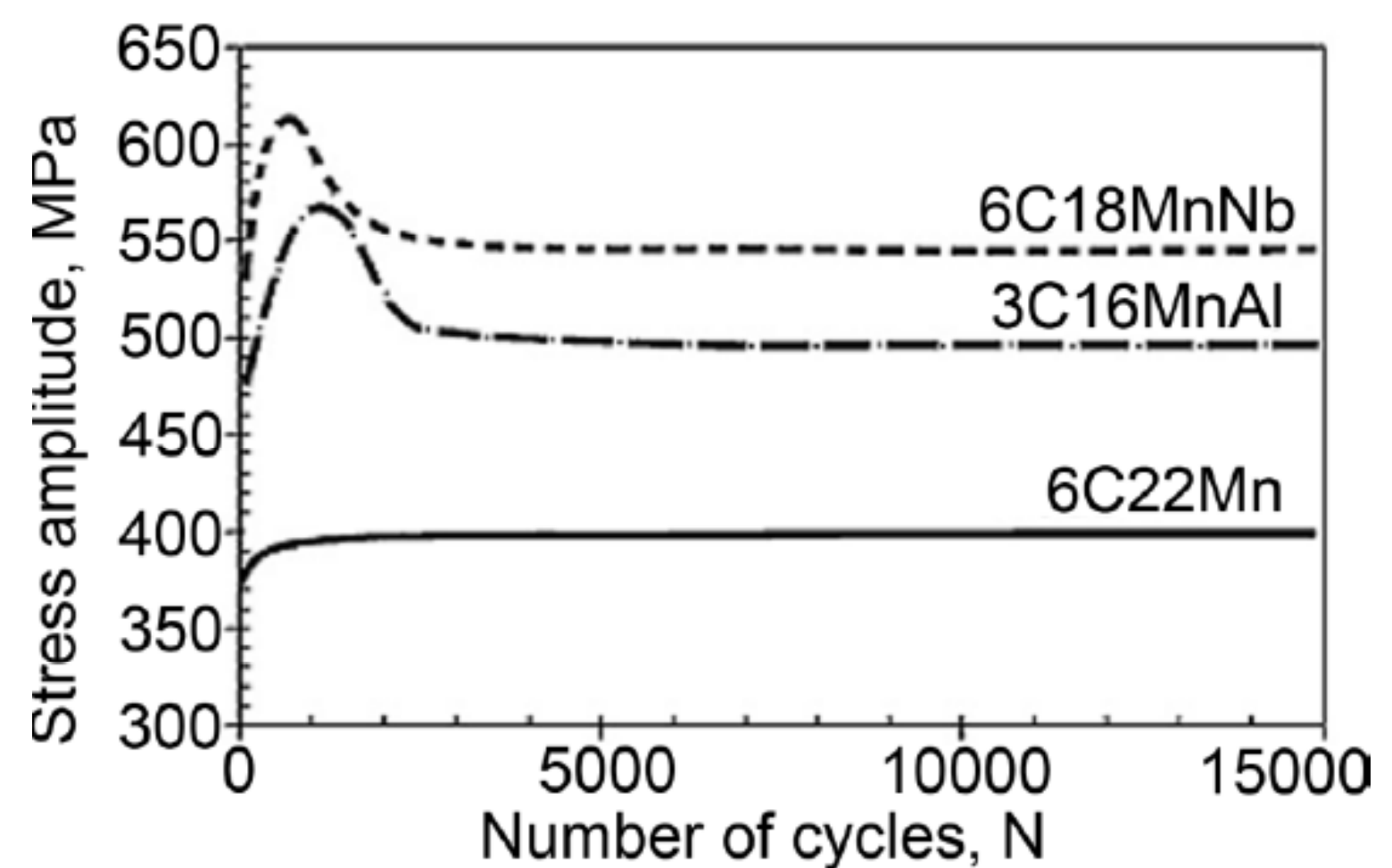


Fig. 24. LCF behavior of three TWIP steels.

bands could lead to unexpected fracture. However, most works on bi-axial loading of TWIP steels demonstrate no serrated flow and no undesirable traces on the surface of the sheet articles [31,103].

8. FATIGUE BEHAVIOR OF TWIP STEELS

The fatigue properties of high Mn TWIP steels are important for the commercial use of these materials in the automotive industry and for other applications. However, there is a limited number of works on the fatigue behavior of these steels. Hamada et al. [104-106] studied the cyclic behavior of TWIP steels under bending conditions and considered the effect of grain size on low-cyclic fatigue (LCF) (Fig. 24). Fe-22% Mn-0.6% C (denoted as 6C22Mn) exhibit no softening under cyclic loading and Fe-18% Mn-0.6% C-0.02%Nb (denoted as 6C18MnNb) and Fe-16% Mn-0.3% C-1.5% Al (denoted as 6C22Mn) steels showed a hardening peak followed by a short softening stage at small cycle numbers. Fe-22% Mn-0.6% C exhibits superior resistance to LCF compared to the two other steels: for the lowest stress amplitude of 380 MPa leading to the fatigue life longer than 2×10^6 cycles, only a minimal cyclic hardening can be identified leading to the saturation stress amplitude of 400 MPa.

Wu et al. [107] and Rüsing et al. [108] studied the LCF of Fe-23% Mn-0.6% C and Fe-22% Mn-0.6% C-0.3V-0.2Cr-0.25Si TWIP steels, respectively. They confirmed that TWIP steel show cycling hardening and cycling saturation rather than cycling softening until the final fracture with a strain amplitude ranging from $\pm 0.2\%$ to $\pm 0.5\%$. The fatigue life at the cyclic strain amplitude of $\pm 0.4\%$ is more than 3000 cycles, which is 1.5-2 times higher than for DP780, TRIP780 and HSLA800 steels. Therefore, even high low-cycle loading could not provide the softening of TWIP steels that is important for car body structural components.

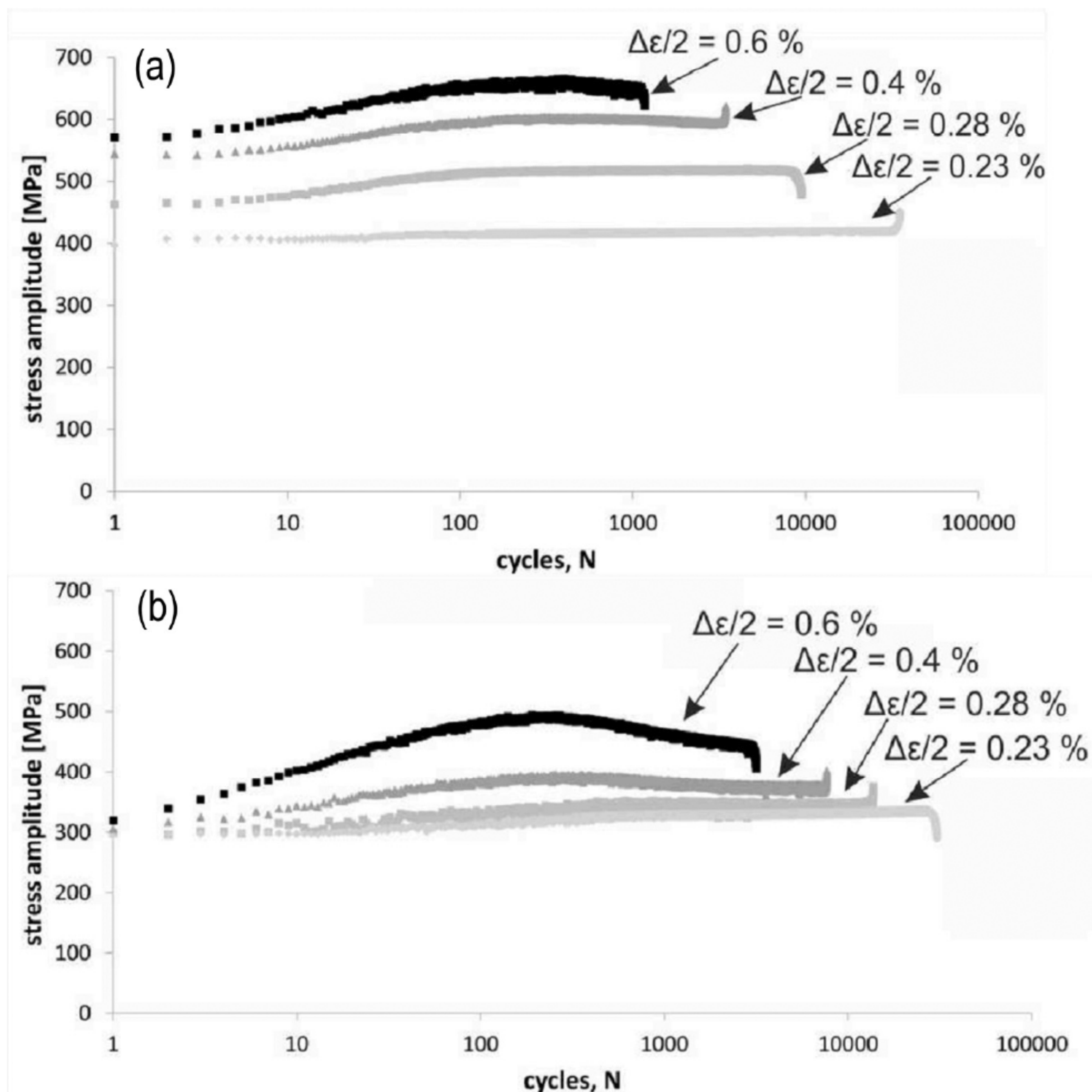


Fig. 25. Cyclic deformation response of the (a) fine- and (b) coarse grained condition, fatigued with constant strain amplitudes at ambient temperature.

In addition, the LCF behavior of the Fe-22% Mn-0.6% C-0.3V-0.2Cr-0.25Si steel was examined in fine-grained and coarse-grained conditions (Fig. 25) [108]. It was found that grain refinement to 2-5 μm provides cyclic hardening at the cyclic strain amplitude of $\pm 0.6\%$, while coarse grained TWIP steel with an average grain size of 80 μm exhibits insignificant softening at a high strain amplitude of $\pm 0.6\%$. However, the amplitude stress remains higher than the stress attributed to steady state cyclic loading. This conclusion is very important because it means that if this regularity is valid, the extensive twinning under deep drawing leading to subdivision of the initial austenite grains to nanoscale crystallites delimited by twin boundaries improves the resistance of TWIP steels to LCF.

The change in low-cycle fatigue properties and deformation microstructure due to the alteration of aluminum and silicon contents was studied by Nikulin et al. in relation to the tensile properties in Fe-30Mn-(6-x)Si-xAl ($x=0, 1, 2, 3, 4, 5, 6$ wt.%) steels that exhibited strain-induced martensitic transformation at low strains for the range of very

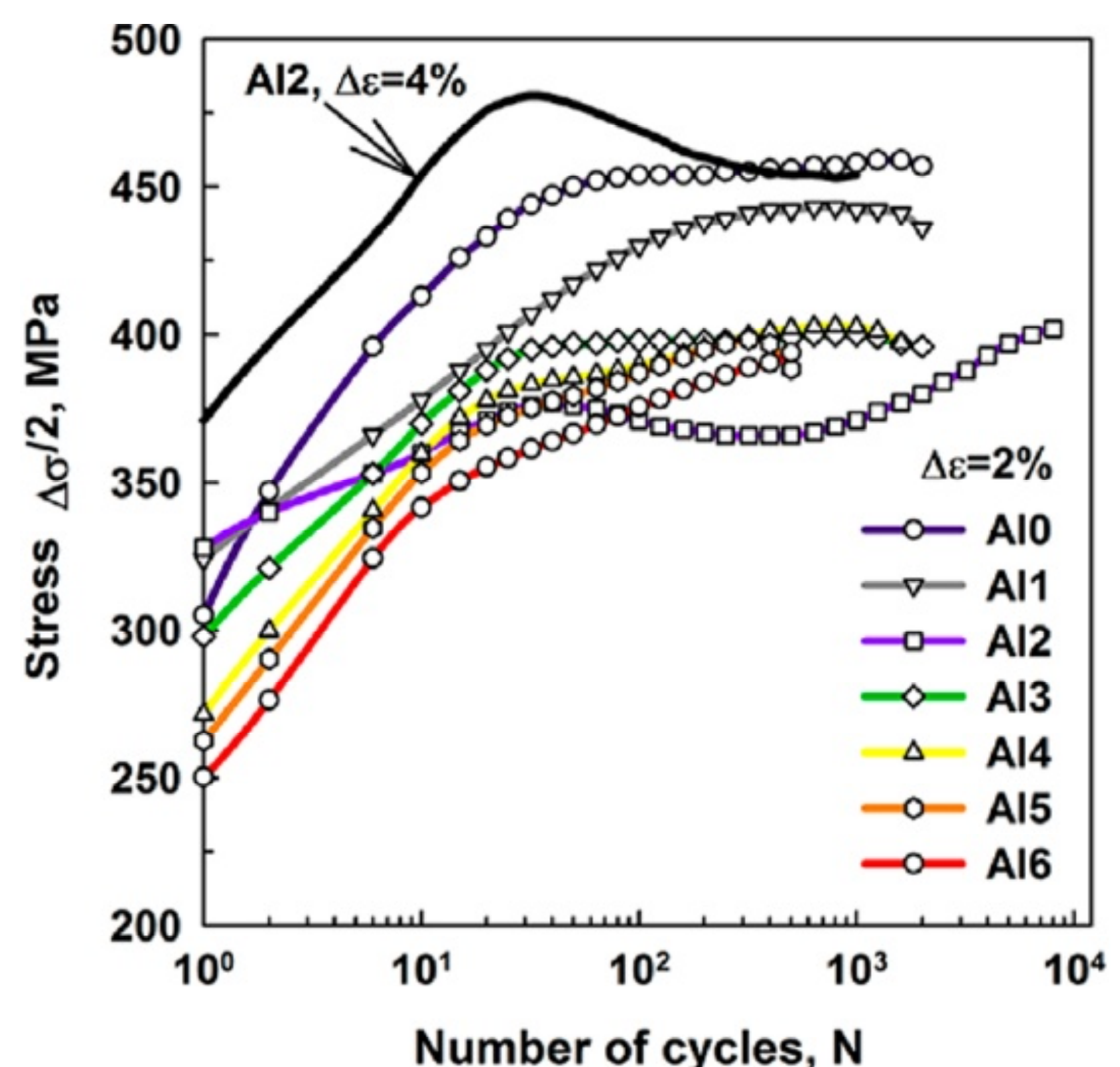


Fig. 26. Changes in stress amplitude with increasing number of cycles during the LCF test at $\Delta\varepsilon = 2\%$ for Fe-30Mn-(6-x)Si-xAl steels.

high amplitudes (Fig. 26) [109]. These steels were aimed to serve as dampers in buildings to adsorb earthquake energy. It should be noted that the mar-

Table 4. Chemical composition (wt.%) and mechanical properties of the steels in [105].

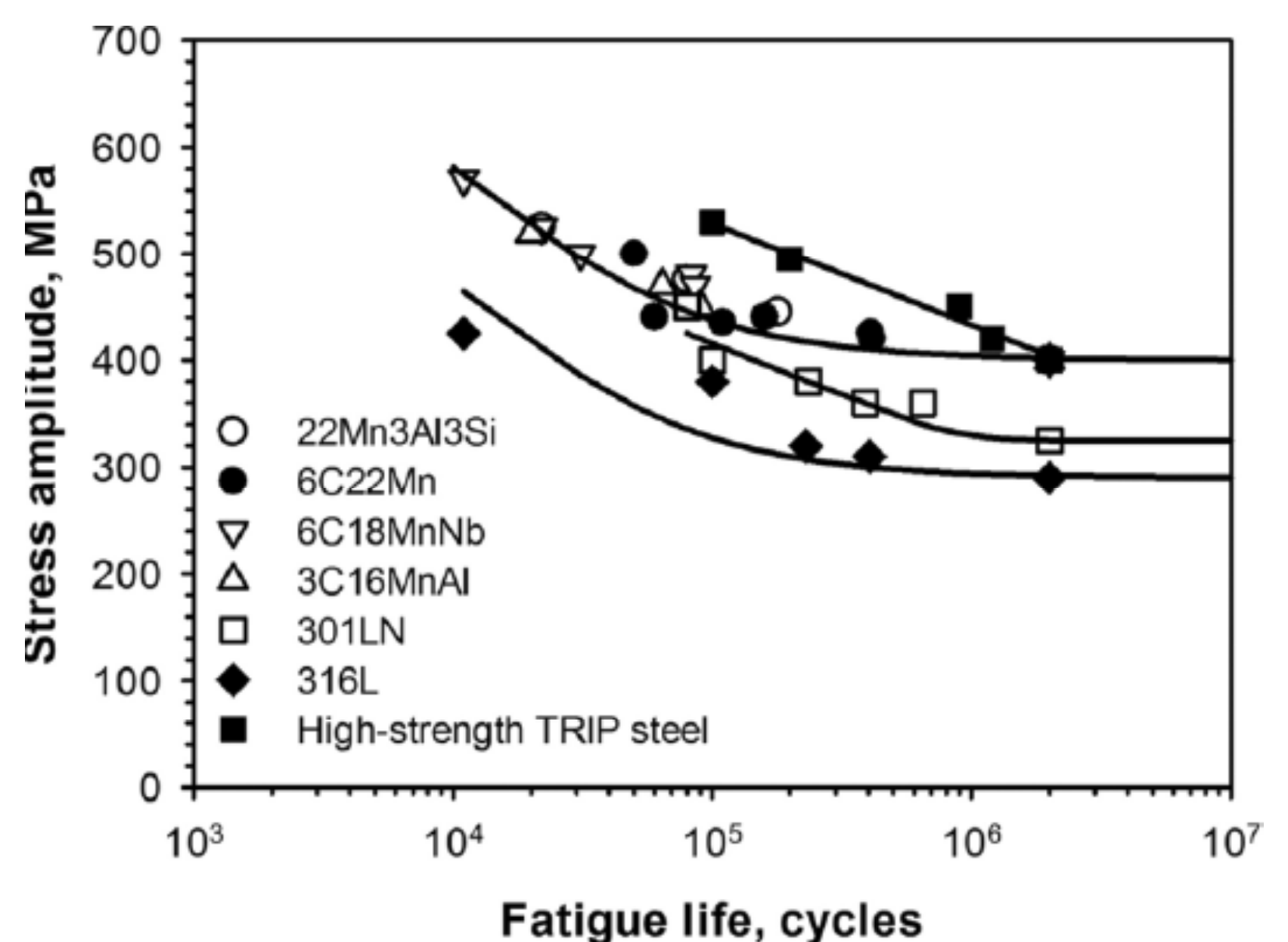
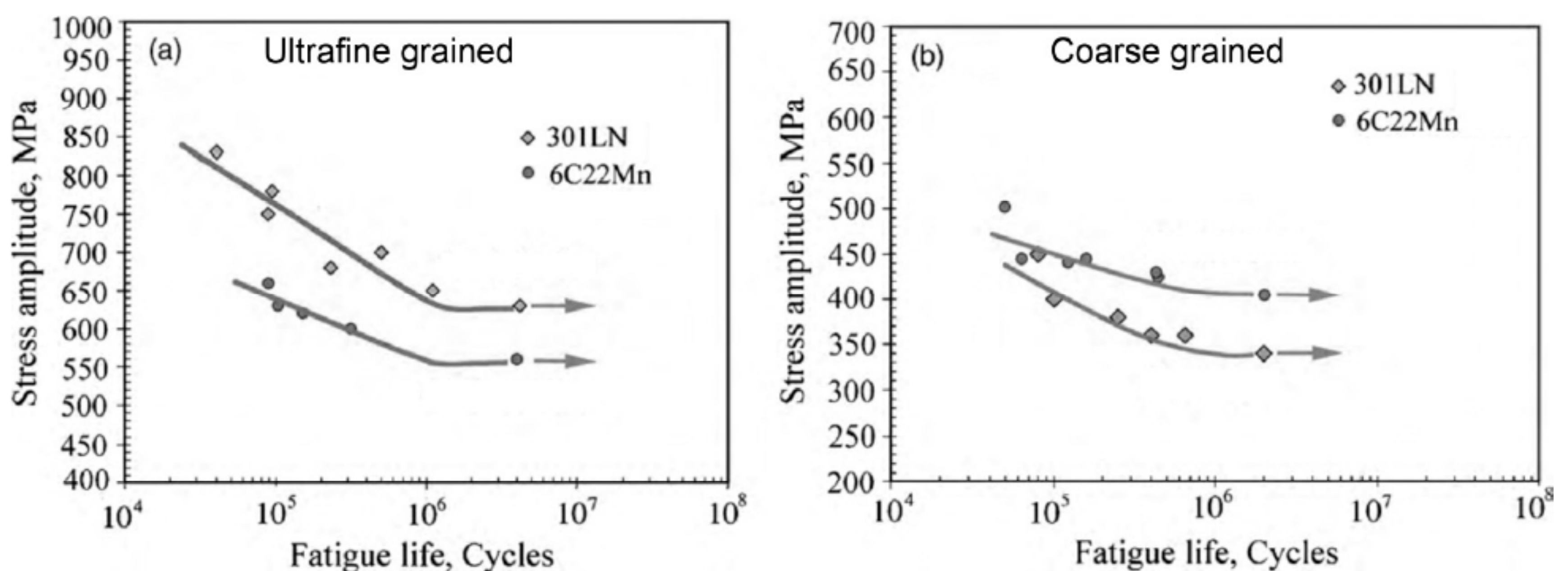
Steel	C	Mn	Al	Si	Nb	Fe	YS, MPa	UTS, MPa	Elongation, %
22Mn3Al3Si	0.01	21.3	3.02	3.00	-	Bal.	353	812	94
6C22Mn	0.6	22.3	-	-	-	Bal.	316	866	96
6C18MnNb	0.6	17.8	-	-	0.02	Bal.	308	963	91
3C16MnAl	0.29	16.4	1.54	-	-	Bal.	268	830	98

tensite fraction decreased with increasing x . It was shown that the ability of TWIP steels to withstand very high cyclic loads tends to slightly decrease with increasing Al content, and, therefore, steels that exhibit TWIP and TRIP effects, concurrently, are more suitable for dampers.

Hamada et al. [104, 105] reported high-cycle fatigue (HCF) behavior of the four TWIP steels listed in Table 4 and Fe-22Mn-0.6C steel [106] with coarse-grained (CG) (32 μm) and ultrafine-grained (UFG) (1.8 μm) structure in comparison with 301LN stainless steel. The fatigue strength for the four TWIP steels is 400 MPa (Fig. 27), which is higher than YS and the fatigue strength of the stainless steel. Therefore, TWIP steels are unique materials that exhibit fatigue strength higher than YS and equal to that of the TRIP780 steel. Therefore, TWIP steels exhibit sufficient resistance to HCF that is close to one of the high-strength automotive steels despite the difference in YS. For 301LN and TWIP steels in coarse-grained and ultrafine-grained conditions, it was reported [106] that the fatigue limit increased by +77% and +40%, respectively, through grain refinement in these steels (Fig. 28). Therefore, grain refinement is an effective method to increase the fatigue strength of TWIP steels, and mechanical

twinning under deep drawing has to enhance HCF resistance.

No mechanical twinning takes place during fatigue in TWIP steels, only the formation of intense slip bands as a result of cyclic stress. This can be explained through the critical dislocation density in addition to the homogeneity of the dislocation slip required for the initiation of deformation twins. This

**Fig. 27.** Bending stress vs cycles to failure curves of the TWIP steels in and of 301LN, 316L, and TRIP steel (data from [105]).**Fig. 28.** Stress amplitude-fatigue life data and plots for 301LN and 6C22Mn steels with (a) UFG structures and (b) CG structures.

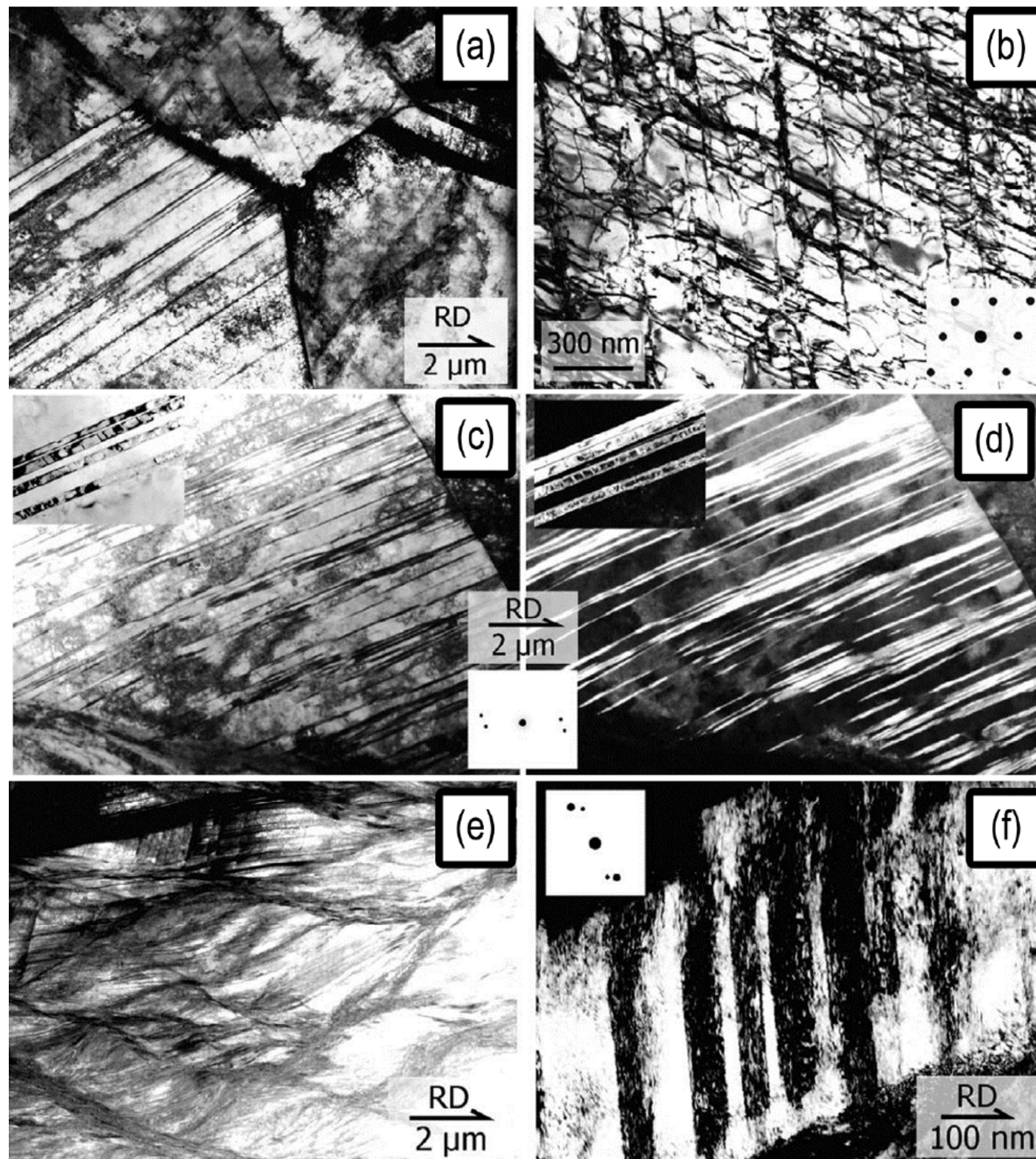


Fig. 29. Microstructure evolution of the Fe-30Mn-3Al-3Si upon cold rolling: (a) $\varepsilon = 0.10$: triple junction; one grain contains deformation twins; (b) $\varepsilon = 0.10$: grains without twins containing a high density of planar dislocation structures; (c) bright- and (d) dark-field TEM images of twins after $\varepsilon = 0.21$, the insets show twins details; (e) S-shaped structure evolved after 1.05 true strain. and (f) lamella structure showing twin orientation. RD – rolling direction.

means that the TWIP effect has no essential role in the cyclic plastic deformation of TWIP steels.

9. EFFECT OF THERMOMECHANICAL PROCESSING ON MICROSTRUCTURE AND MECHANICAL PROPERTIES OF TWIP STEEL

The main disadvantage of TWIP steels that limits their commercial use is the low YS. The easiest way to increase the YS is TMP. TWIP steels were developed for automotive applications, so the most appropriate processing is cold rolling and subsequent recrystallization annealing. Vercaemmen et al. [110] studied the influence of cold rolling on the microstructure of Fe-30Mn-3Al-3Si steel (Fig. 29). At $\varepsilon \sim 0.1$, twins appear in the form of straight lines in more than half of the initial grains (Fig. 29a). Generally, only one twinning system operates in each grain: the twinning system having appropriate orientation with respect to the rolling direction. Twins

form on $\{111\}$ planes with maximum resolved shear stress. Some grains do not contain deformation twins but contain a high density of planar dislocation structures (Fig. 29b). At $\varepsilon \sim 0.21$, almost all grains contain twins (Fig. 29c). Twinning as primary deformation mechanism leads to the formation of nanoscale layered structures due to the thickness of twins being ~ 100 nm. The previously formed twin boundaries tend to bend towards the rolling direction with strain. Large strain rolling leads to the formation of “S-shaped” bands delimiting the areas with lamella structures (Figs. 29e and 29f). Some lamellae show twin orientations, as seen in the inset in Fig. 29f. Neither ε - nor α' -martensite were observed via XRD measurements or TEM observation before and after extensive cold rolling.

Structure evolution of Fe-23% Mn-0.3% C-1.5% Al TWIP steel during cold rolling with reductions of 60 and 80% has been studied in [29]. Microshear bands (MSB) evolve in the microstructure after rolling with a reduction of 60%. MSBs pass through grain boundaries and cut previously formed twins

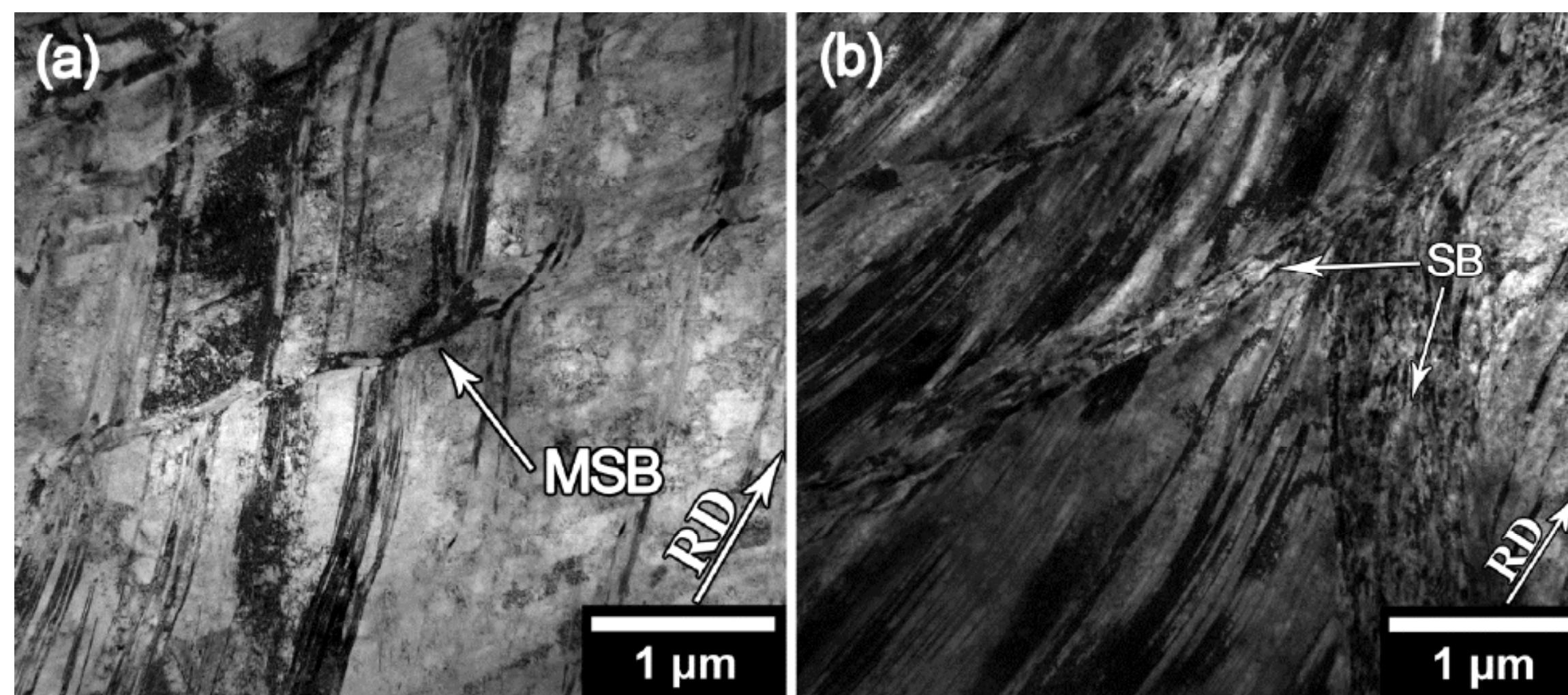


Fig. 30. Microstructure of the Fe-23%Mn-0.3%C-1.5%Al steel evolved after cold rolling to (a) 60%; (b) 80% reduction. MSB – microshear bands, SB – shear bands, RD – rolling direction.

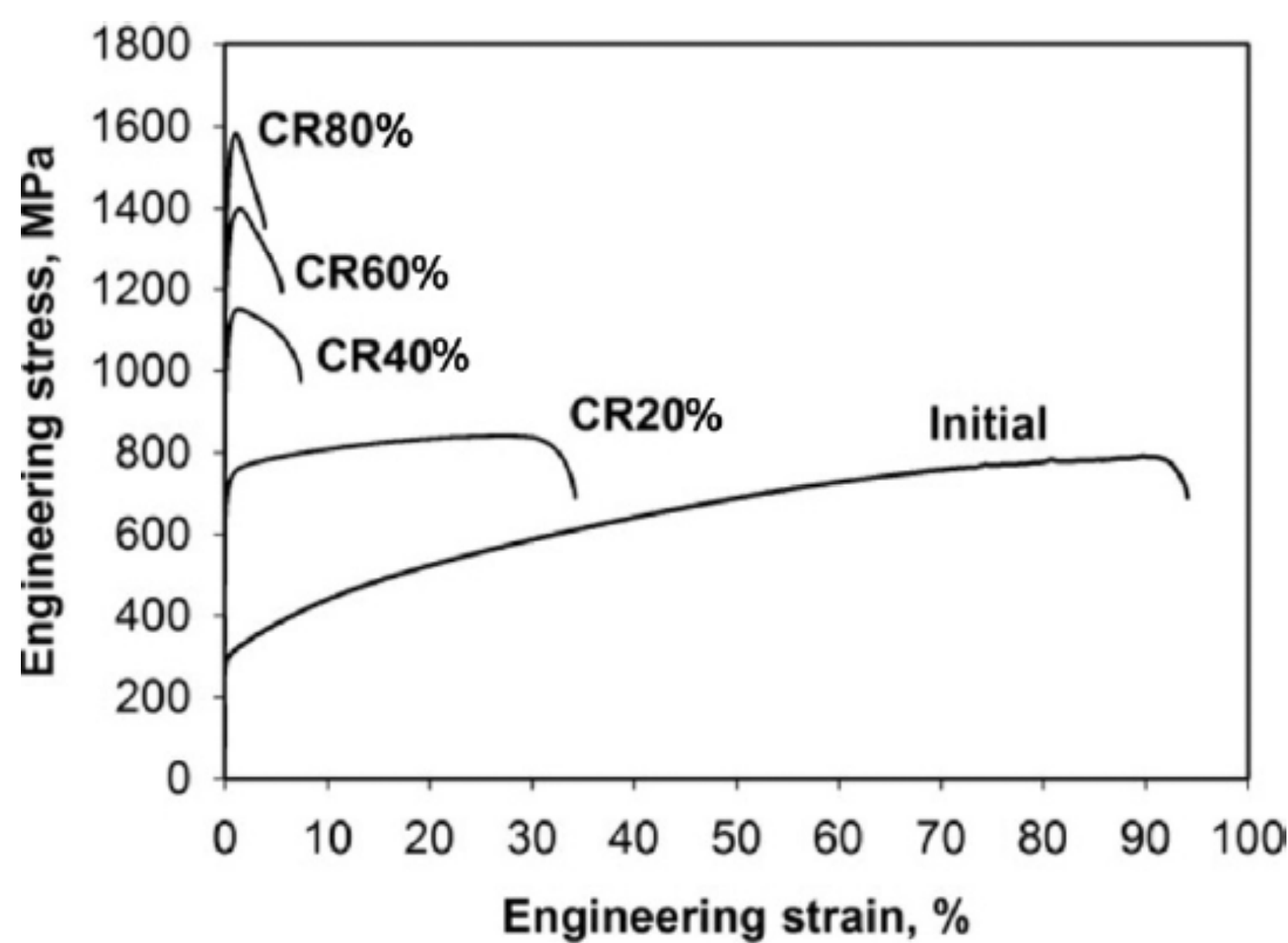


Fig. 31. The stress-strain curves of Fe-23Mn-0.3C-1.5Al steel. Deformed specimens are denoted as CR x , where CR means “cold rolled” and x indicates the reduction degree in %.

(Fig. 30a). Upon further rolling (Fig. 30b), the number of microshear bands and their thickness increased significantly. The mutual intersection of microshear bands and twins led to the formation of a spatial net of shear bands (SB) consisting of greatly misoriented crystallites with a size of approximately 40 nm. A specific feature of the microstructural evolution is that the previously formed twin boundaries tended to rearrange along the rolling direction and thus promoted the appearance of microshear bands to accommodate further strain.

Cold rolling leads to a significant deformation strengthening accompanied by a reduction in ductility. Engineering σ - ε curves for cold rolled Fe-23% Mn-0.3% C-1.5% Al steel [111] are shown in Fig. 31. This steel is characterized by a low YS of 235 MPa in the initial annealed condition. Cold rolling with 20% reduction increases the YS twice, and after cold rolling with a reduction of 80% the YS reaches 1400 MPa.

At the same time, a drastic drop of ductility occurs with increasing strain. At a reduction of 20%, uniform elongation is ~30% and drops to 7% or less

after higher reductions. It seems that 20% rolling reduction is a maximum, which can be used for producing hardened sheets from TWIP steels by cold rolling. The evolution of high density twinning lamellae and the appearance of very high dislocation densities above 10^{15} m^{-2} [111] stop the ability of TWIP steels to increase the number of these defects under tension. As a result, no strain-hardening occurs under the tension of samples subjected to extensive rolling that results in rapid necking and premature fracture. Similar behavior is typical for numerous nanocrystalline materials [112,113].

Generally, the microstructural evolution of TWIP steel under rolling can be divided into 2 stages clearly distinguished by deformation microstructures (Fig. 32). At rolling reductions below 40%, the microstructure consists of elongated grains with a high dislocation density. These grains may be subdivided by mechanical twins. Three types of grains evolve: type I grains are almost free of mechanical twins, type II grains contain one active primary twinning system and type III grains are characterized by more than one primary twinning system or secondary twinning system. Despite this distinct difference between separate grains, the steel exhibits superior ductility, which assumes no localization of plastic deformation within some grains. Therefore, there is no difference in the plastic deformation between grains of different types. This may be attributed to the fact that the subdivision of initial grains by deformation twins has a minor effect on flow stress. It seems that all types of initial grains are able to sustain plastic flow by the operation of dislocation sources and that increasing stress during tension mainly results from increased dislocation density.

At rolling reductions above 40%, three types of structural components evolve (Fig. 32): type II and type III grains and a nanocrystalline structure within areas of localized shear. A distinct change in the tensile behavior and the microstructural evolution

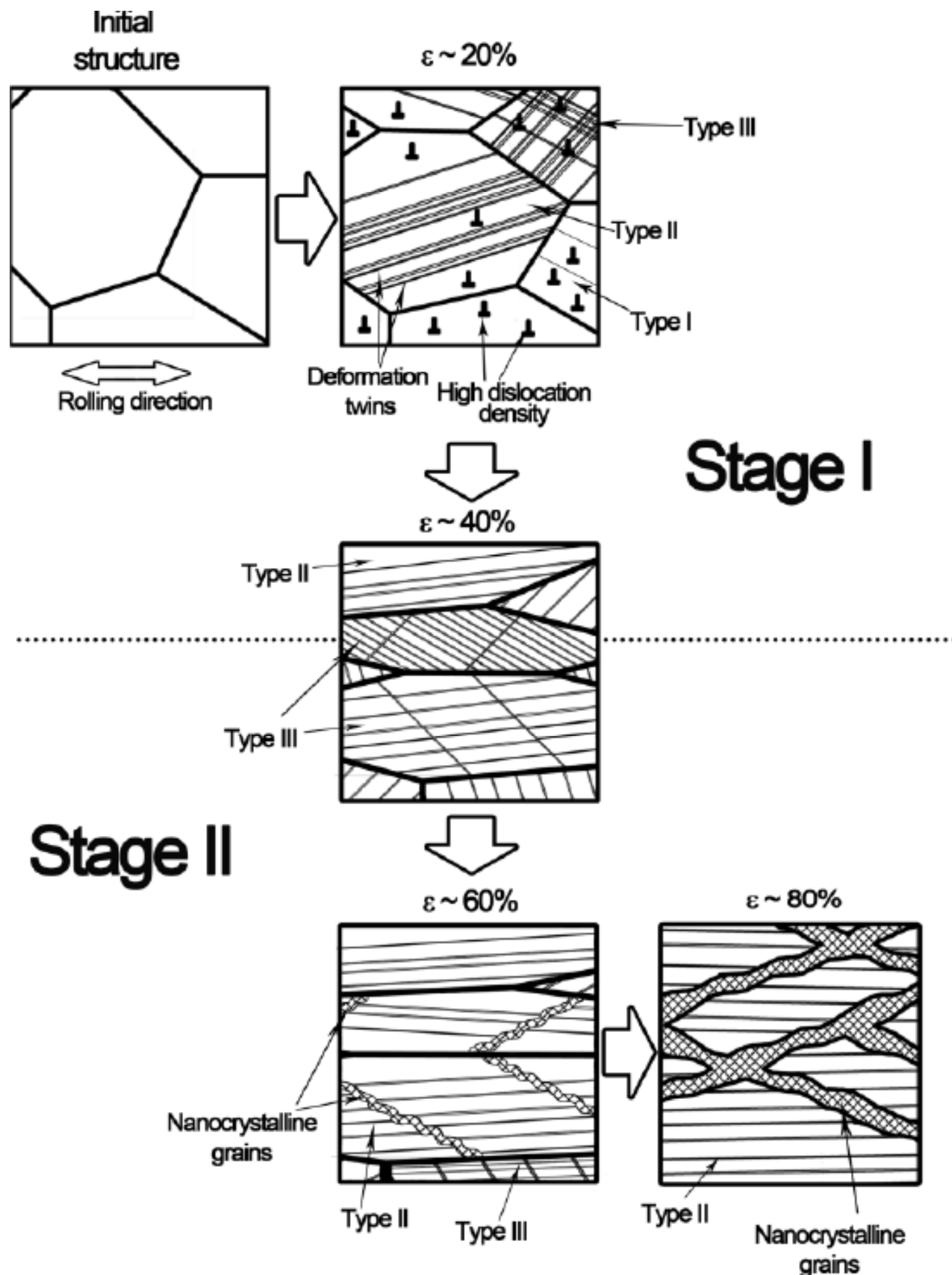


Fig. 32. Schematic of the microstructure evolution of TWIP steels upon rolling.

takes place at a rolling reduction of approximately 40%, when the feasibility of deformation twinning to accommodate plastic flow terminates. Further rolling results in increased dislocation density and the subdivision of initial grains to nanoscale crystallites. This in turn leads to a significant increase in the internal elastic strain. Therefore, at rolling reduction higher than 40%, the steel loses the ability to maintain further plastic flow by the simple emission of new dislocations. As a result, the material experienced difficulty in propagating the plastic flow through different microstructural components to provide general yielding of the specimen under the tension condition. Accordingly, very high stress is required to

initiate plastic flow; and stress localization within structural components with lower yielding leads to premature fracture due to unstable plastic flow.

It was demonstrated that intense plastic straining through equal angular channel pressing (ECAP) at elevated temperatures is highly effective for grain refinement of TWIP steels. Grain refinement to the submicron scale level allows high YS and sufficient ductility to be achieved concurrently in a Fe-0.61C-22.3Mn-0.19Si-0.14Ni-0.27Cr (wt.%) steel [114]. In annealed conditions, this steel exhibited extraordinary high plasticity of 123% and UTS of 930 MPa. The first ECAP pass at 400 °C led to a ductility reduction to 44%, while the UTS increased to 1290 MPa (Table 5).

Table 5. YS, UTS, and ductility of TWIP steel at different condition.

ECAP passes	YS, MPa	UTS, MPA	ϵ , %
As-received	312	930	123
1 pass (400 °C)	980	1286	44
2 passes(400 °C + 300 °C)	1250	1702	24
3 passes(400 °C + 300 °C + 300 °C)	1480	1624	21
4 passes(400 °C + 400 °C + 400 °C + 400 °C)	1290	1573	25

Two ECAP passes provided an increase of UTS to 1700 MPa; elongation-to-failure decreased to 24% (Table 5). Further ECAP processing led to decrease UTS and ductility (Table 5). YS increased up to the third ECAP pass from 312 MPa to 1480 MPa. Therefore, grain refinement is one way to attain very high YS with superior ductility. TWIP steel can be processed in the same way as conventional high-strength steel ($YS \geq 1400$ MPa, $UTS \geq 1600$ MPa) with a very high elongation-to-failure of $\geq 20\%$.

The main difference between microstructural evolution during cold rolling and ECAP at elevated temperatures consists in origin bands subdivided the initial austenite grains to nanoscale crystallites. Under ECAP, this subdivision occurs through the formation of thick MSBs located in parallel within 2° to $\{111\}_\gamma$ planes; the distance between these MSBs is approximately 260 ± 37 nm. Similar MSBs were observed in the other TWIP steels after high strain rate experiments [115,116]. The interactions between non-coplanar sets of MSBs leads to the subdivision of primary MSBs by secondary or tertiary MSBs into crystallites with a nearly rectangular shape and an average size ranging from 0.3 to 0.6 μm . Average misorientation of MSB boundaries increases with strain, and these boundaries become high-angle ones. True grains delimited by high-angle boundaries appear. Subgrains with an average size of 50 ± 10 nm were found within these grains.

The onset of mechanical twinning within these submicron scale grains were detected after a fourth ECAP concurrent with the formation of nanoscale subgrains. This is quite unusual because the SFE of this steel at 400 °C is ≥ 40 mJ/m², and, therefore, no mechanical twinning is expected. However, as shown in several publications by Zhu et al. [117,118], the formation of an ultrafine grain structure (UFG) in TWIP steels may promote the formation of twins, in contrast to the behavior of other materials [119]. The formation of deformation twins in UFG TWIP steels occurs through the operation of several unique twinning mechanisms [118]. Thus, mechanical twinning through specific mechanism provides very high ductility in TWIP steels in the UFG condition.

10. INFLUENCE OF HEAT TREATMENT ON MICROSTRUCTURE AND MECHANICAL PROPERTIES OF TWIP STEELS

Cold rolling is an attractive way to increase YS of TWIP steels. However, there are two disadvantages of this approach: (i) a strong decrease of the strain hardening takes place; (ii) a significant anisotropy in the mechanical behavior is introduced. Haase et al. [120] investigated the effect of annealing on the microstructure and mechanical properties of a Fe-23Mn-0.3C-1.5Al steel subjected to cold rolling with 30% reduction. This steel was annealed at 630 °C for 10 min and at 700 °C for 15 min to obtain recovered and recrystallized structures, respectively. The material after cold rolling showed the highest YS but the lowest uniform elongation, determined as 882 MPa and 15%, respectively (Fig. 33). After recovery annealing, the YS decreased to 640 MPa, and ductility increased to 25%. Recrystallization annealing led to a strong drop of YS to 312 MPa, while a high uniform elongation of 56% appears. Therefore, static recovery (SRV) offers a good com-

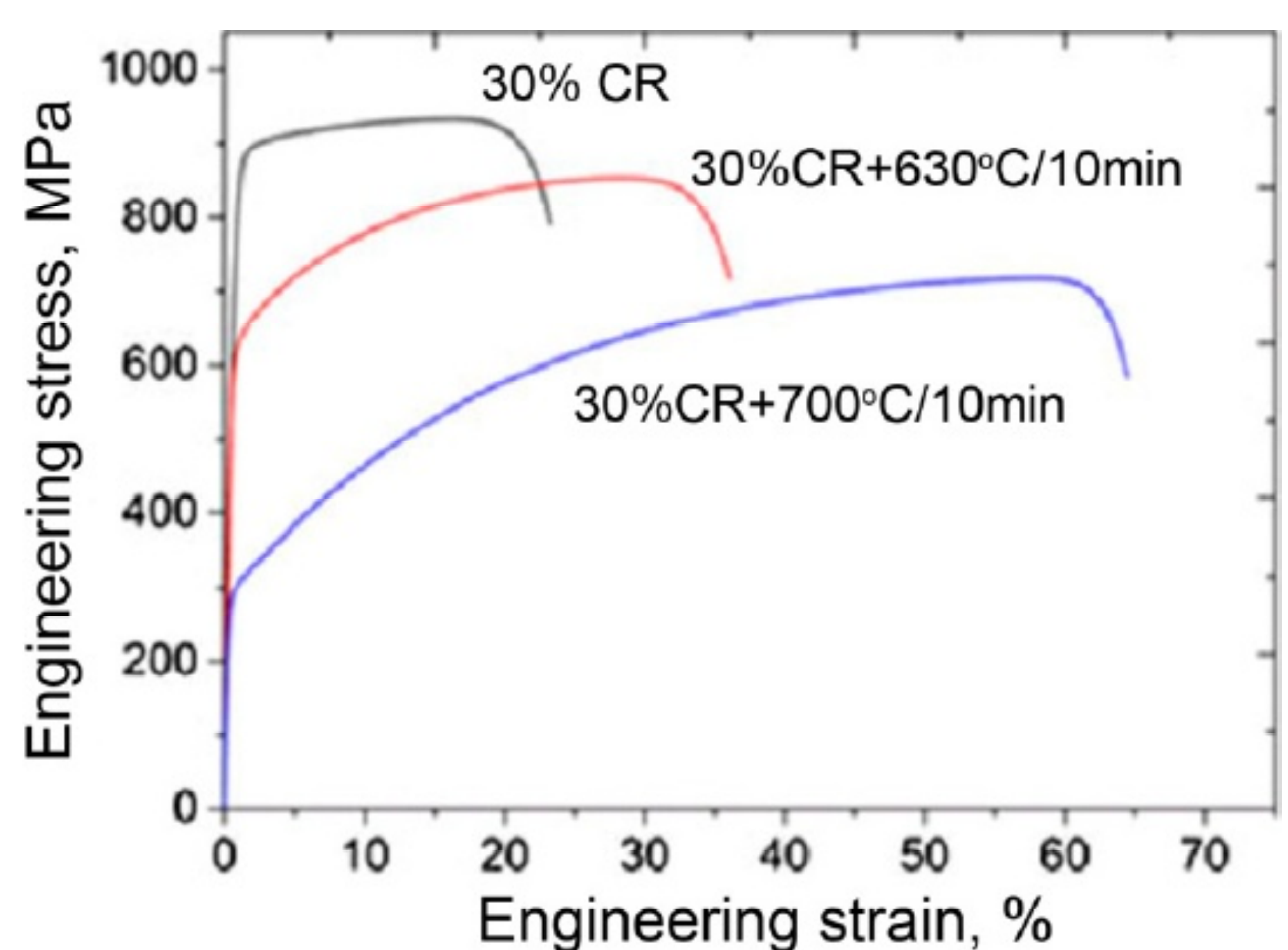


Fig. 33. Engineering stress–strain curves of the Fe-23Mn-0.3C-1.5Al TWIP steel in the various conditions. CR – cold rolled.

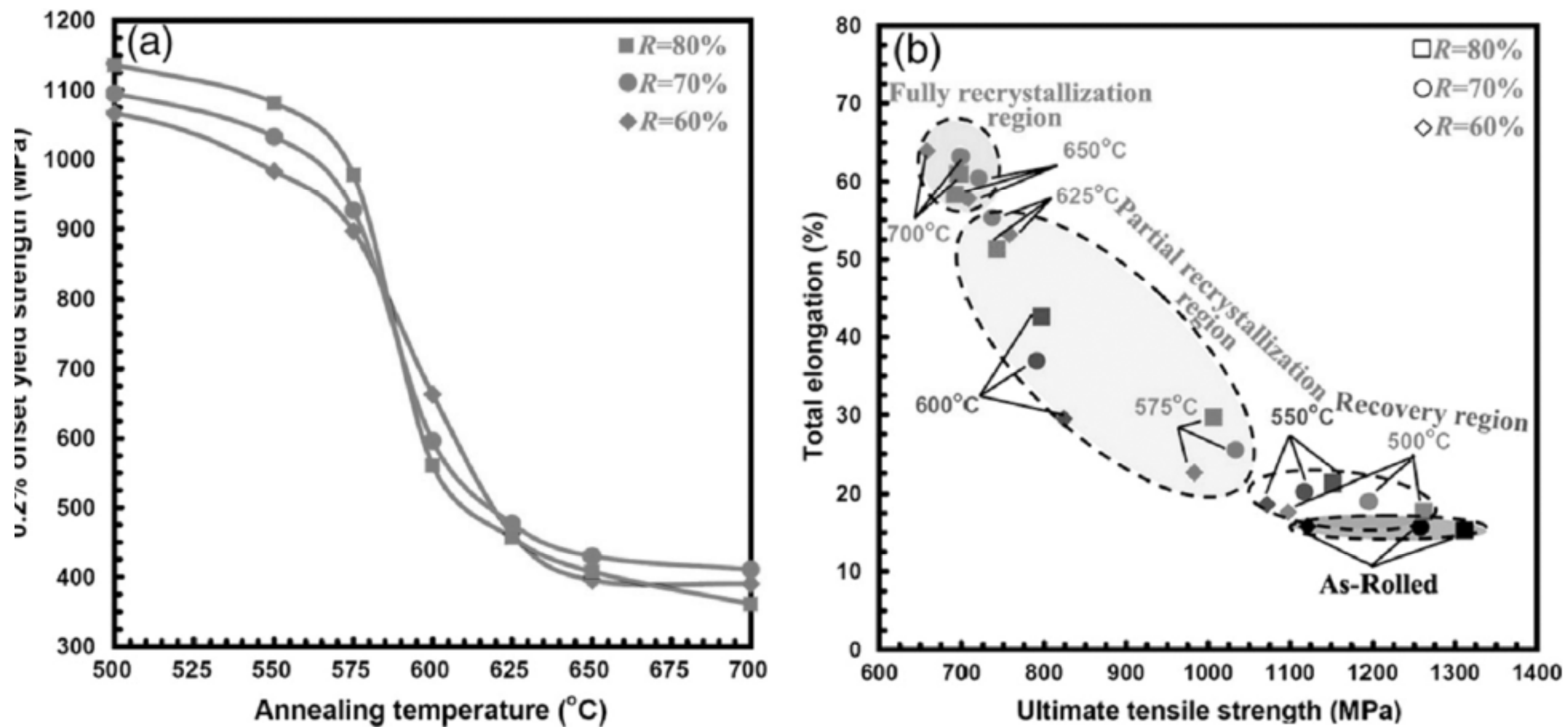


Fig. 34. The effect of annealing temperature on (a) the 0.2% offset yield strength and (b) ultimate tensile stress-total elongation balance of samples with different cold rolling reductions (R).

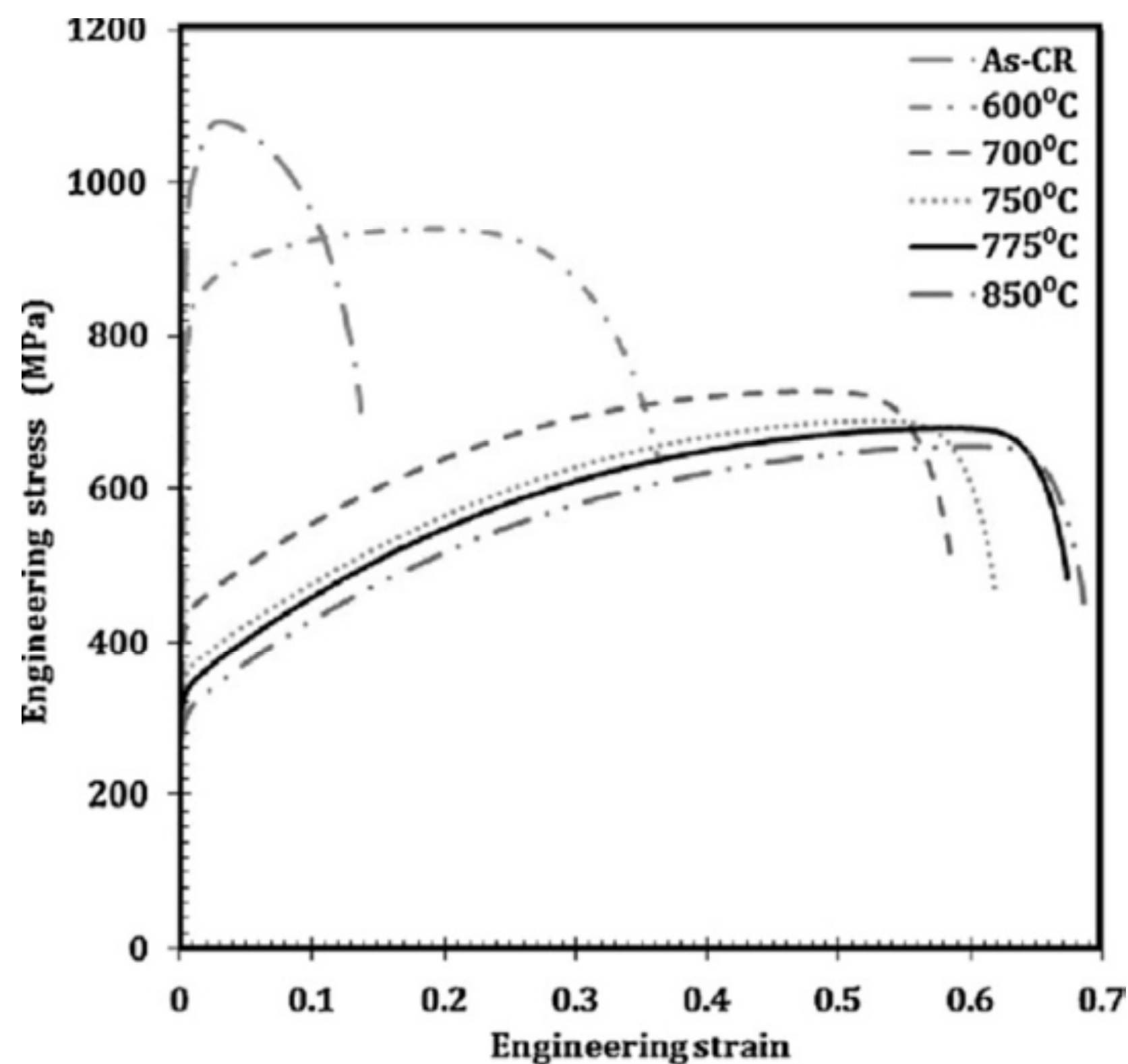


Fig. 35. Engineering stress versus strain curves of as-cold rolled, recovered and partially recrystallized Fe-24Mn-3Al-2Si-1Ni-0.06C TWIP steel.

combination of YS and ductility, while static recrystallization (SRX) leads to mechanical properties very close to the initial material in the coarse grained condition.

Similar work with wider range of strain and annealing parameters was performed by Dini et al. [121] on Fe-31Mn-3Al-3Si TWIP steel. The steel was subjected to cold rolling with reductions of 60, 70 and 80% with subsequent annealing in the temperature range 500 – 700 °C (Fig. 34). The authors showed that partial SRX offers an attractive combination of UTS and ductility; no remarkable difference in mechanical properties between recrystallized steel and the initial material was found, and

SRV yields high UTS and low elongation-to-failure close to these values demonstrated by the steel subjected to extensive rolling.

The effect of annealing on the microstructure and mechanical properties of cold rolled Fe-24Mn-3Al-2Si-1Ni-0.06C TWIP steel was studied by Santos [122] et al. The steel was isochronally annealed between 600 and 850 °C for 300 s after cold rolling with a reduction of 42% to produce different microstructures. It was confirmed that the onsets of SRV and SRX take place at 600 and 650 °C, respectively. A drop in UTS from 1080 MPa to 662 MPa and an increase in total elongation from 13.7% to 65.8% correlates with the formation of a fully recrystallized structure at 850 °C (Fig. 35). The TWIP steel in the recovered condition exhibits UTS of 935 MPa and total elongation of 32%.

As shown above, the partial SRX is an attractive way to obtain a good combination of stress and ductility in TWIP steels. Lu et al. [123] investigated the recrystallization kinetics in Fe-22Mn-0.4C TWIP steel during isothermal annealing at temperatures between 560 and 700 °C for various periods of time. The recrystallized volume fraction, X_{rex} , was calculated based on Vickers hardness (HV_1) measurements as:

$$X_{\text{rex}} = \frac{HV_{\text{initial}} - HV(t)}{HV_{\text{initial}} - HV_{\text{final}}} \quad (21)$$

The decrease of the measured hardness as a function of annealing time at different temperatures is shown in Fig. 36a. The kinetics of isothermal recrystallization are usually expressed by the

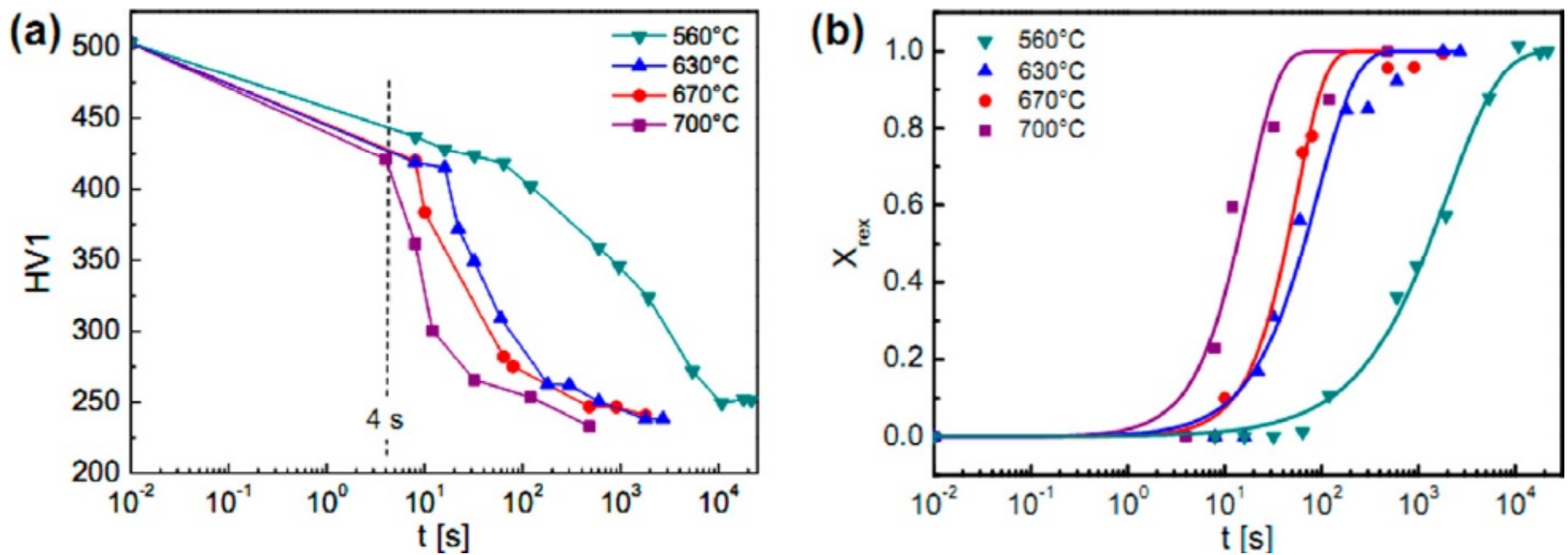


Fig. 36. (a) Vickers microhardness vs. time for annealing at 560, 630, 670, and 700 °C; (b) recrystallized volume fraction of investigated 50% cold-rolled Fe–Mn–C alloy vs. time of annealing.

Johnson–Mehl–Avrami–Kolmogorov (JMAK) equation:

$$X_{\text{rex}} = 1 - \exp \left[- \left(\frac{t}{t_R} \right)^n \right], \quad (22)$$

where t is the annealing time, t_R is characteristic time for recrystallization corresponding to a recrystallized volume fraction $X_{\text{rex}}(t_R) = 0.63$, and n is referred to as the Avrami exponent.

A significant softening occurred even after 4 s at any applied annealing temperature. The temporal change of the recrystallized volume fraction for all four annealing temperatures is presented in Fig. 36b. Typical Avrami-type recrystallization kinetics are obtained. A relatively sluggish recrystallization behavior was observed at a later stage of annealing and was especially pronounced at 560 °C. A recrystallized volume fraction of 60% was reached at 560 °C after 30 min of annealing, but it took more than 5 h to obtain an almost complete recrystallization.

The temperature dependence of the recrystallization time follows an Arrhenius-type relation [119]:

$$t_R = t_0 \cdot \exp \left(\frac{Q_{\text{RX}}}{kT} \right), \quad (23)$$

where Q_{RX} is the apparent activation energy of recrystallization and t_0 is the pre-exponential factor. The value of Q_{RX} is found to be 2.38 ± 0.3 eV or 229.8 ± 28.0 kJ/mol, which is slightly less than the activation energy of self-diffusion in γ -Fe (270 mJ/mol). The obtained values of the Avrami exponent ranged from 0.70 to 1.37 for temperatures between 560 and 700 °C [119].

The use of annealing or warm plastic deformation in the temperature interval 400–600 °C for pro-

cessing TWIP steel can be restricted by embrittlement attributed to segregation of Mn at boundaries. Until recently, there were no data for TWIP steels, but Kuzmina et al. [124] showed a strong embrittlement associated with the intergranular fracture of Fe-9Mn (Mn9) steels after annealing at 450 °C and 600 °C (Fig. 37). It was shown that the annealing of the Mn9 alloy at 450 °C for 1 minute enriches grain boundaries with 1.1 atom/nm² C and 4.8 atoms/nm² Mn excess. No concentrations of excess for the As, Sb, O, N, and P elements was revealed. The level of Mn segregation (11 at.%) after 450 °C annealing for 1 minute was found to be higher than expected from a Mn diffusion length of 0.7 nm. The unexpectedly strong drop in toughness that appears after 10 seconds of tempering at 450 °C was explained by the non-equilibrium concentration of manganese due to the formation of a C-Mn complex.

11. INFLUENCE OF MICROSTRUCTURE ON MECHANICAL PROPERTIES OF TWIP STEEL

Identification of the influence of microstructure on the mechanical properties of materials is the starting point of microstructural design. The dependence of the YS of TWIP steels on the grain size in the annealed condition is widely studied [125–130] and expressed by the Hall-Petch law (Fig. 38).

A different grain size was experimentally obtained by cold rolling and subsequent recrystallization annealing [121–126]. The minimum grain size in this case was approximately 2 μm [121, 124]. The works of Koyama et al. [131] and Saha et al. [132] should be mentioned individually. A microstructure

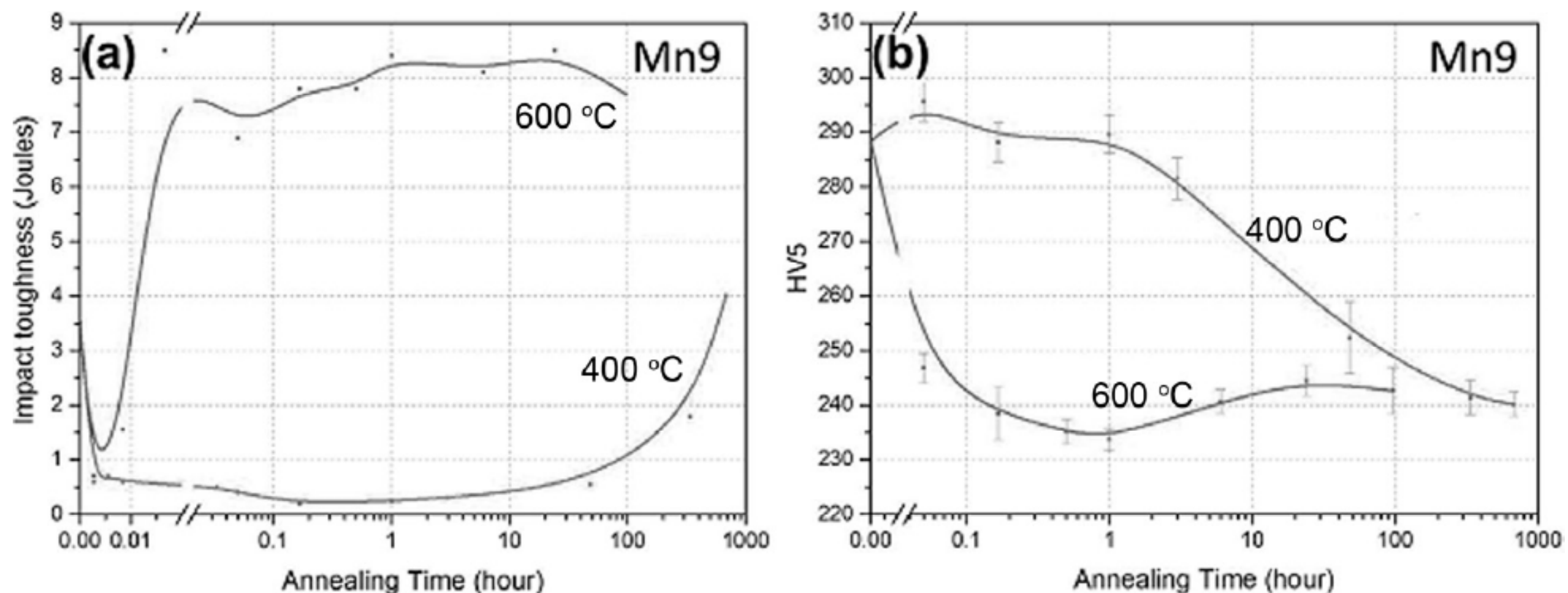


Fig. 37. Influence of annealing time and temperature on (a) room-temperature impact toughness of alloy Mn9; (b) hardness of Mn9.

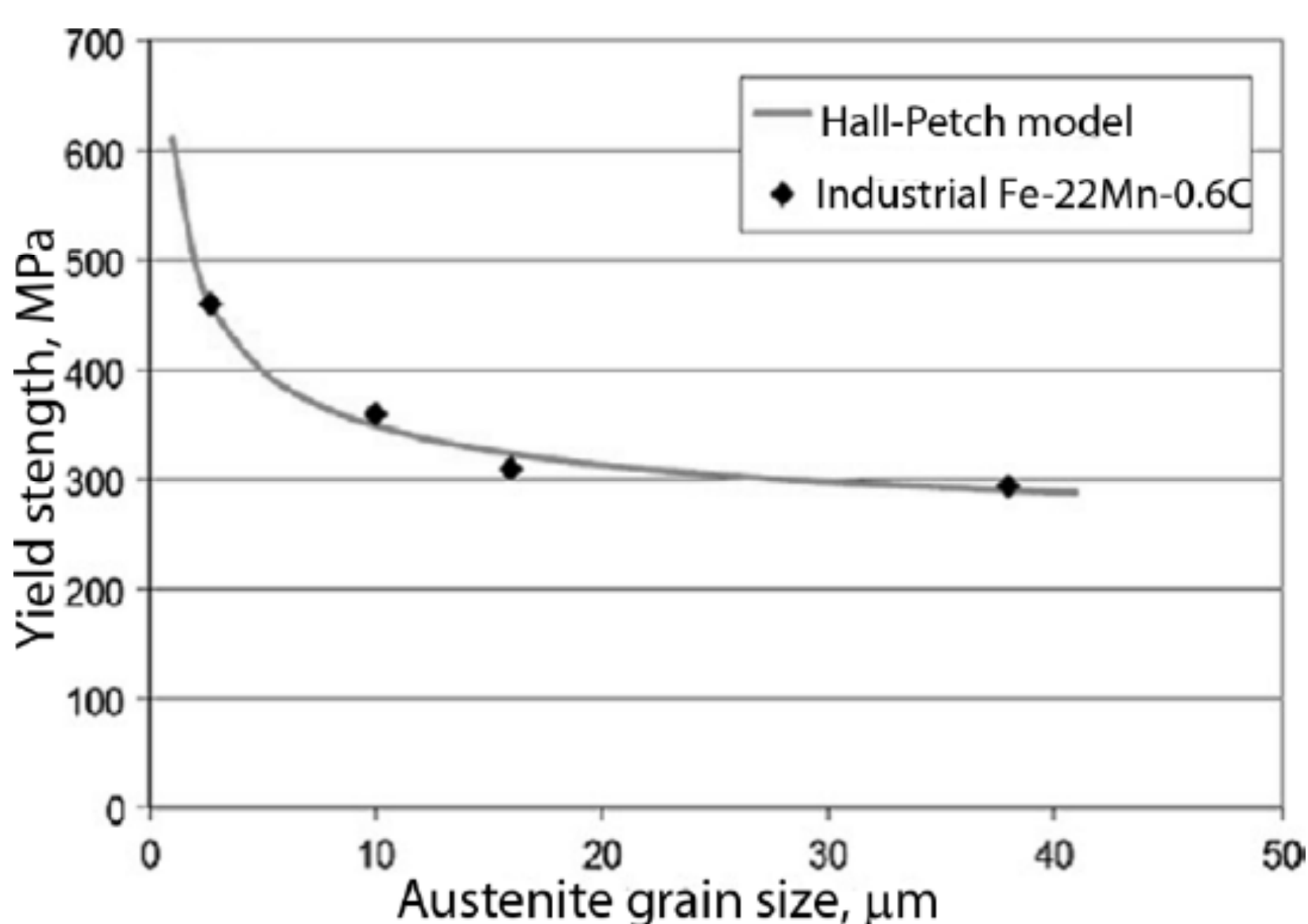


Fig. 38. YS variation with grain size of industrial Fe-22Mn-0.6C TWIP steel.

with an average grain size of approximately 460 nm was obtained in a Fe-17Mn-0.6C steel [127] by caliber rolling at 500 °C, and different grain sizes ranging from 350 to 540 nm were produced in a Fe-31Mn-3Si-3Al steel [128] by cold rolling with a reduction

of 92% and subsequent annealing at 650 °C for 3, 5, and 30 min. Due to this submicron grain size, the steel shows significantly higher values of YS and UTS under tension at room temperature (Fig. 39). The Fe-17Mn-0.6C steel also exhibits excellent cryogenic performance at -150 °C (Fig. 40). The authors consider that the main reason for the increased cryogenic properties of the Fe-17Mn-0.6C steel with the ultra-fine grained structure is the suppression of ϵ - and α' -martensite formation. Brittle fracture in Fe-Mn-C steels is seemed to be caused by the formation of ϵ -martensite; boundaries of ϵ - and α' -martensite serve as places for crack initiation and propagation [133]. Extensive grain refinement suppresses the formation of ϵ -martensite, and thus increases the ductility of TWIP steels in the UFG condition.

In addition to the grain size, it is necessary to determine the role of deformation twinning to calculate the strain hardening of TWIP steels.

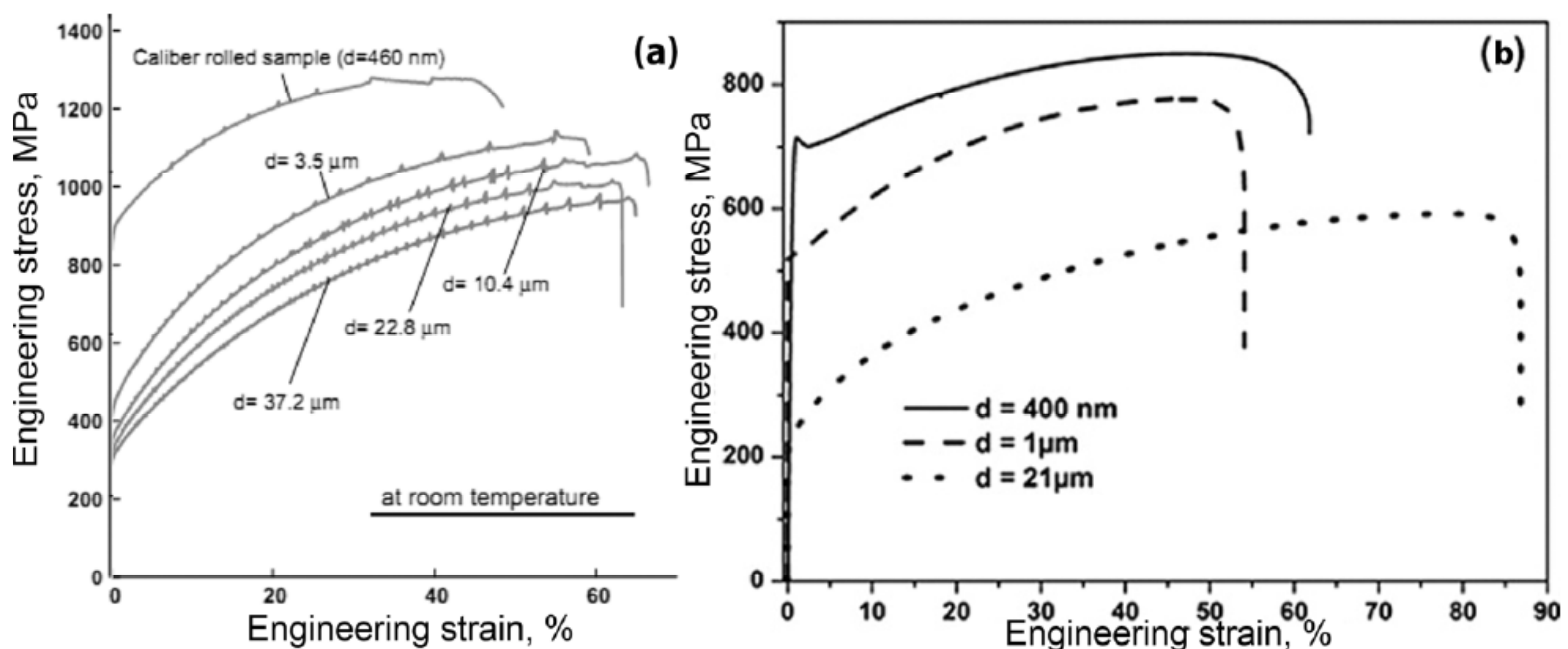


Fig. 39. Stress-strain curves of (a) Fe-17Mn-0.6C and (b) Fe-31Mn-3Si-3Al with different grain size. Replotted from [127] and [128], respectively.

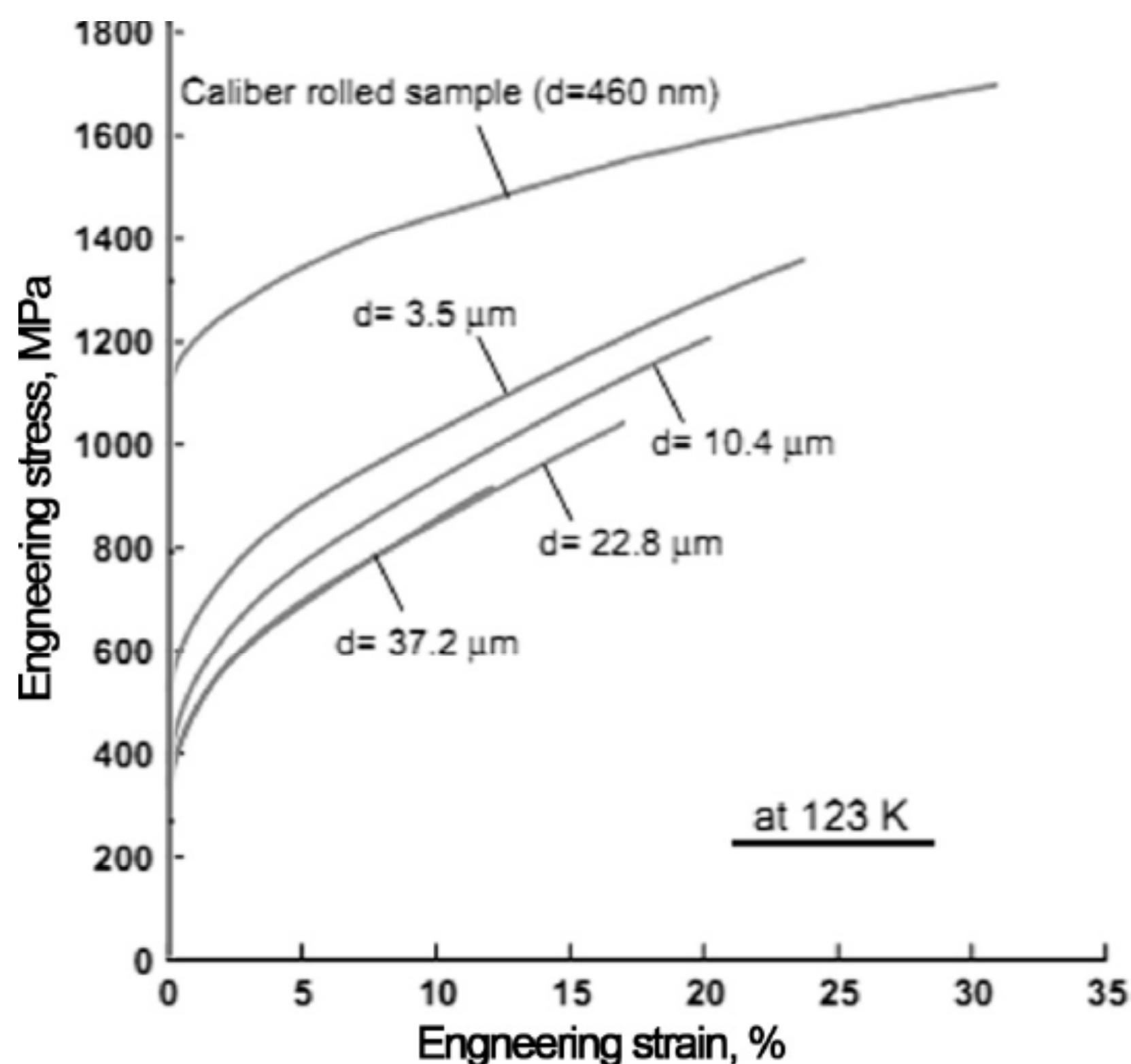


Fig. 40. Engineering stress–plastic strain curves of the Fe–17Mn–0.6C steel at 123K.

The role of deformation twinning in strain-hardening behavior was firstly considered by Remi [58]. To date, numerous studies on TWIP steels were focused on this subject [22,54,75,76,92,118,130]. All proposed approaches can be summarized as follows:

1) The mechanical twinning is considered to contribute to both the overall strain hardening and the development of forward and backward internal stresses in twin and matrix regions, respectively;

2) The effect of the chemical composition of the steel is considered in terms of a semi-phenomenological description [92] based on the Kocks-Mecking-Estrin (KME) model [135-138];

3) Nucleation and growth of mechanical twins is considered as a basis of modeling [75]. Modeling is performed in conjunction with the SEM electron channeling contrast imaging (ECCI) technique to observe a larger area and reveal the nanometer scale features.

Recently, Shterner et al. [139] proposed a constitutive model based on the KME model built upon the partitioning of the grains in a polycrystal into two distinct populations (twinned and twin-free). These grains have distinct differences in dislocation density evolution [22]. For both types of grains, strength dependence on the dislocation density can be written as follows:

$$\sigma = \sigma_0 + M\alpha Gb\sqrt{\rho}, \quad (24)$$

where σ_0 is a “friction stress”, α is a numerical constant that depends on the strength of the dislocation–dislocation interaction, G is the shear modulus, b is the magnitude of the Burgers vector and M

is the Taylor factor. Strain rate dependence included through a factor in power-law form in the original KME model is not included due to its rather weak influence. Dislocation density evolution for twin and twin-free grains is described by:

$$\frac{d\rho_{\text{twinned}}}{d\varepsilon} = M \left(\frac{1}{b\Lambda} + k_1\sqrt{\rho_{\text{twinned}}} - k_2\rho_{\text{twinned}} \right), \quad (25)$$

$$\frac{d\rho_{\text{twin-free}}}{d\varepsilon} = M \left(\frac{1}{b\Lambda} + k_1\sqrt{\rho_{\text{twin-free}}} - k_2\rho_{\text{twin-free}} \right). \quad (26)$$

Here the coefficients k_1 and k_2 represent the dislocation storage rate and the dynamic recovery rate, respectively. The dynamic recovery coefficient k_2 is strain rate, temperature and SFE dependent, while the parameter k_1 is commonly regarded as a rate independent material constant, but it may depend on SFE or microstructure. Λ is the dislocation mean free path and d is the average grain size. The following expression for the MFP covering the entire strain range was used:

$$\Lambda = \Lambda_0 H(\varepsilon_{\text{onset}} - \varepsilon) + \Lambda_0 \exp^{-C(\varepsilon_{\text{onset}} - \varepsilon)} H(\varepsilon_{\text{onset}} - \varepsilon). \quad (27)$$

Eq. (27) is a result of fitting in the strain range after the onset of twinning (i.e., above the onset strain for twinning $\varepsilon_{\text{onset}}$, which can be taken as 0.04 at room temperature, 0.14 at 100 °C and 0.24 at 200 °C) assuming that both the volume fraction, f , of the grains undergoing twinning and the twinned volume fraction in the grains that do exhibit twinning vary in the course of straining. Here, Λ_0 is the initial MPF, which is identical with the average grain size d .

The flow stress thus can be calculated as:

$$\sigma = f\sigma_{\text{twinned}} + (1-f)\sigma_{\text{twin-free}}, \quad (28)$$

where $\sigma_{\text{twinned}} = \sigma_0 + M\alpha Gb\sqrt{\rho_{\text{twinned}}}$ (6) and

$$\sigma_{\text{twin-free}} = \sigma_0 + M\alpha Gb\sqrt{\rho_{\text{twin-free}}}.$$

Values used in Eqs. (24)-(28) are listed in Table 6. Coefficients k_1 and k_2 for twinned and twin-free grains are listed in Table 7 after the tension at different temperatures.

Utilizing these parameters obtained, a very good agreement between the experimental data and the results of the model was obtained in the temperature range 20 - 400 °C, as shown in Figs. 41 and 42.

12. CONCLUSIONS

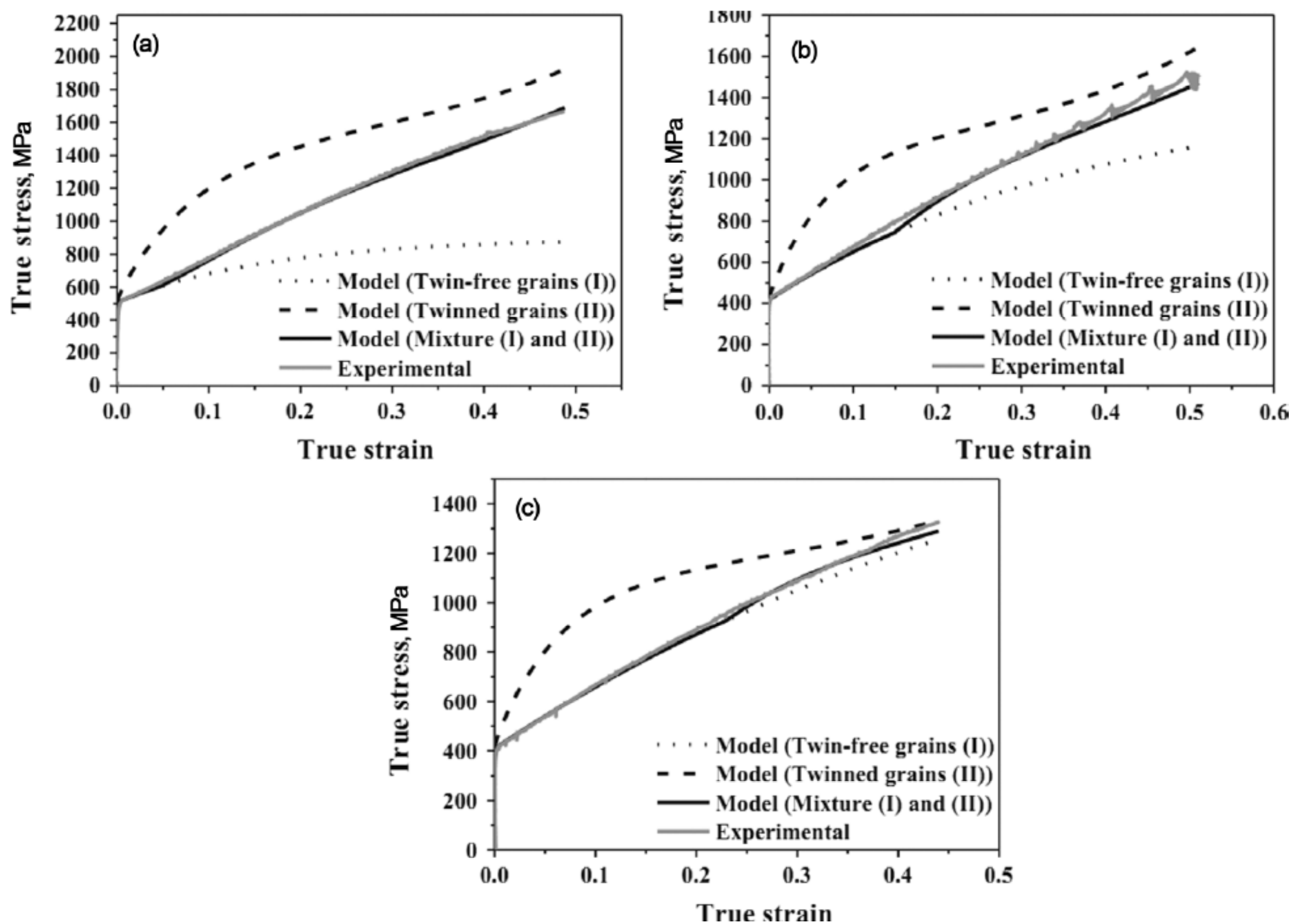
Austenitic steels exhibiting TWIP (twinning-induced plasticity) exhibit an excellent combination of

Table 6. Model parameter values.

Parameters	Physical meaning	Value
σ_0	“Friction” stress	170-410 MPa, temperature dependent
M	Taylor factor 3.06	
G	Shear modulus 60 GPa	
b	Magnitude of Burgers vector	2.5×10^{-10} m
r_{twinned}	Initial dislocation density in twinned grains	5×10^{13} m ⁻²
$r_{\text{twin-free}}$	Initial dislocation density in twin-free grains	5×10^{13} m ⁻²
C_1	Pre-exponential factor in Eq. (27)	0.025
C_2	Coefficient in the exponential factor in Eq. (27)	2.8

Table 7. Coefficients k_1 and k_2 for twinned and twin-free grains.

	Twinned grains		Twin-free grains	
	k_1	k_2	k_1	k_2
Room temperature	5×10^8	6.5	1.4×10^8 m ⁻¹	3.9
100 °C	5×10^8	8.3	1.4×10^8 m ⁻¹	2
200 °C	5×10^8	8.9	1.4×10^8 m ⁻¹	1.1
300 °C			1.4×10^8 m ⁻¹	1.7
400 °C			1.4×10^8 m ⁻¹	2.5

**Fig. 41.** Modelled and experimental true stress–true strain curves at (a) room temperature, (b) 100 °C, and (c) 200 °C. The curves corresponding to twin-free and twinned material taken separately are shown by dotted and dashed lines, respectively.

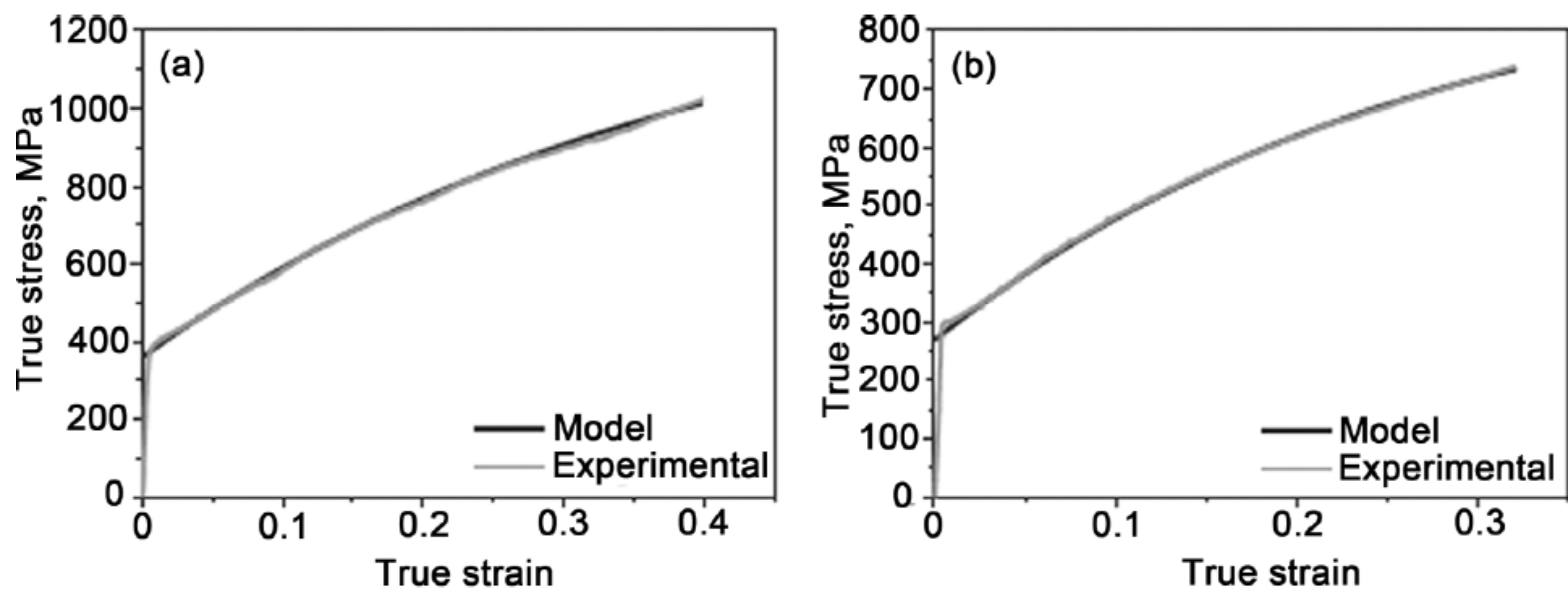


Fig. 42. A comparison between experimental true stress–true strain curves and the deformation curves predicted by the model at different tensile testing temperatures: (a) 300 °C and (b) 400 °C.

strength and ductility, ensuring a value of $\sigma_B \times \delta \geq 5 \times 10^4$ MPa \times %. These steels are considered advanced materials for applications in critical outer structures of car bodies. The concept of alloying in TWIP steels is aimed to provide a stacking fault energy (SFE) between 20 and 40 mJ/m² and to suppress plastic instability attributed to dynamic strain aging and delayed fracture. Thermomechanical processing provides an increase in yield stress up to 1000 MPa by reducing ductility. Extensive grain refinement by warm deformation is effective to produce a high-strength state of TWIP steels with yield stress ≥ 1400 MPa, ultimate tensile strength ≥ 1600 MPa and elongation-to-failure $\geq 20\%$. TWIP steels exhibit superior and unusual fatigue resistance. These steels withstand low-cycle loadings without remarkable softening, and the endurance limit of TWIP on the base of 10^7 is ~ 400 MPa significantly higher than yield stress. The unique ductility of TWIP in the recrystallized condition is attributed to mechanical twinning, which subdivides austenite grains to nanoscale crystallites delimited by twin boundaries. This allows an extraordinary accumulation of lattice dislocations within these crystallites up to very high densities $> 10^{15}$ m⁻². The superposition of grain size strengthening attributed to this subdivision and the deformation strengthening attributed to high dislocation density provides a very high rate of strain hardening, which is responsible for the stability of plastic flow up to high strains at ambient temperatures. The specific mechanisms of solid-solution strengthening associated with the formation of a C-Mn dipole or octahedral clusters CMn₆ can also give a significant contribution to overall hardening but may lead to plastic instability.

Nevertheless, many aspects of microstructural design and properties of TWIP steels remain unresolved to date:

- The mechanism of mechanical twinning that is operative in TWIP steels is very specific. As a result,

the application of known models for predicting volume fraction of deformation twins is not appropriate.

- The fundamental reasons for the delayed fracture of TWIP steels are not fully clarified.

- Little attention is paid to issues of welding TWIP steels, both with each other and with other structural materials.

Addressing these and other issues will help to achieve a better understanding of the plasticity mechanisms and to create the most advanced materials.

ACKNOWLEDGEMENTS

The financial support received from the Ministry of Education and Science, Russia, under Grant No. 14.578.21.0069 (ID number RFMEFI57814X0069) is gratefully acknowledged.

REFERENCES

- [1] H. Hofmann, D. Mattissen and Th.W. Schaumann // *Steel Res. Int.* **80** (2009) 22.
- [2] O. Kwon, K.Y. Lee, G. Kim and K.G. Chin // *Mater. Sci. Forum* **638-642** (2010) 136.
- [3] R.A. Hadfield // *Science* **12** (1888) 284.
- [4] Y.N. Dastur and W.C. Leslie // *Metall. Trans. A* **12** (1981) 749.
- [5] P.H. Adler, G.B. Olson and W.S. Owen // *Metall. Mater. Trans. A* **17** (1986) 1725.
- [6] A.A. Gulyaev, Yu.D. Tyapkin, V.A. Golikov and V.S. Zharinova // *Met. Sci. Heat Treat.* **27** (1985) 411.
- [7] K.S. Raghavan, A.S. Sastri and M.J. Marcinkowski // *Met. Soc. AIME-Trans.* **245** (1969) 1569.
- [8] I. Karaman, H. Sehitoglu, K. Gall, Y.I. Chumlyakov and H.J. Maier // *Acta Mater.* **48** (2000) 1345.

- [9] Karaman, H. Sehitoglu, A.J. Beaudoin and Y.I. Chumlyakov, H.J. Maier, C.N. Tome // *Acta Mater.* **48** (2000) 2031.
- [10] E.G. Astafurova, M.S. Tukeeva, G.G. Zakharova, E.V. Melnikov and H.J. Maier // *Mater. Char.* **62** (2011) 588.
- [11] M. Kato // *Mater. Trans.* **55** (2014) 19.
- [12] D. Canadinc, H. Sehitoglu, H.J. Maier and Y.I. Chumlyakov // *Acta Mater.* **53** (2005) 1831.
- [13] N. Hansen // *Scr. Mater.* **51** (2004) 801.
- [14] V.G. Gavriljuk and H. Berns, *High Nitrogen Steels* (Springer-Verlag Berlin Heidelberg, 1999).
- [15] D. Canadinc, C. Efstathiou and H. Sehitoglu // *Scr. Mater.* **59** (2008) 1103
- [16] W.S. Owen and M. Grujicic // *Acta Mater.* **47** (1999) 111.
- [17] N.R. Dudova, R.O. Kaibyshev and V.A. Valitov // *Phys. Met. Metall.* **108** (2009) 657.
- [18] M.A. Lebyodkin and Y. Estrin // *Acta Mater.* **53** (2005) 3403.
- [19] S. Malopheyev and R. Kaibyshev // *Mater. Sci. Eng. A* **620** (2014) 246.
- [20] D.T. Llewellyn and R.C. Hudd, *Steels: Metallurgy and Applications, Third Edition* (Butterworth-Heinemann, UK, 1998).
- [21] R. Twardowski, D.R. Steinmetz and U. Prahll // *Steel Res. Int.* **83** (2012) 340.
- [22] J.-K. Kim, Y. Estrin, H. Beladi, I.B. Timokhina, K.-G. Chin, S.-K. Kim and B.C. De Cooman // *Metall. Mater. Trans. A* **43** (2011) 479.
- [23] S.D. Antolovich and R.W. Armstrong // *Progr. Mater. Sci.* **59** (2014) 1.
- [24] A. Considère // *Ann. Ponts. Chauss.* **9** (1885) 574.
- [25] Y. Estrin and L.P. Kubin // *Acta Metall.* **34** (1986) 2455.
- [26] S. Hoffmann, W. Bleck and B. Berme // *Steel Res. Int.* **83** (2012) 379.
- [27] F.J. Humphreys and M. Hatherly, *Recrystallisation and Related Annealing Phenomena* (Pergamon Press, Oxford, 2004).
- [28] G. Dini, R. Ueji, A. Najafizadeh and S.M. Monir-Vaghefi // *Mater. Sci. Eng. A* **527** (2010) 2759.
- [29] P. Kusakin, A. Belyakov, C. Haase, R. Kaibyshev and D. Molodov // *Mater. Sci. Eng. A* **617** (2014) 52.
- [30] K. Chung, K. Ahn, D.H. Yoo, K.H. Chung, M.H. Seo and S.H. Park // *Int. J. Plast.* **27** (2011) 52.
- [31] G. Scavino, F. D'aiuto, P. Matteis, P. Russo Spena and D. Firrao // *Metall. Mater. Trans. A* **41** (2010) 1493.
- [32] M. Abbasi, S. Kheirandish, Y. Kharrazi and J. Hejazi // *Mater. Sci. Eng. A* 513– **514** (2009) 72.
- [33] E. Bayraktar, F.A. Khalid and C. Levallant // *J. Mater. Process. Technol.* **147** (2004) 145.
- [34] J. Lorthios, F. Nguyen, A.-F. Gourgues, T.F. Morgeneyer and P. Cugy // *Scripta Mater.* **63** (2010) 1220.
- [35] F. Musin, R. Kaibyshev, Y. Motohashi and G. Itoh // *Metall. Mater. Trans. A* 35A (2004) 2383.
- [36] M. Jobba, R.K. Mishra and M. Niewczas // *Int. J. Plast.* 65 (2015) 43.
- [37] D.-Y. Park and M. Niewczas // *Mater. Sci. Eng. A* 491 (2008) 88.
- [38] B.C. De Cooman, K.-G. Chin and J.Y. Kim, *New Trends and Developments in Automotive System Engineering* (InTech, 2011).
- [39] X.M. Qin, L.Q. Chen, H.S. Di and W. Deng // *Acta Metall. Sin.* **47** (2011) 1117, In Chinese.
- [40] K. Phiu-on, Deformation mechanisms and mechanical properties of hot-rolled Fe-Mn-C-(Al)-(Si) austenitic steels (Ph.D. thesis, RWTH Aachen, 2008).
- [41] O. Bouaziz, S. Allain, C.P. Scott, P. Cugy and D. Barbier // *Curr. Op. in Solid State Mater. Sci.* 15 (2011) 141.
- [42] M.Y. Demeri, *Advanced high-strength steels: Science, technology, and applications* (ASM International, 2013).
- [43] Y. Kim, N. Kang, Y. Park, I. Choi, G. Kim, S. Kim and K. Cho // *J. Korean Inst. Met. Mater.* **46** (2008) 780.
- [44] J.K. Jung, O.Y. Lee, Y.K. Park, D.E. Kim and K.G. Jin // *Korean J. Mater. Res.* **18** (2008) 394.
- [45] H.K. Yang, Z.J. Zhang and Z.F. Zhang // *Scr. Mater.* **68** (2013) 992.
- [46] D.T. Pierce, The Influence of Manganese Content and Temperature on the Relative FCC/HCP Phase Stability and Strain-Hardening Behavior of High-Manganese TRIP/TWIP Steels (Vanderbilt University, Ph.D. Thesis, 2014).
- [47] D. Barbier, N. Gey, S. Allain, N. Bozzolo and M. Humbert // *Mater. Sci. Eng. A* **500** (2009) 196.
- [48] H. Beladi, I.B. Timokhina, Y. Estrin, J. Kim, B.C. De Cooman and S.K. Kim // *Acta Mater.* **59** (2011) 7787.

- [49] I. Gutierrez-Urrutia and D. Raabe // *Acta Mater.* **59** (2011) 6449.
- [50] I. Mejia, A.E. Salas-Reyes, A. Bedolla-Jacuinde, J. Calvo and J.M. Cabrera // *Mater. Sci. Eng. A* **616** (2014) 229.
- [51] A.E. Salas-Reyes, I. Mejia, A. Bedolla-Jacuinde, A. Boulaajaj, J. Calvo and J.M. Cabrera // *Mater. Sci. Eng. A* **611** (2014) 77.
- [52] K. Yan, D.G. Carr, M.D. Callaghan, K.-D. Liss and H. Li. // *Scripta Mater.* **62** (2010) 246.
- [53] R.T. Tol, L. Zhao, H. Schut and J. Sietsma // *Metall. Mater. Trans. A* **43** (2012) 3070.
- [54] S. Allain, J.-P. Chateau, O. Bouaziz, S. Migot and N. Guelton // *Mater. Sci. Eng. A* **387-389** (2004) 158.
- [55] O. Bouaziz, S. Allain and C. P. Scott // *Scripta Mater.* **58(6)** (2008) 484.
- [56] N.I. Medvedeva, M.S. Park, D.C. Van Aken and J.E. Medvedeva // *J. All. Comp.* **582** (2014) 475.
- [57] Y.-K. Lee and C.-S. Choi // *Metall. Mater. Trans. A* **31** (2000) 355.
- [58] T.S. Byun // *Acta Mater.* **51** (2003) 306371.
- [59] L. Remy // *Acta Metall.* **26** (1978) 443.
- [60] D.T. Pierce, J. Bentley, J.A. Jiménez and J.E. Wittig // *Scripta Mater.* **66** (2012) 753.
- [61] P.C.J. Gallagher // *Metall. Trans.* **1** (1970) 2429.
- [62] K. Kapoor, D. Lahiri, I.S. Batra, S.V.R. Rao and T. Sanyal // *Mater. Char.* **54** (2005) 131.
- [63] J.P. Hirth // *Metall. Trans. A* **1A** (1970) 2367.
- [64] A. Saeed-Akbari, J. Imlau, U. Prah and W. Bleck // *Metall. Mater. Trans. A* **40** (2009) 3076.
- [65] L. Remy // *Acta Metall.* **25** (1977) 173.
- [66] A. Dumay, J.-P. Chateau, S. Allain, S. Migot and O. Bouaziz // *Mater. Sci. Eng. A* **483-484** (2008) 184.
- [67] Q.X. Dai, X.N. Cheng, Y.T. Zhao, X.M. Luo and Z.Z. Yuan // *Mater. Charact.* **52** (2004) 349.
- [68] J.C. Li, W. Zheng and Q. Jiang // *Mater. Lett.* **38** (1999) 275.
- [69] K. Jeong, J.-E. Jin, Y.-S. Jung, S. Kang and Y.-K. Lee // *Acta Mater.* **61** (2013) 3399.
- [70] Y.N. Petrov // *Scripta Mater.* **53** (2005) 1201.
- [71] A. Saeed-Akbari, L. Mosecker, A. Schwedt and W. Bleck // *Metall. Mater. Trans. A* **43** (2011) 1688.
- [72] B.X. Huang, X.D. Wang, L. Wang and Y.H. Rong // *Metall. Mater. Trans. A* **39A** (2008) 717.
- [73] T.-H. Lee, E. Shin, C.-S. Oh, H.-Y. Ha and S.-J. Kim // *Acta Mater.* **58** (2010) 3173.
- [74] G. Frommeyer, U. Brück and P. Neumann // *ISIJ Int.* **43** (2003) 438.
- [75] J.-H. Xu, W. Lin and A. J. Freeman // *Phys. Rev. B* **43** (1991) 2018.
- [76] C. Wang et al // *Nature Sci. Rep.* **5** (2015) 10213.
- [77] J.A. Venables // *Philos. Mag.* **30** (1974) 1165.
- [78] J.B. Cohen and J. Weertman // *Acta Metall.* **11** (1963) 996.
- [79] T. Mori and H. Fujita // *Acta Metall.* **28** (1980) 771.
- [80] S. Mahajan and G.Y. Chin // *Acta Metall.* **21** (1973) 173.
- [81] L. Bracke, L. Kestens and J. Penning // *Scr. Mater.* **61** (2009) 220.
- [82] H. Idrissi, K. Renard, L. Ryelandt, D. Schryvers and P.J. Jacques // *Acta Mater.* **58** (2010) 2464.
- [83] H. Idrissi, K. Renard, D. Schryvers and P.J. Jacques // *Philos. Mag.* **93** (2013) 4378.
- [84] D.R. Steinmetz, T. Japel, B. Wietbrock, P. Eisenlohr, I. Gutierrez-Urrutia, A. Saeed-Akbari, T. Hickel, F. Roters and D. Raabe // *Acta Mater.* **61** (2013) 494.
- [85] O. Bouaziz and N. Guelton // *Mater. Sci. Eng. A* **319-321** (2001) 246.
- [86] D. Zhemchuzhnikova, S. Malopheyev, S. Mironov and R. Kaibyshev // *Mater. Sci. Eng. A* **598** (2014) 387.
- [87] D. Zhemchuzhnikova and R. Kaibyshev // *Adv. Eng. Mater.* (2015) (in press).
- [88] I. Polmear and D.St. John, *Light Alloys: From Traditional Alloys to Nanocrystals* (Butterworth-Heinemann, 2005).
- [89] V.T. Witusiewicz, F. Sommer and E.J. Mittemeijer // *J. Phase Equilibria Diffus.* **25** (2004) 346.
- [90] H. Schumann // *Neue Huette* **17** (1972) 605.
- [91] O. Grassel, G. Frommeyer, C. Derder and H. Hofmann // *Le Journal de Physique IV* **07** (1997) 383.
- [92] O. Grassel and G. Frommeyer // *Mater. Sci. Technol.* **15** (1998) 1213.
- [93] O. Bouaziz, H. Zurob, B. Chehab, J.D. Embury, S. Allain and M. Huang // *Mater. Sci. Technol.* **27** (2010) 707.
- [94] S. Hong, S.Y. Shin, H.-S. Kim, S. Lee, S.-K. Kim, K.-G. Chin and N. J. Kim // *Metall. Mater. Trans. A* **43** (2012) 1870.
- [95] K.T. Park, K.G. Jin, S.H. Han, S.W. Hwang, K. Choi and C.S. Lee // *Mater. Sci. Eng. A* **527** (2010) 3651-3661.

- [96] J. Kang, D.S. Wilkinson, M. Jain, J.D. Embury, A.J. Beaudoin, S. Kim, R. Mishra and A.K. Sachdev // *Acta Mater.* **54** (2006) 209.
- [97] S.-J. Lee, J. Kim, S.N. Kane and B.C. De Cooman // *Acta Mater.* **59** (2011) 6809.
- [98] K. Renard, S. Ryelandt and P.J. Jacques // *Mater. Sci. Eng. A* **527** (2010) 2969.
- [99] L. Chen, H.-S. Kim, S.-K. Kim and B.C. De Cooman // *ISIJ Int.* **47** (2007) 1804.
- [100] A. Saeed-Akbari, A. K. Mishra, J. Mayer and W. Bleck // *Metallurgical and Materials Transactions A* **43** (2012) 1705.
- [101] T.A. Lebedkina, M.A. Lebyodkin, J.-P. Chateau, A. Jacques and S. Allain // *Mater. Sci. Eng. A* **519** (2009) 147.
- [102] K.S.B. Rose and S.G. Glover // *Acta Metall.* **14** (1966) 1505.
- [103] S. Allain, P. Cugy, C. Scott, J.P. Chateau, A. Rusinek and A. Deschamps // *Int. J. Mater. Res.* **99** (2008) 734.
- [104] A.S. Hamada, L.P. Karjalainen and J. Puustinen // *Mater. Sci. Eng. A* **517** (2009) 68.
- [105] A.S. Hamada, L.P. Karjalainen, A. Ferraiuolo, J. Gil Sevillano, F. De Las Cuevas, G. Pratolongo and M. Reis // *Metall. Mater. Trans. A* **41A** (2010) 1102.
- [106] A.S. Hamada and L.P. Karjalainen // *Mater. Sci. Eng. A* **527** (2010) 5715.
- [107] Y.-X. Wu, D. Tang, H.-T. Jiang, Z.-L. Mi, Y. Xue, H.-P. Wu // *J. Iron Steel Res. Int.* **21** (2014) 352.
- [108] C.J. Rüsing, T. Niendorf, A. Frehn and H.J. Maier // *Adv. Mater. Res.* **891-892** (2014) 1603.
- [109] I. Nikulin, T. Sawaguchi and K. Tsuzaki // *Mater. Sci. Eng. A* **587** (2013) 192.
- [110] S. Vercammen, B. Blanpain, B.C. De Cooman and P. Wollants // *Acta Mater.* **52** (2004) 2005.
- [111] P. Kusakin, A. Belyakov, R. Kaibyshev and D.A. Molodov // *Adv. Mater. Res.* **922** (2014) 394.
- [112] I. Shakhova, V. Dudko, A. Belyakov, K. Tsuzaki and R. Kaibyshev // *Mater. Sci. Eng. A* **545** (2012) 176.
- [113] R.Z. Valiev and T.G. Langdon // *Adv. Eng. Mater.* **12** (2010) 677.
- [114] I.B. Timokhina, A. Medvedev and R. Lapovok // *Mater. Sci. Eng. A* **593** (2014) 163.
- [115] D.A. Hughes and W.D. Nix // *Mater. Sci. Eng. A* **122** (1989) 153.
- [116] D.A. Hughes // *Acta Mater.* **41** (1993) 1421.
- [117] Y.T. Zhu, X.Z. Liao, X.L. Wu and J. Narayan // *J. Mater. Sci.* **48** (2013) 4467.
- [118] Y.T. Zhu, X.Z. Liao and X.L. Wu // *Prog. Mater. Sci.* **57** (2012) 1.
- [119] R.Z. Valiev, R.K. Islamgaliev and I.V. Alexandrov // *Progr. in Mater. Sci.* **45** (2000) 103.
- [120] C. Haase, L.A. Barrales-Mora, D.A. Molodov and G. Gottstein // *Metall. Mater. Trans. A* **44** (2013) 4445.
- [121] G. Dini, A. Najafizadeh, R. Ueji and S.M. Monir-Vaghefi // *Mater. Lett.* **64** (2010) 15.
- [122] D.B. Santos, A.A. Salehn, A.A. Gazder, A. Carman, D.M. Duarte and E.A.S. Ribeiro // *Mater. Sci. Eng. A* **528** (2011) 3545.
- [123] Y. Lü, , D.A. Molodov and G. Gottstein // *Acta Mater.* **59** (2011) 3229.
- [124] M. Kuzmina, D. Ponge and D. Raabe // *Acta Mater.* **86** (2015) 182.
- [125] R. Ueji, N. Tsuchida, D. Terada, N. Tsuji, Y. Tanaka, A. Takemura and K. Kunishige // *Scr. Mater.* **59** (2008) 963.
- [126] S.H. Wang, Z.Y. Liu and G.D. Wang // *Acta Metall. Sin.* **45** (2009) 1083.
- [127] E. El-Danaf, S.R. Kalidindi and R.D. Doherty // *Metall. Mater. Trans. A* **30** (1999) 1223.
- [128] G. Dini, A. Najafizadeh, R. Ueji and S.M. Monir-Vaghefi // *Mater. Des.* **31** (2010) 3395.
- [129] J.D. Yoo, S.W. Hwang and K.T. Park // *Mater. Sci. Eng. A* **508** (2009) 234.
- [130] J.D. Yoo and K.D. Park // *Mater. Sci. Eng. A* **496** (2008) 417.
- [131] M. Koyama, T. Lee, C.S. Lee and K. Tsuzaki // *Mater. Des.* **49** (2013) 234.
- [132] R. Saha, R. Ueji and N. Tsuji // *Scr. Mater.* **68** (2013) 813.
- [133] M. Koyama, T. Sawaguchi, T. Lee, C.S. Lee and K. Tsuzaki // *Mater. Sci. Eng. A* **528** (2011) 7310.
- [134] J. Gil Sevillano // *Scripta Materialia* **60** (2009) 336.
- [135] H. Mecking and U.F. Kocks // *Acta Metall.* **29** (1981) 1865.
- [136] U.F. Kocks // *J. Eng. Mater. Technol.* **98** (1976) 76.
- [137] L.P. Kubin and Y. Estrin // *Acta Metall. Mater.* **38** (1990) 697.
- [138] Y. Estrin and H. Mecking // *Acta Metall.* **32** (1984) 14.
- [139] V. Shterner, A. Molotnikov, I.B. Timokhina, Y. Estrin and H. Beladi // *Mater. Sci. Eng. A* **613** (2014) 224.